Electron and nuclear spin sensing using nitrogen-vacancy centers in diamond

February 2020

Kento Sasaki

A Thesis for the Degree of Ph.D. in Engineering

Electron and nuclear spin sensing using nitrogen-vacancy centers in diamond

February 2020

Graduate School of Science and Technology
Keio University

Kento Sasaki

Abstract

A nitrogen-vacancy (NV) center is a point defect in diamond accompanying one singlet-triplet ($S = 1$) electron spin in its negatively charged state, and its remarkable properties allow for optical initialization/readout and microwave control of the single spin at room temperature. The precession of the spin is very sensitive to the change in the surrounding environment such as temperature, electric field, and magnetic field. Therefore, research towards application of the NV as a quantum sensor has become very active especially in the past decade.

Among many, one of the most promising applications is a magnetic field sensor for a single molecule nuclear magnetic resonance (NMR) and magnetic resonance imaging (MRI). The sensitivity capable of detecting a magnetic field arising from a single nuclear spin has been demonstrated when NV is placed sufficiently close (< 10 nm) to the target nuclear spin. The spectrum resolution comparable with the conventional NMR was demonstrated employing a microwave spin control sequence synchronized with a classical clock. The single spin of NV is confined within the atomic scale volume so the atomic spatial resolution of magnetic resonance imaging (MRI) should be possible when it is made into a scanning probe or a static sensor capable of separating the magnetic field coming from individual nuclei of the target molecule. One of obvious goals of the NV-based magnetometry is therefore structure analysis of an individual molecule either by the scanning NV probe or static NV capable of pinpointing each nucleus in the molecule.

The present thesis research has been conducted to understand physical properties of the NV center interacting with magnetic fields arising from surrounding electron and nuclear spins, and to develop methods to improve the sensitivity, spectrum resolution, and spatial resolution of the NV as a quantum sensor.

Firstly, we have designed and built an optically detected magnetic resonance (ODMR) setup, a system capable of initialization, manipulation, and readout a single NV center spin and NV ensembles spins. The system is also capable of simultaneous initialization and manipulation of the target nuclear spins for NMR. A specially designed microwave planar ring antenna for ODMR has been fabricated for wide-field ($\sim$1 mm^2) PL mapping, magnetic field imaging, and ODMR.

Secondly, we have applied ODMR with a narrow band microwave pulse control to enhance the DC field sensitivity of a high density NV ensemble placed near the surface of diamond. Together with dynamic nuclear polarization of nitrogen nuclei within NVs, we have obtained a high DC sensitivity of 35 nT $Hz^{0.5}$. We have also measured the coherence of the NV electron spin using Hahn-echo and found that the coherence was degraded at the level crossing condition by paramagnetic impurity electron spins in the diamond thin film. This additional decoherence depended on the density of the flipped spin. We have also carried out spectroscopy of the decoherence for the quantitative analysis of the paramagnetic defect densities.

Lastly, we have advanced to the nuclear spin detection with a single NV center. Our final goal is to perform MRI of individual nucleus in a single molecule placed on a diamond surface using a static single NV placed near the surface of the diamond. Here identification of chemical species of the individual atoms can be achieved by the their NMR frequencies. For the imaging with the spatially fixed NV sensor, relative position information of the target nuclear spin from the sensor needs to be obtained. A method to obtain two of three position parameters, a distance r and a polar angle θ, have been developed elsewhere. Here we have successfully developed a method to measure the remaining position parameter, the azimuthal angle ϕ, for the complete determination of the target nuclear spin position with the atomic-scale resolution. Our development to reach this far was made by step-by-step advancements. First, since the standard protocol for NMR is AC magnetometry, we have reproduced in our lab a novel AC magnetometry method recently developed by other groups that utilized synchronization with a classical clock and successfully achieved ultra high spectrum resolution of 304 μHz. Then we have moved to detection of ^{13}C nuclear spins placed within the same diamond, which is widely accepted as a testbed towards future external nuclear spin sensing. Utilizing standard pulsing protocols, we have determined the hyperfine parameters of a single ^{13}C spin, and obtained the position parameters r and θ. Then our novel ϕ determination method was developed and successfully tested with a free nuclear spin precession signal of ^{13}C prepared by dynamic nuclear polarization and manipulated by a specially developed pulse sequence of the rf phase control. As a result we have succeeded in the unique assignment of each ^{13}C position with a single lattice site resolution. Our position determination method is general and therefore capable with a future MRI of a single molecule placed on the diamond surface.

Acknowledgement

First of all, I would like to thank Prof. Kohei Itoh, my supervisor, and Dr. Eisuke Abe, who led the diamond research at Itoh group during the present thesis research. Kohei gave me a basic and important message on how to contribute to the development of science, and taught me how to determine the research purpose and direction. Eisuke has always supported the present research with a great deal of knowledge, logical composition skills, and insight, and educated me thoroughly on research methods and attitudes as a science researcher. Both teachers have also been very helpful while aiming for research funding and finding future employment. In addition, I thank the Itoh group members for revitalizing my research activities and my student life.

I would like to thank Associate Prof. Junko Ishi-Hayase and her group members and Assistant Prof. Yasuaki Monnai for their help in the research of Sec. 2.2 [Review of Scientific Instruments Vol. 87, 053904 (2016)]. Junko proposed to create an microwave antenna for NV ensemble characterization measurement, and this was the starting point of the microwave antenna research. Hayase group members, Ryushiro Fujita and Soya Saijo, also assisted the work by the supplementary measurements. Yasuaki helped me in leading the design and simulation of the microwave antenna and discussion for the paper.

I thank Associate Prof. Kai-Mei Fu and Dr. Ed Kleinsasser at UW, Associate Prof. Wen-Di Li at HKU, and Dr. Hideyuki Watanabe at AIST for their contribution in research on Chap. 3 [Applied Physics Letters Vol. 110, 192407 (2017)]. Kai-Mei lent me a highly sensitive diamond sample for a very long time, and frequently checked drafts of the paper. Ed, who carried out the original research at Fu group, Wen-Di, and Hideyuki made the diamond sample by He^+ ion implantation and CVD growth and performed basic evaluations.

Thanks to Prof. Christian Degen for allowing me to stay at ETH Zurich, and to Jonathan Zopes, Jens Boss, Segawa Takuya, and others at Degen group who were helpful during my stay. Jonathan and Jens took part in many discussions on nuclear spin measurements, and Takuya helped me with matters about living in Switzerland. This stay accelerated my research on Chap. 4 [Journal of Applied Physics Vol. 123, 161101 (2018), Physics Review B Vol. 98, 121405 (2018)] by the basic idea of a three-dimensional

nuclear spin localization method based on dipole interaction modified by DC field pulses generated from a RF coil.

I also thank Associate Prof. Kazuya Ando and Prof. Shinichi Watanabe for patient discussion for examination of the present thesis.

I acknowledge JSPS for Grant-in-Aid for Research Fellowship for Young Scientists (DC1) No. JP17J05890. It has supported my research with the workstation computers for numerical simulation of the measurement protocols and analysis, Field-Programmable-Gate-Array for further development of measurement methods, and a monthly subsidy of 200,000 yen for paying tuition and living expenses.

Finally, I would like to thank my family for their support of daily life.

Contents

Chapter 1

Introduction

1.1 Background

A nitrogen-vacancy (NV) center in diamond, which is utilized as a quantum sensor in this thesis, has been in the focus of intense research for almost 40 years.

In late 1970s, an optical transition observed at 637 nm and a characteristic electron magnetic resonance spectrum obtained with irradiated diamonds were assigned successfully to the NV center in diamond [1, 2]. In 1980s, fluorescence intensity related with the NV electric ground spin state was identified in a hole burning experiments [3], and, together with microwave irradiation, optically detected magnetic resonances (ODMR) of NV centers in a bulk of diamond was examined [4,5]. In 1997, Gruber *et al.* demonstrated ODMR of single NV centers, i. e., single electron spin detection, at room temperature using a scanning confocal optical microscope [6]. The single NV centers are created via appropriate does of electron irradiation and subsequent annealing of type Ib synthetic diamond, whose concentration of nitrogen impurities is high.

Jörg Wrachtrup, a researcher who led the study of single NV magnetic resonance, has been a professor at Stuttgart University since 2000 and has continued his research on single NV magnetic resonance. Then, in 2004 at Wrachtrup group, by employing appropriate microwave and radio-frequency pulse sequences, Jelezko *et al.* demonstrated the coherent control of a single electron spin of the NV center [7] and resolved a strongly coupled single ^{13}C nuclear spin to the NV electron spin [8]. This successful demonstration of two-qubit manipulations with the NV electron spin and ^{13}C nuclear spin at room temperature has triggered a basic research aimed at applying the NV centers to quantum information processing such as quantum computing and quantum communication.

From 2005 to 2006, in collaboration with Jan Meijer (Ruhr University), Steven Prawer (University of Melbourne) and Philip Hemmer (Texas A&M University), Wrachtrup group

created single NV centers and a pair of NV center and nitrogen paramagnetic defect by nitrogen ion implantation into high-purity natural IIa diamond substrate [9–11]. Wrachtrup group also measured the NV center's optical properties by taking advantage of the narrow linewidth characteristics of NV centers originally present in the high-purity diamonds. Mikhail Lukin (Harvard University) who theoretically proposed usage of NV centers for quantum communication in 2005 [12], obtained high-purity diamond through joint research with Wrachtrup group. They investigated the dynamics of single NV centers affected by ^{13}C nuclear spins [13] and demonstrated quantum register based on a single ^{13}C nuclear spin strongly coupled with a single NV center [14]. At that timing, such high-purity natural diamond was very rare. Not many researchers used long coherence high quality NV centers. For example, David Awscharom (University of California Santa Barbara), who had not collaborated with Wrachtrup group, continued investigation on coupling between single NV center and nitrogen paramagnetic defects mainly through experiments using commercially available (Sumitomo Electric Industires) synthetic Ib diamond [15–19].

An electron spin of a single NV center in such high-purity diamond has coherence time of ~ 300 μs which is longer than the one found in Ib diamond. This long coherence time is preferred as a single qubit. However, for quantum computing applications, coupling as multi-qubits and selective initialization and manipulation are required, but how to realize them are still open questions. Researcher searched application of NV centers which can be realized only with single spin operations.

Then, in 2008, Taylor *et al.* proposed an application of the NV centers, namely quantum sensors for highly sensitive magnetometry [20]. Here two general directions were proposed; 1) using a single NV electron spin as a probe for scanning magnetometry [21, 22] and 2) using NV electron spins in an ensemble array as pixels for optical magnetic imaging. In both cases, DC and AC magnetic field sensing would be possible using microwave pulse protocols developed in conventional NMR such as Ramsey, Hahn-echo, and dynamical decoupling sequences. This proposal caught attentions of the community because the sensitivity and spatial resolution that could be theoretically achieved by the single NV electron spin outperformed those by conventional ESR, NMR, and MRI. As already demonstrated by the single ^{13}C nuclear detection [8], if a single NV electron spin could be brought very close (a few tens of nanometers) to the target nuclear spins, it could detect surrounding individual nuclear spins leading to single molecule imaging. Such performances could not be achieved by conventional NMR using inductive coils [23]. In the same year, nanoscale AC magnetometry using NV centers in nanodiamond [24] and high resolution magnetic imaging using a single NV center in a nanodiamond combined with atomic force microscope [25] were successfully demonstrated. In the same year,

Christian Degen (IBM) also proposed NV scanning magnetometry for the spin detection application [26].

Element Six has started supplying commercial high-purity IIa diamond synthesized by the plasma enhanced chemical vapor deposition (CVD) method [27]. Since 2009, such synthetic high-purity diamonds have been used by many NV research groups, such as Hewlett Packard [28–31], Delft University [32], University of California Berkeley [33, 34], and so on. The CVD method was also used for the ^{12}C isotope purification of diamond, and the single NV coherence time was extended to about 2 ms [35] providing high sensitivity and high resolution of NV magnetometry.

During 2010–2012, another directions of magnetometry, the optical magnetic imaging using NV ensembles in bulk [36] or near surface [37, 38], was demonstrated. Lukin group observed entanglement between NV electron spin state and polarization of emitted red photon [39], and it opened the way for quantum communication based on single NV centers. A fundamentally new electric-field sensing using single NV centers was also demonstrated in Wrachtrup group [40]. The external electron spin detection was also demonstrated using shallow, meaning very close ($\sim$10 nm) to the diamond surface, NV centers [41, 42]. Moreover, in parallel, even though it was a ^{13}C situating inside the diamond, a single ^{13}C nuclear spin weakly coupled to the single NV sensor was detected using the dynamical decoupling, and its hyperfine parameters were extracted for the identification of the target spin positions [43–45]. The application range of NV centers has begun to expand.

During 2013–2014, a very small number of external proton nuclear ensemble spins placed on the diamond surfaces was detected by a single shallow NV center [46–48]. The detection volume, which directly reflected the NMR spatial resolution and sensitivity, was down to $(5\ \text{nm})^3$ by creating shallow NV centers using low energy ion implantation [47] and CVD nitrogen delta doping [48]. Subsequently such detection volume reduced down to 1.9 nm by etching the diamond surface [49]. Realization of external ensemble proton NMR in turn made it possible to estimate the depth of the NV sensor, i. e., the distance from the diamond surface [50]. Then came a time when single nuclear spin detection was demonstrated. Müller *et al.* detected single ^{29}Si nuclear spins with dynamical decoupling [51], while Sushkov *et al.* indirectly detected single proton spins on the diamond surface by probing the dynamics of the surface electron spins [52].

In the course of above mentioned advancements, the sensitivity and resolution were constantly improved by modification of the instrumentation and development of new pulse protocols. High resolution spectroscopy of ^{13}C spin bath was demonstrated [53] by the correlation spectroscopy [54]. The NMR sensitivity was enhanced by utilization of the double quantum transition [55]. A three-dimensional imaging of electron spins

with subnanometer resolution was demonstrated using strong field gradient applied by a scanning magnetic probe [56].

1.2 The works presented in this thesis and related works

The present author started the NV research described in this thesis in the Itoh group at Keio University in 2015. In close collaboration with Dr. Eisuke Abe, who was also a member of the Itoh group, we started from designing and setting up of the measurement system compatible with ODMR spectroscopy based on single NV centers. At that time, in collaboration with Dr. Hideyuki Watanabe of AIST, Itoh group was leading the technology to produce shallow single NV centers suitable for sensing by nitrogen doping using CVD method. We mainly studied from three viewpoints: microwave engineering, materials science, and sensing protocol development.

In NV measurement, a magnetic field application method and a microwave irradiation method different from those of conventional ESR are used, so it was necessary to examine and verify a more suitable microwave irradiation method. In conventional ESR, the magnetic field is adjusted by tuning the amount of current flowing through the electromagnet and the rotation of the sample. ESR is detected by detecting the change of the absorption of the microwaves at the resonance frequency of the three-dimensional microwave resonator with the sample inserted during sweeping the magnetic field strength. On the other hand, in NV measurement, in order to obtain a high spatial resolution and a high signal-to-noise ratio, a confocal system using an objective lens having a high numerical aperture and a short working distance is widely used. Therefore, it is difficult to perform measurement using a sample rotation or a three-dimensional microwave resonator like conventional ESR. For applying a magnetic field, it is common to use a small permanent magnet that does not obstruct optical measurement, and the magnetic field strength and angle are adjusted by its position. Since the method is not good at sweeping the magnetic field strength at regular intervals like an electromagnet, the microwave frequency is swept in ODMR spectroscopy with the magnetic field strength fixed. Therefore, the microwave irradiation antenna is required to have a shape that can apply a sufficient microwave intensity in a wide band and does not hinder optical measurement. The technique used in the early NV research was the technique using copper wires and coils, but the weak point was that each could only measure a spatially narrow range and the low microwave intensity.

In sample characterization, a wide range of measurements is suitable to evaluate more

NV centers because they are created at random sites in the diamond lattice. In order to obtain important parameters such as coherence time, the measurement using strong microwave pulses is required. The requirement for microwave application on wide-field magnetic imaging using NV ensembles is also the same. We dealt with these problems by devising the shape of the planar single slit loop resonator antenna and widening the bandwidth (Sec. 2.2). In order to lower Q value, the capacitance was increased by using a large copper plate around the ring antenna, and the resonance frequency was tuned to a frequency suitable for NV center by adjusting the position of the loop. The fabricated antenna was evaluated by pulsed measurement to confirm high spatial uniformity and broadband characteristics. This antenna was used for the initial evaluation of diamond samples. After the high quality characteristics of NV centers were confirmed with the antenna, advanced sample evaluation, sensing measurement and protocol development were performed using a copper wire antenna. In addition, we also developed a circularly polarized antenna that can selectively excite the two resonances of NV for further protocol development [57].

As mentioned above, Itoh group was leading the technology in the field of materials science, which was the creation of single NV centers with stable and long coherence near the diamond surface. Conventionally, it has been known that the charge of NV center is difficult to stabilize near the surface due to the influence of p-type defects [28] or surface terminations [58], but this is overcome by a technology that electrically stabilizes NV by doping nitrogen at a high concentration by CVD method. In addition, noise less coherence property was obtained in combination with ^{12}C isotope purification technique. The CVD method at AIST has a very high quality as diamond, so it is difficult to form vacancies. The efficiency of NV center generation against nitrogen is low. On the other hand, the generation of NV ensembles near surface has also been demanded for a wide-field optical magnetic imaging applications. In 2016, Kai-Mei Fu's group at the University of Washington collaborated with AIST and Wen-Di Li's group at Hong Kong University to create holes in the nitrogen doped CVD diamond thin film (100 nm) while suppressing damage by He^+ ion implantation [59]. They succeeded improving the NV generation while maintaining the narrow line width of the previous state, and obtained a highly sensitive NV ensemble near surface.

Nitrogen impurities are accepted as a main cause of decoherence, so that the ratio of the density of nitrogen donor paramagnetic defect, P1 center, and the density of NV centers is recognized as a representative parameter for sample evaluation. However, in the case of a sensing diamond chip having a doped layer only in the vicinity of its surface, it is difficult to measure the P1 density with conventional ESR. In 2016, P1 center detection in a bulk diamond was performed elsewhere using the simultaneous resonance

conditions [60] and the double electron-electron resonance technique [61,62]. These methods is suitable for local electron spin detection in the vicinity of NV center, and could be applied to quantitative evaluation of P1 density in CVD thin film. We borrow the samples from Fu group and evaluated it with with pulsed measurement (Chap. 3). First, the experiment conducted by Fu group, DC magnetic field sensitivity evaluation by continuous wave experiment, was reproduced. We also evaluated the sensitivity of the DC magnetic field when the sensitivity was further increased using nuclear spin polarization and pulsed measurement. After that, instant diffusion under the simultaneous resonance condition with paramagnetic defects $S = 1/2$ was measured, and quantitative evaluate the paramagnetic impurity density in CVD thin film was performed.

Independently, Itoh group has also developed a near-surface single NV center generation technique using ion implantation through a SiO_2 mask into high-purity diamond [63]. The present author cooperated with characterization of coherence of the created NV centers. The materials science based on these sample evaluations will lead to the realization of diamond tips containing near-surface NV centers that enable high resolution magnetic imaging and detection of external molecules.

Since 2017, the author has begun protocol development for nuclear spin detection. In previous works, the protocol development has brought many achievements towards sensing applications. For example, sensor coherence enhancement and sensitivity improvement by dynamical decoupling [64–69], unambiguous identification of nuclear species [70–72], precise determination of nuclear spin position parameters (distance r, polar angle θ) [71], enhancement of sensor readout contrast [73–75] and frequency resolution using nuclear spin memory [76–78]. Until 2017, some of them are used for demonstration of single molecule NMR detection [79] and highly sensitive detection of chemical shift at high magnetic field [80]. For single molecule MRI, which is one of an ultimate goal of NMR using a single NV center, determination of three-dimensional nuclear spin positions and detection of fine shifts in NMR frequencies (chemical shift and J coupling) are required for pinpointing and identifying functional groups in a molecule.

First, the present author visited Christian Degen's group, who moved to ETH as a professor in 2011 and led the technology in the field of nuclear spin detection, and gained knowledge for nuclear spin detection for a month and a half. In the process, the author cooperated the improvement of sample resolution in AC magnetometry using shaped pulses [81], and development of three-dimensional nuclear spin position determination technique using DC magnetic field pulse [82]. In the same year, a paper on AC magnetic field detection with ultrahigh frequency resolution independently developed by ETH [83], Ulm [84], and Harvard [85] was published or appeared on the Web site (arXiv). The frequency resolution previously limited to the relaxation time of electron spins or nuclear

spins has been improved to the stability of classical clocks, and Harvard has achieved chemical shift and J coupling detection with picolitre detection volume at low magnetic field. After returning to Keio, the present author implemented this AC magnetometry technique and succeeded in reproducing the extremely high frequency resolution of 304 μHz (Sec. 4.1). In addition, we devised dynamic nuclear magnetic polarization [86] and radio wave pulse irradiation methods, and based on these technologies, we succeeded in detecting the free precession of ^{13}C spin bath in diamond. In the middle of this technological development, we noticed that there was a correlation between the precession phase of nuclear spins and radio-wave irradiation and came up with the idea of application for determination of three-dimensional nuclear spin position. We demonstrated it by pinpointing a unique lattice site of a single ^{13}C nuclear spin in diamond (Sec. 4.2). After that, independent work on nuclear spin detection and localization method using similar methods have also been demonstrated at Stuttgart [87] and ETH [88, 89]. More recently, at a cryogenic temperature, determination of 27 ^{13}C nuclear spin positions near a single NV center was demonstrated at Delft University [90]. Building blocks in protocol development for single molecule structure analysis are getting ready.

1.3 Organization

The present thesis is based on three papers I published as first-authors [91–93].

Chapter 2 introduces fundamental properties of NV centers and the homebuilt ODMR measurement setup. The measurement instruments for the development of spin sensing protocols were described, and specially designed microwave antennas [91] developed for characterization of diamond samples are described.

Chapter 3 examines the sensitivity for DC magnetometry with the dynamic nuclear polarization, and electron spin sensing by the decoherence spectroscopy. Pulse measurement protocols are developed for a novel diamond sample [59] having the high NV density ($\sim$ 1 ppm) near the surface with the very narrow ensemble electron spin linewidth ($\sim$ 200 kHz).

Chapter 4 first demonstrates an application of a novel AC magnetometry protocol [83–85] to achieve 304 μHz resolution using our experimental setup. Then describes the development of nuclear magnetic resonance protocols for absolute nuclear spin lattice site position determination, followed by experimental demonstration of the successful assignment of a single ^{13}C spin lattice site in diamond [93].

Chapter 5 provides conclusions and outlook of NV-based spin magnetometry.

Chapter 2

Experimental setup for optically detected magnetic resonance

Our experiments are based on unique spin-optical characters of the negatively charged nitrogen-vacancy (NV) center in diamond. The first section of this chapter (Sec. 2.1) describes properties of NV centers followed by experimental setups to utilize NV centers as sensors. The second section (Sec. 2.2) describes a newly developed microwave antenna that allows for efficient optically detected magnetic resonance (ODMR) characterization of NVs in diamond.

2.1 Optically detected magnetic resonance

2.1.1 Properties of nitrogen-vacancy center in diamond

Figure 2.1(a) shows a structure of a nitrogen-vacancy (NV) center in diamond. The NV is a pair of a substitutional nitrogen atom and a neighboring vacancy. The nitrogen atom and the vacancy are aligned parallel to one of four $\langle 111 \rangle$ crystallographic axes of diamond lattice ([111], $[\bar{1}\bar{1}1]$, $[1\bar{1}\bar{1}]$, and $[\bar{1}1\bar{1}]$). Therefore $\langle 111 \rangle$ is the symmetry axis of NV center, and it shows C_{3v} point group symmetry together with the three adjacent carbon atoms.

A negatively charged state NV^- is one of stable charge states, and it has spin-optical properties that allow for ODMR. There is another possible stable charge state called NV^0, which is not ODMR active. Since magnetometry is the main topic of this thesis, we focus exclusively on NV^-; NV in the present thesis refers to NV^- otherwise noted.

The NV^- center has six electrons, which are supplied from dangling bonds of the three carbon atoms and the nitrogen atom, and an extra electron released from a surrounding donor defect. The dangling bonds form two A_1 and two degenerated E molecular or-

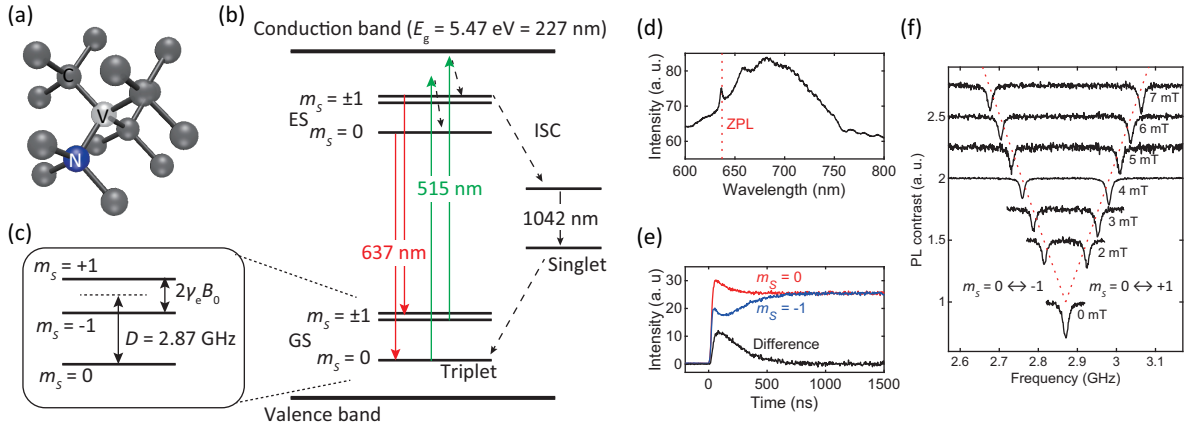

Figure 2.1: (a) Defect structure of a nitrogen-vacancy center. (b) Electronic energy levels diagram of a NV center. GS: ground state; ES: excited state; ISC: intersystem crossing. (c) Photoluminescence spectrum under green (515 nm) laser excitation. ZPL: zero-phonon line at 637 nm. (d) Time-resolved fluorescence. An excitation laser is turned on at $t = 0$ s. (e) Optically detected magnetic resonance as sweeping microwave frequency. PL contrast is defined as the ratio of the PL intensities with and without the microwave irradiation. Offsets, $0.25B_0$, are introduced for mitigating overlaps between data taken at different magnetic field strengths B_0. The red dashed lines represent positions of expected resonance frequency $D \pm \gamma_e B_0$.

bitals [94]. The energy of E orbits are higher than the A_1 orbits, and thus A_1 orbits are filled by four electrons. In the ground state, the remaining two electrons occupy each of E orbit, and they exhibit a spin triplet state $S = 1$. It is this spin triplet state that is utilized as a single spin for sensing in the present and many of other NV quantum sensing works.

Figure 2.1(b) shows an energy diagram of the NV center [95,96]. There are two triplet states separated by the wavelength of 637 nm, situating between a bandgap of diamond (227 nm), and two singlet states separated by 1042 nm situating between the two triplet states.

A spin energy diagram is shown in Fig. 2.1(c). The ground state of NV center is spin triplet. The energy separation between $m_S = 0$ and $m_S = \pm 1$ states is 2.87 GHz, and is called zero-field splitting D. The major contribution to the term is the dipole electron-electron spin interaction between E orbit electrons. When magnetic field of B_0 is applied parallel to the NV symmetry axis, $m_S = \pm 1$ states are lifted by Zeeman effect, and the energy separation between $m_S = -1$ and $m_S = +1$ becomes $2\gamma_e \boldsymbol{B}_0$, where $\gamma_e = 28$ MHz/mT is gyromagnetic ratio of the NV's electron spin. The Hamiltonian of such spin triplet is given as,

$$H = D\hat{S}_z^2 + \gamma_e \boldsymbol{B}_0 \cdot \hat{\boldsymbol{S}}, \tag{2.1}$$

where $\boldsymbol{B}_0$ is applied magnetic field vector. Here I define that z axis is parallel to the NV symmetry axis. $\hat{S}_z$ and $\hat{\boldsymbol{S}}$ are the electron spin operators for $S = 1$, and the all components are given as,

$$\hat{S}_x = \frac{1}{\sqrt{2}} \begin{pmatrix} 0 & 1 & 0 \\ 1 & 0 & 1 \\ 0 & 1 & 0 \end{pmatrix}, \hat{S}_y = \frac{1}{\sqrt{2}} \begin{pmatrix} 0 & -i & 0 \\ i & 0 & -i \\ 0 & i & 0 \end{pmatrix}, \hat{S}_z = \begin{pmatrix} 1 & 0 & 0 \\ 0 & 0 & 0 \\ 0 & 0 & -1 \end{pmatrix}. \tag{2.2}$$

See Appendix B.2 of Ref. [97] for the spin operators for $S > 1/2$. The zero-field splitting has only a z direction component, so that the energy levels are also magnetic field direction dependent. I only show the case when $\boldsymbol{B}_0$ is parallel to z axis for simplicity, and general case is shown in Sec. 2.1.7 and Sec. 2.2. The excited state considered in this work is also spin triplet, and it is also described by Eq. (2.1) with zero-field splitting of $D = 1.42$ GHz.

Optical excitation from the ground triplet state to the excited triplet state is enabled by light illumination, whose wavelength is shorter than 637 nm. However, green light at 510–540 nm is preferred for suppression of the NV^- population loss induced by photoionization [98]. This optical excitation is spin conserving transition. For example, when an electron is excited from from the high energy A_1 orbit, it goes to one of the E orbits to satisfy the Pauli exclusion principle, and an unpaired electron in another E orbit and an electron remaining in the A_1 orbit conserve the total spin state for $S = 1$ [99].

A direct decay from the excited triplet state to the ground triplet state is also spin conserving and accompanies a single photon emission. Figure 2.1(d) is a photoluminescence (PL) spectrum of a single NV center in diamond with 515 nm excitation taken at ambient condition. A zero-phonon line (ZPL) is observed as a small sharp peak at 637 nm, whereas the phonon sideband associated with phonon emissions spreads to 800 nm. The phonon sideband is due to the relatively slow local strain relocation during transition compared to the instantaneous reconfiguration of the electron state (Frank–Condon principle).

The decay from the excited triplet state to the excited singlet state, intersystem crossing (ISC), is also possible. This transition rate is spin dependent due to transverse spin-orbit interaction [99], and the transition rate from $m_S = \pm 1$ of the excited triplet state is much higher than that from $m_S = 0$ of the excited triplet state. The excited singlet state decays to the ground singlet state by emitting a single infrared photon at 1042 nm. The ground singlet state then decays to the $m_S = 0$.

These spin dependent transitions associated with the singlet states are utilized in the present work for optical initialization and readout of NVs by ODMR. $m_S = \pm 1$ state often decays to $m_S = 0$ state, but the probability for the opposite direction is small. Through continuous green light illumination, i.e., many optical transition cyclings, the spin state is stochastically but efficiently initialized to $m_S = 0$ even at room temperature. While the excitation from $m_S = 0$ goes back to $m_S = 0$, that from $m_S = -1$ goes to $m_S = 0$, so this initialization is efficient. The singlet state to the ground state transition is non-radiative so the red photon (600–800 nm) emission does not occur during the initialization process from $m_S = -1$ to $m_S = 0$. The readout at room temperature is also possible by utilizing the spin dependent PL intensity; the PL intensity for $m_S = 0$ state is much higher than that for $m_S = -1$, so the two-level readout is possible by the counting of red photons.

Figure 2.1(e) shows the time-resolved fluorescence of a single NV center in diamond during green laser excitation. The green laser is tuned on during $t \geq 0$ s to observe the fluorescence. Since the single NV fluorescence is weak, ~ 100 kcps, the signal is taken by averaging over many fluorescence cycles. PL intensity during $0 \leq t \leq 1$ μs for $m_S = 0$ is higher than $m_S = -1$ due to the spin dependent fluorescence. The initialization time from $m_S = -1$ to $m_S = 0$ through the green light excitation is about 1 μs.

ODMR (or continuous wave ODMR) is carried out by observing such a spin dependent PL intensity under the continuous microwave irradiation. Figure 2.1(f) shows ODMR spectra of a single NV center in diamond as sweeping microwave frequency. At zero-magnetic field ($B_0 = 0$ mT) $m_S = \pm 1$ levels are degenerated so the transition frequencies from $m_S = 0$ to $m_S = \pm 1$ are the same zero-field splitting $D = 2.87$ GHz. By applying the magnetic field parallel to the NV symmetry axis, they are resolved by $2\gamma_e B_0$ [see also Fig. 2.1(c)]. The resonance frequency for $m_S = 0 \leftrightarrow -1$ ($0 \leftrightarrow +1$) follows $D - \gamma_e B_0$

$(D + \gamma_e B_0)$ as expected.

For magnetometry application, the magnetic field is estimated from the shift in the resonance frequency $\Delta f_{\rm res}$ from zero-field splitting by $\Delta B_0 = -\Delta f_{\rm res}/\gamma_e$ for $m_S = 0 \leftrightarrow -1$ resonance. The DC magnetic field sensitivity is thus proportional to precision in the resonance frequency and narrowness in the linewidth. Also high PL intensity and high PL intensity contrast between microwave on and off are needed for high sensitivity. These parameters are not only limited by environment spin impurities but also the measurement condition, such as laser intensity, microwave intensity, and photon collection efficiency of the microscope.

2.1.2 Diamond sample

In the present thesis, we use a diamond sample fabricated with chemical vapor deposition (CVD). An ultra pure IIa diamond (Element Six electronic grade) containing NV centers at very low density, a single NV center per $\sim (10\ \mu\text{m})^3$ volume, is used for single NV measurements. A typical NV coherence is $\sim 300\ \mu$s, and it is long because the diamonds contain few paramagnetic impurities. The diamonds are not ^{12}C isotopically purified, thus they contain ^{13}C isotopes which have nuclear spin $I = 1/2$ at natural abundance of 1.1 % (1.95×10^{21} cm^{-3}). The ^{13}C density corresponds to the average distance between ^{13}Cs is about 8 Å, and the coherence of NV center can be limited by these ^{13}C nuclear spins. Since the single NV centers have a long coherence time and surrounding ^{13} nuclear spins, the sample is useful for testbed of single spin NMR.

The pure diamond is also used as the substrate material when creating NV centers on the diamond surface for sensing. When creating NV centers on the surface, a nitrogen-doped diamond thin film is created on the substrate surface by strictly calibrating the growth rate of CVD. The NV density changes according to the nitrogen doping amount, and from single NV centers to NV ensembles can be created near surface. Methane gas purified to ^{12}C isotope are often used to remove ^{13}C nuclear spin noise to enhance coherence time and sensitivity. Since natural vacancy generation is less compared to the ion implantation, conversion efficiency from nitrogen impurities to NV centers is improved by performing a process of intentionally creating vacancies by He^+ implantation (Chap. 3). The vertical positions of the NV centers are confined in the thin film grown by the CVD, the depth distribution of the NV does not unintentionally spread due to the ion channeling unlike the ion implantation method. In the ion implantation method, the depth distribution can be controlled by using dry etching [49] or a SiO_2 implantation mask [63].

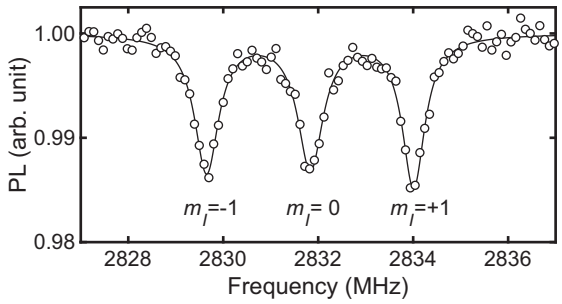

Figure 2.2: ODMR spectrum corresponds to transition between $m_S = 0 \leftrightarrow -1$. Three resonance signals associated with each of the nuclear spin states $m_S = 1$, 0, and -1 are resolved.

2.1.3 Hyperfine structure associated with nitrogen nuclear spin

Strictly speaking, because the major stable isotope of nitrogen, ^{14}N (99.6 %, $I = 1$), has a nuclear spin, the transition frequency between $m_S = 0 \leftrightarrow -1$ (or $m_S = 0 \leftrightarrow +1$) is split into three. To include the hyperfine coupling between the electron spin and nitrogen nuclear spin, the Hamiltonian of the spin triplet is modified as

$$\hat{H} = D\hat{S}_z^2 + \gamma_e B_0 \hat{S}_z - \gamma_N B_0 \hat{I}_z + A_z \hat{S}_z \hat{I}_z + A_{xy}(\hat{S}_x \hat{I}_x + \hat{S}_y \hat{I}_y) + P\hat{I}_z^2, \qquad (2.3)$$

where $\gamma_N = 3.08$ kHz/mT is the gyromagnetic ratio of nuclear spin, $A_z = -2.14$ MHz and $A_{xy} = -2.70$ MHz are the hyperfine parameters [100], $P = -5.01$ MHz is the quadrupole interaction of nitrogen nuclear spin, and $\hat{I}_x$, $\hat{I}_y$, $\hat{I}_z$ are nuclear spin operators for $I = 1$ which are similar to Eq. (2.2). Here I considered that magnetic field is applied parallel to the NV symmetry axis. The main contribution to A_z and A_{xy} are Fermi-contact interaction. The gyromagnetic ratio of ^{14}N is positive and the corresponding hyperfine parameters are negative. This is because the ground state electrons situates closer to the vacancy position within the NV and electron spin density around the nitrogen can be considered negative [101]. The quadrupole interaction is internal interaction of nuclear spin $I = 1$, and it does not split the electron spin transition frequencies.

Figure 2.2 is a high resolution ODMR spectrum corresponds to transition between $m_S = 0 \leftrightarrow -1$ taken under mitigation of the linewidth broadening related with optical initialization and strong microwave field by suppression of excitation powers. The three dips corresponding to nuclear spin states ($m_I = -1$, 0, and $+1$) are clearly resolved. The separations between adjacent/neighboring dips are close to A_z.

Additionally, there are also hyperfine interactions ($A_z \sim 40$ MHz and $A_{xy} \sim 40$ MHz) in the excited triplet state [102]. They are significantly larger than those of the ground

state because of the increased spin density at the nitrogen atom position. This strong $A_{xy}(\hat{S}_x\hat{I}_x + \hat{S}_y\hat{I}_y)$ interaction mixes excited spin states with the same total spin angular momentum, $m_S + m_I$, and it causes a flip-flop between the electron spin and the nuclear spin at a level crossing condition at ~ 50 mT (see Chap. 3).

2.1.4 Coherent control of NV electron spins

As conventional pulsed ESR techniques, it is possible to coherently control the electron spin of the NV center with microwave pulses because the NV electron spin normally has a long coherence time even at ambient conditions. This technique is critical for magnetometry of oscillating magnetic signals with constant phases, such as microwave itself, AC magnetic field, and nuclear spins.

In order not to initialize during the spin operation by the microwave, the laser is irradiated only during initialization and readout. Sensor signal readout is calculated as the sum of photon counting for ~ 1 μs from the start of laser irradiation, and initialization is performed by continuously irradiating the laser for a few microseconds [see Fig. 2.1(e)]. The sequence are repeated many (in most case $> 10^4$) times to acquire enough photon counts to ensure high signal to noise ratio.

Spin motion in a rotating frame

A rotating frame is a convenient way to explain the coherent manipulation of spins using microwaves field described as,

$$\boldsymbol{B}_{\mathrm{mw}} = B_{\mathrm{mw}} \cos(2\pi f_{\mathrm{mw}} t)\boldsymbol{e}_x \tag{2.4}$$

where $\boldsymbol{e}_x$ is an unit vector parallel to x axis (any specific axis perpendicular to z axis). Here, for simplicity, we consider only electron spin transition using Eq. (2.1) and the magnetic field applied parallel to NV axis. Eq. (2.1) is thus rewritten as,

$$\hat{H} = D\hat{S}_z^2 + \gamma_{\mathrm{e}} B_0 \hat{S}_z \tag{2.5}$$

$$= \begin{pmatrix} D + \gamma_{\mathrm{e}} B_0 & 0 & 0 \\ 0 & 0 & 0 \\ 0 & 0 & D - \gamma_{\mathrm{e}} B_0 \end{pmatrix}. \tag{2.6}$$

This Sec. 2.1.4 is reproduced from the present author's master degree thesis.

When the microwave field is applied, the Hamiltonian is rewritten as,

$$\hat{H} = D\hat{S}_z^2 + \gamma_e B_0 \hat{S}_z + \gamma_e B_{mw} \cos(2\pi f_{mw} t)\hat{S}_x \tag{2.7}$$

$$= \begin{pmatrix} D+\gamma_e B_0 & \frac{\gamma_e B_{mw}}{\sqrt{2}}\cos(2\pi f_{mw}t) & 0 \\ \frac{\gamma_e B_{mw}}{\sqrt{2}}\cos(2\pi f_{mw}t) & 0 & \frac{\gamma_e B_{mw}}{\sqrt{2}}\cos(2\pi f_{mw}t) \\ 0 & \frac{\gamma_e B_{mw}}{\sqrt{2}}\cos(2\pi f_{mw}t) & D-\gamma_e B_0 \end{pmatrix}. \tag{2.8}$$

The Hamiltonian is put in a rotation frame using following equation,

$$\hat{H}' = \left[U(t)^\dagger \hat{H} U(t) - \hat{H}_{rot}\right], \tag{2.9}$$

where $U(t) = e^{-2\pi i \hat{H}_{rot} t}$ is rotation operator.

When $\hat{H}_{rot} = -f_{mw}\hat{S}_z$, Eq. (2.9) is explicitly given as,

$$\hat{H}' = \begin{pmatrix} f_+ + f_{mw} & \frac{\gamma_e B_{mw}}{2\sqrt{2}}(1+e^{4\pi i f_{mw} t}) & 0 \\ \frac{\gamma_e B_{mw}}{2\sqrt{2}}(1+e^{-4\pi i f_{mw} t}) & 0 & \frac{\gamma_e B_{mw}}{2\sqrt{2}}(1+e^{4\pi i f_{mw} t}) \\ 0 & \frac{\gamma_e B_{mw}}{2\sqrt{2}}(1+e^{-4\pi i f_{mw} t}) & f_- - f_{mw} \end{pmatrix} \tag{2.10}$$

where $f_+ = D + \gamma_e B_0$ and $f_- = D - \gamma_e B_0$ are NV's resonance frequencies. In a rotating wave approximation, fast-oscillating components, $e^{4\pi i f_{mw} t}$ and $e^{-4\pi i f_{mw} t}$, are ignored, and the Eq. (2.10) is simplified as,

$$\hat{H}' = \begin{pmatrix} 2D-\delta & \frac{\gamma_e B_{mw}}{2\sqrt{2}} & 0 \\ \frac{\gamma_e B_{mw}}{2\sqrt{2}} & 0 & \frac{\gamma_e B_{mw}}{2\sqrt{2}} \\ 0 & \frac{\gamma_e B_{mw}}{2\sqrt{2}} & \delta \end{pmatrix}, \tag{2.11}$$

where $\delta = f_- - f_{mw}$ is detuning between the microwave frequency and the actual resonance frequency. In this rotating frame, the energy of $m_S = 0$ and $m_S = -1$ states are same when $\delta = 0$, whereas the energy of $m_S = +1$ state is higher than the other state by $2D$. In most case $\frac{\gamma_e B_{mw}}{2\sqrt{2}} \ll 2D - \delta$ is satisfied, and spin state transition to $m_S = +1$ from other states can be ignored. Therefore, the spin dynamics of $m_S = 0$ and $m_S = -1$ states is described by a subspace given as,

$$\hat{H}' = \begin{pmatrix} 0 & \frac{\gamma_e B_{mw}}{2\sqrt{2}} \\ \frac{\gamma_e B_{mw}}{2\sqrt{2}} & \delta \end{pmatrix} = -\delta\hat{S}_z + \frac{\gamma_e B_{mw}}{\sqrt{2}}\hat{S}_x. \tag{2.12}$$

Here the spin operators, $\hat{S}_x$, $\hat{S}_y$, and $\hat{S}_z$, are rewritten in the subspace by spin operators for $S = 1/2$,

$$\hat{S}_x = \frac{1}{2}\begin{pmatrix} 0 & 1 \\ 1 & 0 \end{pmatrix}, \hat{S}_y = \frac{1}{2}\begin{pmatrix} 0 & -i \\ i & 0 \end{pmatrix}, \hat{S}_z = -\frac{1}{2}\mathbf{1} + \frac{1}{2}\begin{pmatrix} 1 & 0 \\ 0 & -1 \end{pmatrix}. \tag{2.13}$$

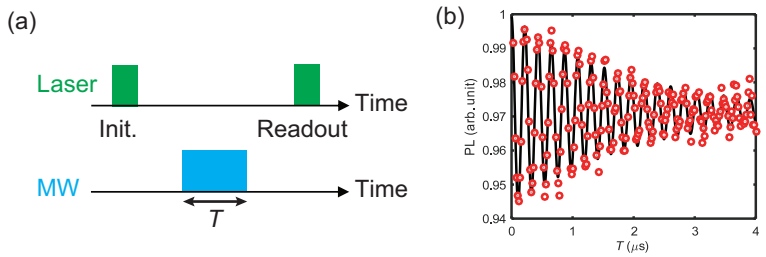

Figure 2.3: (a) Pulse sequence for Rabi oscillation. (b) An example of Rabi oscillation as sweeping microwave pulse duration T. The solid line is fitting $A\exp(-T/T_{\mathrm{R}})\cos(2\pi f_{\mathrm{R}}T)+B$.

Therefore, the NV's electron spin dynamics in the subspace can be interpreted by a Bloch sphere and a Bloch vector, similar to the spin 1/2 systems. The detuning δ acts as a static magnetic field in the z direction, and the microwave magnetic field B_{mw} acts as a static magnetic field in the x direction. The microwave magnetic field direction in the rotating frame can be adjusted by the phase of microwave. Since the Hamiltonian in rotating frame [Eq. (2.12)] is time independent, the NV's electron spin precesses around the total magnetic field. On the other hand, there is a difference of a factor of $\sqrt{2}$ on the amplitude of field along x (or y), due to the difference in the amplitude of

Rabi oscillation

Rabi oscillation is one of the simplest pulsed measurements and is used for microwave strength measurement (see Sec. 2.2) and calibration of further advanced magnetometry protocols. Figure 2.3(a) shows a Rabi oscillation sequence. The spin state is initialized into $m_S = 0$ by irradiating the green laser at the start of the sequence, and the sensor state is coherently driven between $m_S = 0$ and $m_S = -1$ during a microwave pulse irradiation, whose length is T. At the end of the sequence, the photon counting reflecting probability of $m_S = 0$ state is carried out by irradiating the laser again.

Figure 2.3(b) shows an example of Rabi oscillation obtained as incrementing microwave pulse duration T. The Rabi frequency f_{R} is obtained by fitting the oscillation with exponentially decaying trigonometric function or fast Fourier transform (FFT). At the resonance condition, $\delta = 0$, Rabi frequency depends on the microwave strength perpendicular to the sensor symmetry axis and it is possible to be applied for microwave field strength sensing as shown in Sec. 2.2.

The microwave pulse duration corresponds to spin rotation angle $\pi/2$ (π) called $\pi/2$

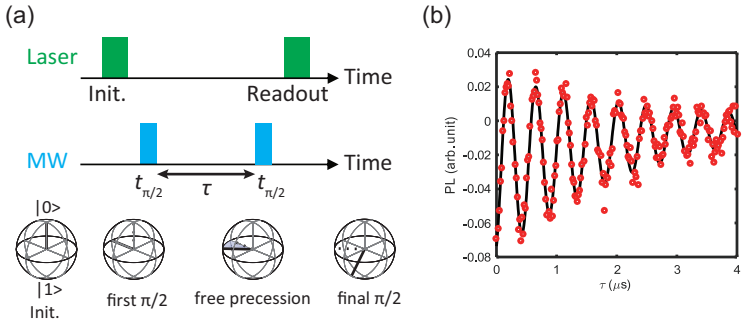

Figure 2.4: (a) Pulse sequence for Ramsey interferometry. Bloch spheres in rotating frame with microwave frequency is shown at the bottom. A unit vector pointing $+z$ ($-z$) direction is $|0\rangle$ ($|1\rangle$) which corresponds $m_S = 0$ ($m_S = -1$) state (b) An example of Ramsey interferometry as sweeping the interpulse delay τ. NV ensemble containing ^{14}N nuclear spins is measured. The solid line is fitting $-C\exp(-\tau/T_2^*)(1 + 2\cos(2\pi A_z + \phi))$, where $A_z = 2.18$ MHz is obtained from ODMR measurement.

pulse $t_{\pi/2}$ (π pulse t_π) is extracted from f_R by $t_{\pi/2} = 1/4f_\mathrm{R}$ ($t_\pi = 1/f_\mathrm{R}$). The knowledge of Rabi frequency is thus essential for creating superposition of sensor spin state and flipping of sensor spin, which are the building blocks of advanced magnetometry protocols.

By sweeping the microwave frequency of the calibrated π pulse, it is possible to perform spectroscopic measurements similar to the continuous wave ODMR. This is called pulsed ODMR spectroscopy. Unlike CW ODMR, resulting sensor state is not perturbed from the excitation light intensity, thus the suppression of PL contrast and broadening of linewidth caused by optical initialization are avoided to have high sensitivity (see Sec 3.3).

Ramsey interferometry

Using $\pi/2$ pulses, sensor spin precession is directly obtained using Ramsey interferometry. Figure 2.4(a) shows Ramsey sequence. The difference between Ramsey and Rabi sequences is obtained in microwave pulse sequence between laser pulses for initialization and readout. The sequence is consists of two $\pi/2$ pulses. The first $\pi/2$ pulse brings the sensor state into a superposition of $m_S = 0$ and $m_S = -1$ from $m_S = 0$ after initialization. The sensor's free precession occurs during the delay τ between $\pi/2$ pulses. The sensor state after the precession is rotated again by final $\pi/2$ pulse, and then spin state is readout. When the frequencies of sensor precession and microwave is completely same, $\delta = 0$, sensor does not precess in the rotating frame during the interpulse delay, and sensor state is obtained as $m_S = -1$ when readout laser pulse is applied. On the other

hand, when there are detuning between sensor resonance and microwave frequency, $\delta \neq 0$, sensor precession occurs, and the probability of sensor state oscillates between $m_S = -1$ and $m_S = 0$. As this is a precession measurement, the sensor resonance frequency is precisely obtained from FFT spectrum of the oscillation signal, thus this sequence can be utilized for precise DC magnetometry.

In an actual measurement case, we also use a sequence with final $\pi/2$ pulse with phase shifted by π. The rotation axis of the sensor spin gets opposite of the non phase shifted sequence. By taking the difference between the signals obtained in the two sequences, the oscillation contrast becomes clearer and the offset is removed, thereby facilitating the analysis.

Figure 2.4(b) shows an example of Ramsey interferometry as sweeping the interpulse delay τ. The microwave is tuned to sensor spin resonance between $m_S = 0$ and $m_S = -1$ under ^{14}N nuclear state of $m_I = 0$. The Ramsey signal is oscillating by the detuning between microwave and resonance ^{14}N nuclear state of $m_I = \pm 1$ ($A_z = 2.18$ MHz). The decay of the oscillation called dephasing is because the resonance frequency of the sensor fluctuates due to surrounding spin impurities, such as paramagnetic nitrogen defects P1 and ^{13}C isotope. The longer coherence time is desired for magnetometry because FFT spectrum of Ramsey signal gets sharper leading high precision of resonance frequency estimation.

Hahn echo

Figure 2.5(a) shows Hahn echo sequence, and the sequence has a π pulse at the middle of $\pi/2$ pulses of Ramsey sequence. The sensor spin evolution until the first free evolution is same as in Ramsey sequence. When the magnetic field is time independent, δ is constant, the sensor spin precession in second free precession is same amount as first free evolution after flipping by π pulse. As a result, the sensor acquisition phase is canceled out, and then sensor state goes to $m_S = 0$ state after final $\pi/2$ pulse. Therefore, Hahn echo is insensitive to DC magnetic field. On the other hand, when the magnetic field strength is changed between first and second free evolution, the sensor precession frequency δ changed, thus acquisition phase does not cancel out. AC magnetometry is carried out by obtaining degradation of probability of $m_S = 0$ state.

Hahn echo is a lock-in detection scheme and is sensitive to AC magnetic field with frequency $f_{\mathrm{det}} = \frac{1}{2\tau}$ because the condition maximizes the phase accumulation calculated by an integration. In addition, since harmonics (odd multiples of f_{ac}) are also observed, the echo envelope oscillates at a frequency $f_{\mathrm{ac}}/2$ for 2τ, where f_{ac} is the frequency of target AC field. Figure 2.5(b) shows an example of Hahn echo spectrum of a single NV center in magnetic field of 2.68 mT. The echo signal modulates strongly at 13.7 kHz,

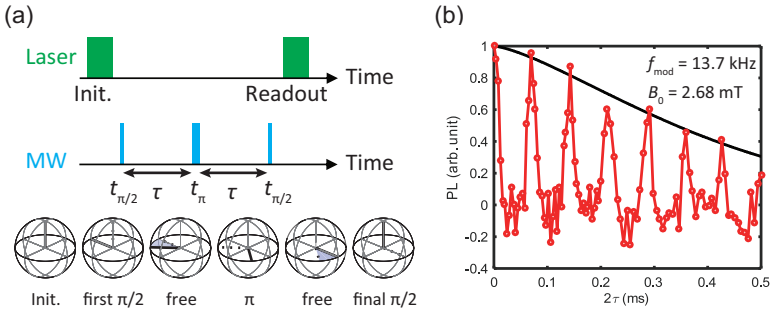

Figure 2.5: (a) Pulse sequence for Hahn echo. Bloch spheres in rotating frame with microwave frequency is shown at the bottom. (b) An example of Hahn echo as sweeping the interpulse delays 2τ. A single NV center in a bulk of pure diamond (natural abundance of ^{13}C 1.1 %) is measured in magnetic field of 2.68 mT. The echo envelope is strongly modulated by surrounding ^{13}C nuclear spins by 13.7 kHz. The solid line is fitting of envelope $\exp[-(2\tau/T_2)^p]$.

which corresponds to the original target frequency of 27.4 kHz $= 2 \times 13.7$ kHz. It is the signal of ^{13}C nuclear spins surrounding a single NV center, whose precession frequency is $f_c = 28.7$ kHz.

This sequence is also applicable to detect the electron spin with precession frequency much faster than $f_{\rm det}$. The detection condition is achieved when resonance frequencies of NV center and the target electron spin is close. The local magnetic field conditions at NV centers are changed by the flipping of target electron spins by the π pulse. When the target electron spins are ensemble, because the ensemble spin state varies measurement cycles, the change of the local field is detected as sensor decoherence. It is called decoherence spectroscopy and its application is shown in Sec. 3.4.

As in Ramsey case, the decay of the envelope occurs due to the fluctuation of environment spins. In most NV measurement, the time scale of the coherence is significantly long compare to the Ramsey case because the noise varying slower than the Hahn echo sequence duration 2τ is canceled out by refocusing effect of middle π pulse. Additionally, we mention that the stretch factor p is parameter of envelope decay shape which depends on the source of decoherence.

By introducing more π pulses periodically between a Ramsey sequence, the coherence time enhances by further filtering of the noise. Since it is periodical pulse application, it still have a certain detection window for coherent signals. It is called dynamical decoupling and is used for practical AC magnetometry and nuclear spin detection (see Chap. 4).

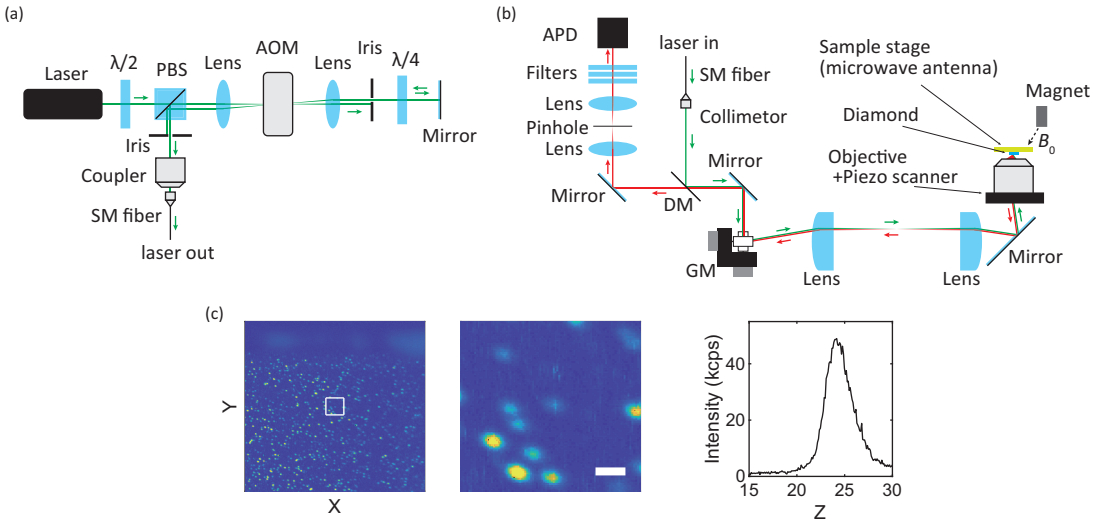

Figure 2.6: Schematic diagram of our optical system (a,b), and typical photoluminescence (PL) images (c). (a) Laser switching optics. (b) Laser scanning confocal microscope. Filters include long path (> 650 nm), short path (< 800 nm), and notch filters (515 nm). PBS: polarizing beamsplitter; AOM: acousto-optic modulator; $\lambda/2$: $\frac{\lambda}{2}$-plate; $\lambda/4$: $\frac{\lambda}{4}$-plate; SM fiber: single mode fiber; DM: dichroic mirror; GM: galvanometric mirror; APD: Avalanche photodiode. (c) PL image taken with the system shown in (a,b). Left panel is PL mapping at the surface of synthetic CVD diamond which contains single NV centers. The size of scanning area is 60×60 μm^2, and the size of the white square is 6×6 μm^2, which is expanded in middle panel. The scalebar in middle panel represents 1 μm. A right panel is PL intensity as sweeping the objective lens height using the piezo scanner. The full width at half maximum is ~ 3 μm.

2.1.5 Confocal microscope

A confocal microscope is an essential tool for resolving single NV centers. Even there are some commercial microscope systems for ODMR measurements, the ODMR setups in research labs are often homemade for the flexibilities needed to enhance the performance.

Figures 2.6(a,b) show our homemade confocal optical system built for the single NV measurement. The system consists of two parts, the laser switching part [Fig. 2.6(a)] and the main confocal part [Fig. 2.6(b)]. We use a green laser at 515 nm for the PL excitation.

For laser switching in the pulse measurement, we utilize an acouto-optic modulator (AOM), which switches the input laser diffraction using reflection index spatial modulation of an optic crystal activated by a piezo transducer. In Fig. 2.6(a), the beam first goes

through a $\frac{\lambda}{2}$-plate and a polarizing beamsplitter to purify the laser linear polarization in the vertical direction. The beam is then focused through an AOM aperture by a lens, and is collimated by another lens after AOM. When AOM is turned off, no beam diffraction occurs, and thus beam goes through and hit an iris that can absorb most of the laser power. On the other hand, when AOM is turned on, the beam is diffracted, and it can go through the iris. After that, it is reflected by a mirror and back to AOM again. Since it goes through $\frac{\lambda}{4}$ twice, before and after the reflection, the laser linear polarization is shifted from vertical to horizontal, and the beam is reflected at the polarization beamsplitter. The beam goes through another iris for further filtering of the non diffracted beam, and it is coupled to a single mode fiber to bring it for a confocal system shown in Fig. 2.6(b).

The benefit of this double path configuration is the high switching contrast. For example, our AOM diffraction contrast is normally 10^3:1, and it is amplified up to 10^6:1, which is sufficient to control NV center. Additionally, the single mode fiber coupling purifies the beam distorted after going through AOM, so it is useful for achieving higher resolution [Fig. 2.6(b)] and higher switching contrast.

In the main part of the confocal system shown in Fig. 2.6(b), the green laser coming from the switching system [Fig. 2.6(a)] goes through a collimator for making the beam parallel at free space. The dichroic mirror, which is a long path filter mirror, reflects the green laser. The reflected beam goes into the laser scanning system.

The laser scanning system consists of a galvanometric mirror, two long focal length (f) lenses, and an objective lens. The distances between galvanometric mirror to first lens, first lens to second lens, and second lens to objective lens, are f, $2f$, and f, respectively. The galvanometric mirror is a pair of mirrors whose angle can be adjusted by motors. The beam traveling direction is controlled by changing the angles of the mirrors. When the beam traveling direction is shifted by θ from the alignment axis of a lens pair between galvanometric mirror and objective lens, the beam angle gets parallel to the alignment axis by the first lens, and the angle information is carried into the path between beam propagation axes relative to the alignment axis. The finite size original beam spot size is distorted by the first lens, but it goes back to the original size by the second lens. The second lens focuses the beam to the back aperture of the objective lens and the incidence angle is exactly same as θ. The laser spot position on the diamond sample surface is two-dimensionally scanned by the angles of the mirrors of the galvanometric mirror.

The precise tuning of the focal plane is possible using the piezo scanner mounting objective lens. Since the translation range (~ 0.1 mm) is much shorter than focal length of the lens, the deviation in the distance between the second and objective lenses is negligible.

When the laser spot hits a NV center, red single photons come out from the objective lens. The red photons go through the scanning system and a dichroic mirror. The red photons from the focal position are parallel to the propagation axis, however it is possible to include red photons from off focal positions, which are not parallel.

The unwanted photons from off focal position are spatially filtered by a pinhole. Only the parallel photons can go through the pinhole at focal position while others can't. The output photons go through more optical filters to increase the contrast of the NV center fluorescence by removing unwanted fluorescence from other defects such as NV^0. The filters also removes strong leakage of the green laser from the dichroic mirror. The purified red photons are detected by an avalanche photodiode, which has a high quantum efficiency with a low dark count.

In addition, for applying microwaves, diamond is attached to a sample stage that can serve as a microwave antenna. In most cases, a coplaner waveguide is used as a sample stage, and a narrow (30 μm) copper wire soldered on the waveguide is placed across the diamond surface. The external bias field is applied by a permanent magnet, and the dipole magnetic field of the magnet at the sensor position is carefully controlled by the magnet position adjusted with the three-axes motorized stage.

Figure 2.6(c) shows a PL scan image of a diamond surface taken with the setup. The diamond sample surface is a 5 nm CVD nitrogen delta doping layer that contains single NV centers. The left panel shows a large area (60×60 μm^2) PL image taken as sweeping galvanometric mirror angles, and the middle panel is a magnified image of the center small region (6×6 μm^2). As seen in the panels, many bright spots are successfully resolved except for the top of the left panel, which is covered by a copper wire for the microwave irradiation. A scale bar shown in the middle panel is 1 μm so that the nanoscale resolution is obtained. The right panel shows vertically scan data of the center bright spot shown in the middle panel. This confirms that the spatial filtering with the pinhole works from the sharp peak found at Z = 24 μm.

2.1.6 Microwave system

We then show the microwave pulse generation system and its synchronization with the optical system. Figure 2.7 shows a schematic of the connection of the present system.

The microwave signal is generated with IQ modulation of a vector signal generator (VSG) using an arbitrary waveform generator (AWG). The pulse shape, frequency, and phase of the microwave signal are controllable with appropriate IQ signals uploaded from PC. The microwave signal is amplified to $\sim$ 1 watt, and injected to a microwave antenna after going through a circulator, which is used for mitigating reflected microwaves going

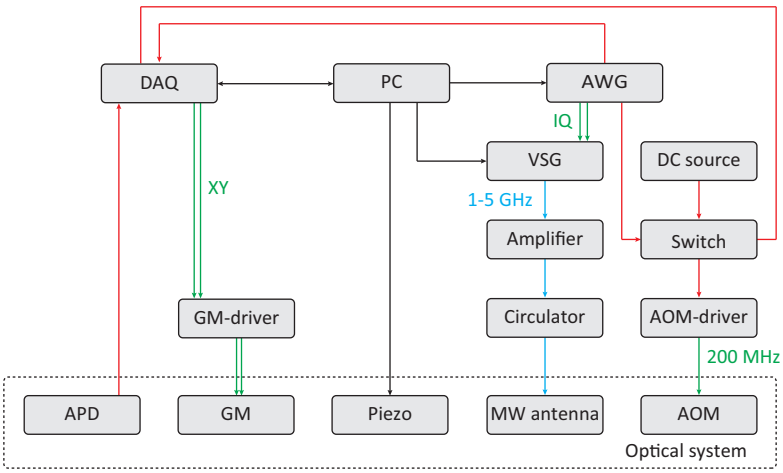

Figure 2.7: A schematic of a microwave system. Red lines represent TTL digital signal lines. Green lines represent low or radio- frequency analog signal lines. Blue lines represent microwave analog lines. Black lines represent digital USB connections. The dashed squares denote the components included in the optical system shown in Fig. 2.6. AWG: arbitrary waveform generator; VSG: vector signal generator; DAQ: data acquisition instruments, including counter, digital output, and analog output; MW antenna: microwave antenna. See definition of other omitted names in caption of Fig 2.6.

back to the amplifier. For large frequency shift of more than 100 MHz, we normally change the frequency of VSG directly from PC.

AWG controls AOM for synchronizing the microwave sequence with laser pulses. For PL mapping, only continuous excitation is required. The AOM is driven by 200 MHz signals generated from its driver, which can be switched by TTL signal. The driver is connected with AWG and a DC source with a switch controlled by the digital signal coming from DAQ for supporting both the pulse measurement and PL imaging.

The galvanometric mirror is connected to its driver, which linearly encodes the input analog signal to the mirror angle, and the analog signal for controlling is generated from DAQ. For PL mapping, photon signal, TTL signal from APD, is counted by DAQ, and it is sampled when the position is shifted to map the intensity for each data pixel. The piezo scanner for the objective position control is made by PC, and it is not synchronized with DAQ. To obtain the focus position, the photon counting for each piezo stage position is sampled by controlling DAQ and piezo scanner individually.

For pulsed measurements, DAQ should be synchronized with AWG for keeping photon counting timetag during the microwave sequence. This is done by TTL signal from AWG to DAQ. When AWG starts generating the IQ signal, the TTL triggered signal for DAQ is simultaneously generated. The photon timing is stored by sampling of 100 MHz counting at photon arrival time, and the 100 MHz photon counter is launched by the TTL trigger signal. For example, when three photons arrive at 100 ns, 1 μs, and 10 μs after the sequence generation, we obtain three counting data as 10, 100, and 1000 (the photon timing is tagged with 10 ns resolution).

After photon counting is transferred from DAQ to PC, we extract the number of photons arrived. We integrate the number of photons as a sampling data during the gating time. For a single NV measurement, we typically integrate the photon number for 500 ns from the readout pulse application.

We measure many cycles of the microwave sequence to obtain large number of photon counts (in most case $> 10^4$) to get a high signal to noise ratio of the average photon count per readout reflecting NV's electron spin state. The integrated photon number reflects transition probability of the NV spin state. We normalize the integrated photon data to obtain the transition probability using the reference photon intensity of $m_S = 0$ and $m_S = \pm 1$ states.

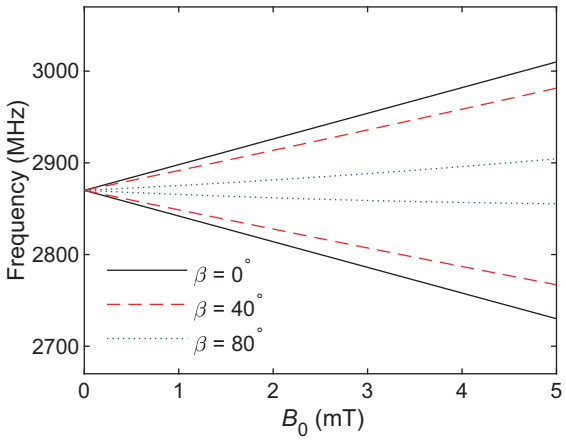

Figure 2.8: Magnetic field dependence of resonance frequencies of a single NV center. β represents a tilt angle between NV-axis and magnetic field.

2.1.7 Resonance spectrum of NV ensembles and magnetic field calibration

To explain ODMR spectrum of NV ensemble, which is a group of many individual single NV centers, the resonance frequencies of a single NV center are first explained based on Eq. (2.1). Figure 2.8 shows magnetic field dependence of resonance frequencies calculated using Eq. (2.1). β represents the tilt angle between NV axis and the magnetic field. When $\beta = 0$, magnetic field is parallel to the NV axis, and the resonance frequencies shift linearly with magnetic field strength. On the other hand, when $\beta = 40°$ and $80°$, the resonance frequencies change nonlinearly with the magnetic field strength. The separation of the frequencies decreases as β increases. The magnetic field strength and tilt angle from a NV axis can be obtained from the resonance frequencies (see Appendix A).

NV ensemble includes NV centers with all four possible symmetry axes, [111], $[\bar{1}\bar{1}1]$, $[1\bar{1}\bar{1}]$, and $[\bar{1}1\bar{1}]$. The tilt angles between respective NV axes and the magnetic field are all different except for the specific magnetic field direction. Therefore eight resonance dips can be found in the ODMR spectrum, and the patterns of eight resonance frequencies depends on magnetic field vector. Figure 2.9 shows ODMR spectrum of NV ensemble. The resonance frequencies depend on the position of a permanent magnet used for magnetic field application. The magnetic field vector at each magnet position can be obtained as shown in the right schematic of Fig. 2.9 by calculating magnetic field vector consistent with B_0 and β for each NV axis. It is also possible to fit the magnetic field vector by minimizing the difference of resonance frequencies between measurement and calculation

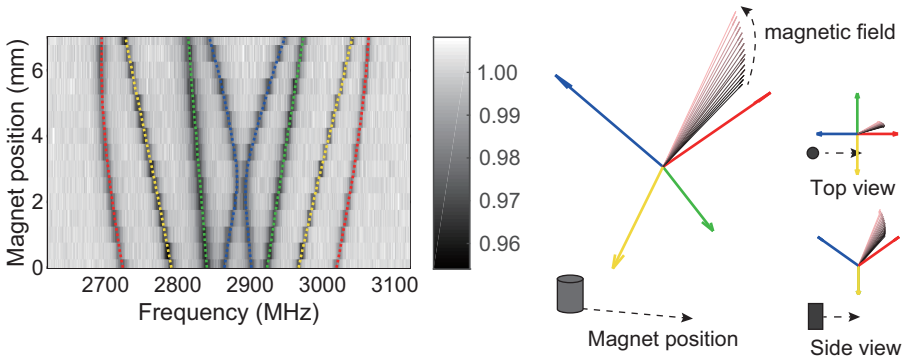

Figure 2.9: (Left panel) ODMR spectrum of NV ensemble as adjusting the position of a permanent magnet. (Right schematic) Obtained magnetic field direction relative to NV axes (red: [111], green: $[\bar{1}1\bar{1}]$, blue: $[\bar{1}\bar{1}1]$, yellow: $[1\bar{1}\bar{1}]$). Dashed arrows represent the direction of movement of the permanent magnet ($\sim [110]$) and the direction of change of the magnetic field vector.

using Eq. (2.1) for each NV axis.

2.2 Development of large-area microwave antenna for optically detected magnetic resonance

We report on a microwave planar ring antenna specifically designed for optically detected magnetic resonance (ODMR) of nitrogen-vacancy (NV) centers in diamond. It has the resonance frequency at around 2.87 GHz with the bandwidth of 400 MHz, ensuring that ODMR can be observed under external magnetic fields up to 100 G without the need of adjustment of the resonance frequency. It is also spatially uniform within the 1-mm-diameter center hole, enabling the magnetic-field imaging in the wide spatial range. These features facilitate the experiments on quantum sensing and imaging using NV centers at room temperature.

This Sec. 2.2 is reproduced from *K. Sasaki, Y. Monnai, S. Saijo, R. Fujita, H. Watanabe, J. Ishi-Hayase, K. M. Itoh and E. Abe, Broadband, large-area microwave antenna for optically detected magnetic resonance of nitrogen-vacancy centers in diamond. Review of Scientific Instruments Vol. 87, 053904 (2016)*, with the permission of AIP Publishing.

2.2.1 Introduction

Nitrogen-vacancy (NV) center in diamond is an atomic defect consisting of a substitutional nitrogen and a vacancy adjacent to it. Among a few charge states NV centers can take, the negatively charged NV^- state possesses optical and magnetic properties favorable to quantum technology applications [103, 104]. The electronic spin of a single NV center (hereafter NV center specifically refers to the NV^- state) can be manipulated by microwave at around 2.87 GHz, and can be initialized and read out optically owing to the state-dependent fluorescence [105]. Its long coherence time at room temperature makes it a leading candidate for a ultra-sensitive, nanoscale magnetometer [20, 21, 24–26, 35]. In addition, the both long coherence time and magnetometry have also been realized in ensemble NVs under ambient conditions [33, 38, 106, 107]. Consequently, NV-based sensing and imaging of magnetic fields, as well as other physical quantities such as temperatures and electric fields, have become an active area of research and are expected to find practical applications not only in physics but also in biology, medical science, planetary science, and so forth [34, 40, 95, 108–112]. In optically detected magnetic resonance (ODMR) experiments of NV centers, a thin straight copper wire or a millimeter-sized loop coil is commonly used to generate an oscillating magnetic field $\boldsymbol{B}_{\mathrm{ac}}$ [13, 113]. For sensing with ensemble NVs, in which the sensitivity is enhanced by the square-root of the number of spins at the expense of nanoscale resolution, the uniformity of $\boldsymbol{B}_{\mathrm{ac}}$ is particularly important. Even in sensing with single NVs, the starting point is to search a diamond substrate for single NVs by confocal microscopy and ODMR. $B_{\mathrm{ac}} = (|\boldsymbol{B}_{\mathrm{ac}}|)$ can be made strong in the vicinity of a wire, but decreases rapidly as departing from it. On the other hand, B_{ac} generated by a loop coil is more uniform, but tends to be much weaker than that by the wire. Moreover, both structures are placed in contact with a diamond surface, nearby which an objective lens and/or a specimen to be sensed, varying from inorganic materials to living cells, are necessarily present. One cannot observe, for instance, the region beneath the wire, as it hinders the light propagation. Therefore, it is preferable to leave the surface open as much as possible. A few microwave circuits for ODMR of NV centers that are placed beneath diamond samples have been devised. Bayat *et al.* developed a double split-ring resonator which achieves spatially uniform B_{ac} and efficient coupling to NV centers [114]. While the resonator frequency is shown to be tunable within 400 MHz around 2.87 GHz by placing a copper tape near the structure, its moderate quality factor ($Q \sim 70$) allows only one resonance (typically < 10 MHz linewidth) within the bandwidth (40 MHz), making it difficult to simultaneously observe multiple resonances separated by 10-100 MHz under weak external magnetic fields. Mrózek *et al.* designed a microwave circuit operating between 2.7 GHz and 3.1 GHz with a notable capability of generating ar-

bitrary microwave polarizations [115]. A drawback is that the distributions of microwave strength and polarization depend largely on the positions, and careful calibrations may be necessary. In this Sec. 2.2, we aim to design and characterize a microwave planar ring antenna that addresses above-mentioned limitations. The design targets of our antenna are as follows: (i) It is placed beneath a diamond sample, thereby does not interfere with the objective lens or the specimen. (ii) It generates B_{ac} spatially uniform within an area of about 1 mm^2, which covers large parts of typical diamond samples. (iii) It has a resonance frequency at around 2.87 GHz and a bandwidth of a few 100 MHz ($Q < 10$) so that multiple resonances can be addressed.

2.2.2 Design and S-parameter

Figure 2.10(a) shows a photograph of a fabricated microwave antenna we have developed. The design parameters are summarized in Fig. 2.10(b). Our ring resonator is regarded as a single-loop coil surrounding a circular hole, inside of which resonant magnetic fields are concentrated [114,116,117]. To help intuitive understanding of the design, we model the structure as a simple series LCR circuit. The inductance L_0 arises from the circular hole: $L_0 \propto r$. The capacitance C_0 is formed by the gap: $C_0 \propto (R + s - r)/g$. The constriction connecting the upper and lower half-circles will contribute to the resistance: $R_0 \propto (R - s - r)^{-1}$. Then, the resonance frequency $2\pi f_0 = (L_0 C_0)^{-1/2}$ and the quality factor $Q_0 = 2\pi f_0 L_0 / R_0$ are proportional to $\sqrt{g/\{r(R+s-r)\}}$ and $(R - s - r)\sqrt{gr/(R+s-r)}$, respectively. These expressions, although very naive, indicate that small g and large s are desirable to achieve low Q, which is our design target (iii). Practically, the minimum achievable g is limited by our manufacturing accuracy of 0.1 mm. In relation to our design targets (i) and (ii), the primary consideration is the sample size. Typical diamond substrates are 1–5 mm on a side with thickness t_{d} of around 0.5 mm. As the NV centers existing near the top surface are used for sensing, we are mainly concerned with the distribution of B_{ac} about 0.5 mm above the antenna surface. We find that r comparable with t_{d} is advantageous to deliver spatially uniform and strong B_{ac} to the diamond surface. We thus limit r to be around 0.5 mm and adjust the remaining design parameters R and s to tune f_0 and Q_0 to the desired values, using three-dimensional electromagnetic simulation software CST MICROWAVE STUDIO®. In the simulation, we set the width and thickness of diamond as $w_{\mathrm{d}} = 2.2$ mm and $t_{\mathrm{d}} = 0.51$ mm, respectively, to coincide with the actual size of the diamond sample used for S-parameter and ODMR measurements below. However, the electromagnetic property of our antenna is found to be insensitive to the sizes of diamond samples.

Simulated B_{ac} at the diamond surface is shown in the left-hand side of Fig. 2.11(a),

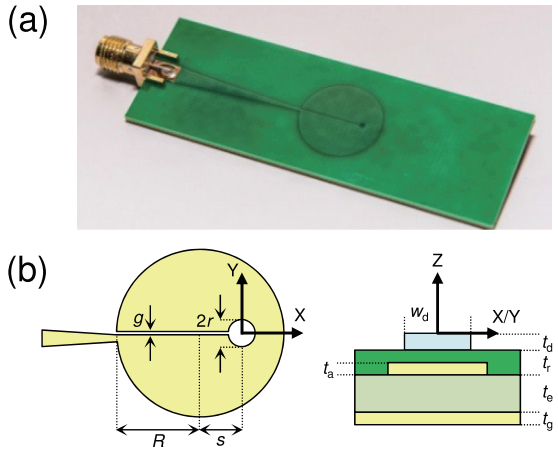

Figure 2.10: (a) A photograph of a microwave antenna. (b) Design parameters and the definition of the XYZ coordinate. R (= 7.0 mm): ring radius, r (= 0.5 mm): hole radius, s (= 3.9 mm): distance between the ring and hole centers, g (= 0.1 mm): gap, w_{d} (= 2.2 mm): width of diamond ($\epsilon_{\mathrm{r}} = 5.68$, $\sigma = 0$ S/m), t_{d} (= 0.51 mm): thickness of diamond, t_{r} (= 0.03 mm): thickness of resist (as a solder mask, $\epsilon_{\mathrm{r}} = 4.3$, $\tan\delta = 0.025$), t_{a} (= 0.018 mm): thickness of metal conductor for antenna (copper, $\sigma = 5.8 \times 10^7$ S/m). t_{e} (= 1.6 mm): thickness of epoxy glass (FR4, $\epsilon_{\mathrm{r}} = 4.3$, $\tan\delta = 0.03$). t_{g} (= 0 mm in simulation, 0.018 mm in fabricated devices): thickness of metal conductor for ground plane. Here, ϵ_{r} is the relative permittivity, σ is the conductivity, and $\tan\delta$ is the loss tangent. Simulation and actual values are the same except for t_{g}. To impedance-match with instrumental 50 Ω, the width of the 23-mm-long feed line is consecutively varied from 3.3 mm (SMA connector side) to 0.54 mm (ring edge). (This figure is reproduced from Ref. [91].)

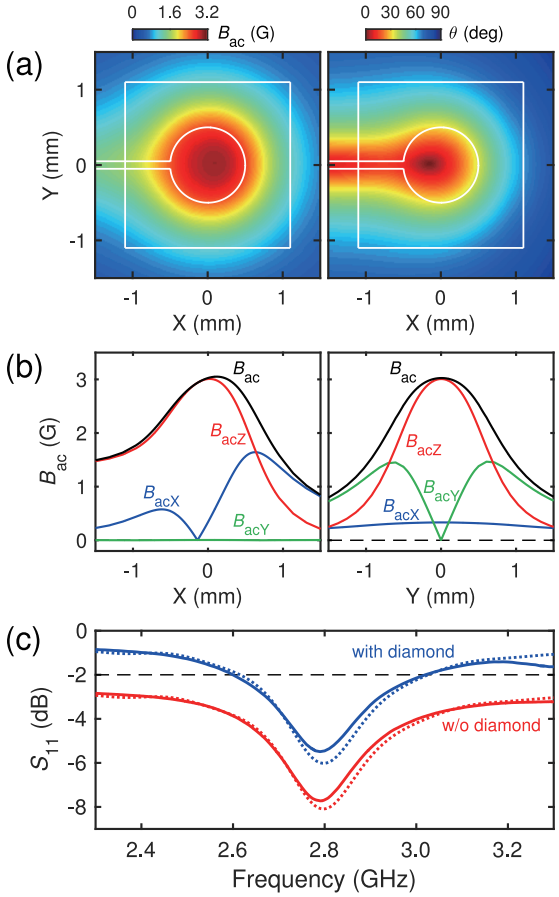

Figure 2.11: (a) Simulated B_{ac} and θ at the diamond surface (Z = 0 mm) with f_{mw} = 2.87 GHz and P_{mw} = 1 W. The solid (white) lines outline the diamond sample and the hole and gap structures of the antenna. (b) Cross sections of (a) along the X (left) and Y (right) axes. The components of B_{ac} are also shown. (c) Measured (solid lines) and simulated (dotted lines) S_{11} with (blue) and without (red) diamond on top of the antenna. The data without diamond are shifted downward by 2 dB for clarity. (This figure is reproduced from Ref. [91].)

and its cross sections along the X and Y axes are in Fig. 2.11(b). The microwave frequency $f_{\rm mw}$ is 2.87 GHz and the microwave power $P_{\rm mw}$ is 1 W. As expected, $B_{\rm ac}$ is concentrated inside of the hole and the main component of $B_{\rm ac}$ is in the Z direction ($B_{\rm acZ} \geq 0$). To evaluate the directional uniformity, we calculate the zenith angle θ, i.e., the tilt angle from the Z axis, as

$$\theta \;=\; \arccos\left(\frac{B_{\rm acZ}}{B_{\rm ac}}\right) \; (0^\circ \leq \theta \leq 90^\circ), \tag{2.14}$$

which is shown in the right-hand side of Fig. 2.11(a). The X and Y components are very small ($\theta \sim 0^\circ$) in the center region and increase towards the peripheral of the hole ($\theta \sim 30^\circ$). Thus, as long as we restrict the scanning range inside of the hole, we expect spatially and directionally uniform $B_{\rm ac}$. Figure 2.11(c) shows measured (using a vector network analyzer) and simulated reflection coefficients S_{11} with and without diamond on top of the antenna. The experimental resonance frequency is almost unaffected (2790 MHz) by the presence of diamond. We obtain the bandwidth of 437 MHz ($Q \sim 6.4$) and 395 MHz ($Q \sim 7$) with and without diamond, respectively. These features are well reproduced by simulation.

We note that in this simulation the presence of double-sided tapes [Fig. 2.12(a)] is not considered. Also, in simulation the antenna metal is embedded in the resist layer, and the thickness of the resist changes depending on the presence or absence of the metal [Fig. 2.10(b)]. In actual fabricated antennas, the resist covers the surfaces of metal and epoxy glass with uniform thickness. Figure 2.11(c) confirms these differences have minor, if not negligible, effects on comparison between simulation and measurement.

2.2.3 Sample and experimental setup

The $(w_{\rm d}^2 \times t_{\rm d})$-sized diamond sample is pictured in Fig. 2.12(a). Through the transparent sample, the hole and gap structures of the antenna as well as double-sided tapes to immobilize the sample are visible. Microwave plasma-assisted chemical vapor deposition is used to grow a 100-nm-thick N-doped diamond film on a type $\mathrm{II_a}$ (001) substrate. A portion of doped N forms NV centers [48, 118, 119]. The NV density is estimated to be of the order of 10^{15} cm^{-3}. The spin Hamiltonian of the NV ground state is given, in the frequency unit, as

$$\hat{H}^{(i)} \;=\; D(\hat{S}_z^{(i)})^2 + \gamma_{\rm e}\boldsymbol{B}_0 \cdot \boldsymbol{S}^{(i)}. \tag{2.15}$$

Here, $D = 2.87$ GHz is the zero-field splitting, $\gamma_{\rm e} = 2.8$ MHz/G is the electron magnetic moment, B_0 is the external magnetic field felt by the NV centers, and $\hat{\boldsymbol{S}}^{(i)}$ is the $S = 1$ spin operator with the quantization (z) axis taken as the ith NV axis. The NV axis is

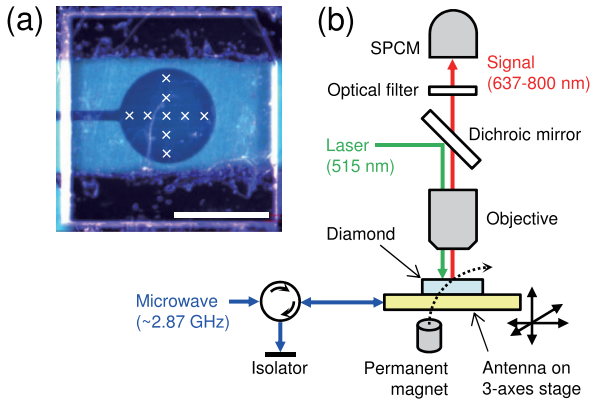

Figure 2.12: (a) An optical microscope image of the diamond sample mounted on the antenna. The scale bar is 1 mm. The cross marks (×) indicate the positions where ODMR measurements in Sec. 2.2.4 are conducted. Their XY coordinates (in millimeter) are (0,0), (0,±0.2), (0,±0.4), (±0.2,0), and (±0.4,0). (b) Schematic of experimental setup. SPCM: single photon counting module. (This figure is reproduced from Ref. [91].)

the vector connecting N and V and is parallel to one of the four ⟨111⟩ crystallographic axes ($i = 1, 2, 3, 4$). In ODMR of ensemble NVs, the maximum of eight resonances, corresponding to the four possible NV axes and the two allowed $|\Delta m_S| = 1$ transitions, is observed. Key elements of our experimental setup are shown in Fig. 2.12(b). A 515-nm green laser light non-resonantly excites the NV electrons, and red signal photons emitted from the NV centers are counted with a single photon counting module. The duration and interval of laser illumination are controlled by an acousto-optic modulator. For continuous wave (CW) and pulsed magnetic resonance of the NV electronic spins, a microwave signal generator and an amplifier are connected to the antenna. A permanent magnet is used to split the $m_S = \pm 1$ states. In our measurements, the positions of the objective lens and the permanent magnet are fixed, and the diamond sample and the antenna move in the XYZ directions with 3-axes piezo- and translation stages. Therefore, the orientation and strength of the external magnetic field do not change at the focal point. This means that even when NV centers in different positions are measured, they feel the same $\boldsymbol{B}_0$.

2.2.4 Comparison with other methods

The CW ODMR spectrum taken at the hole center (0,0) is shown in the right-hand side of Fig. 2.13. In the CW mode, the laser illumination and the photon counting are

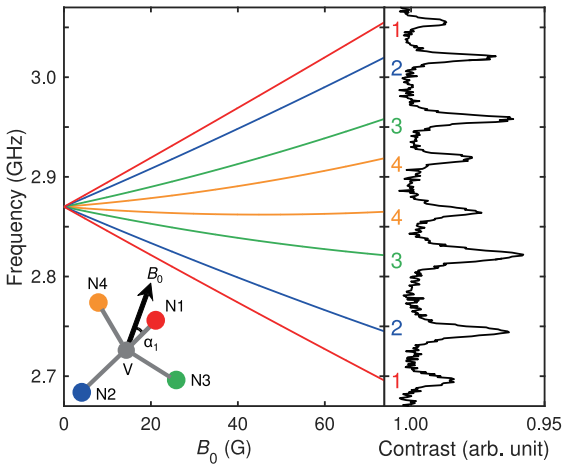

Figure 2.13: CW ODMR spectrum taken at the hole center (0,0) (right) and calculated B_0-dependence of the transition frequencies at $\alpha_1 = 29°$, $\alpha_2 = 132°$, $\alpha_3 = 109°$, and $\alpha_4 = 83°$. At $B_0 = 74$ G, the eight resonances are reproduced simultaneously. (This figure is reproduced from Ref. [91].)

executed continuously, during which the microwave frequency is swept. The fluorescence decreases at the resonance, giving a series of dips. The contrast is given as the ratio between the data with the microwave on and off in order to cancel out the background. The eight dips characteristic of ensemble NVs are clearly observed. The Zeeman term of Eq. (2.15) is written as $\gamma_e B_0(\sin\alpha_i \hat{S}_x^{(i)} + \cos\alpha_i \hat{S}_z^{(i)})$, where α_i is defined as the angle between $\boldsymbol{B}_0$ and the ith NV axis. By numerically solving Eq. (2.15), we determine B_0 and α_i as $B_0 = 74$ G with $\alpha_1 = 29°$, $\alpha_2 = 132°$, $\alpha_3 = 109°$, and $\alpha_4 = 83°$ that reproduce the eight resonances simultaneously. As α_i is made closer to 90°, the off-diagonal term with $\hat{S}_x^{(i)}$ becomes non-negligible and the nonlinearity in the evolution of transition frequencies is more pronounced. The observations here demonstrate that under the external magnetic field up to 100 G or so, which is a typical condition for NV-based sensing and imaging experiments [36,113], our antenna does not require an adjustment of its resonance frequency by external perturbations (such as placing a copper tape as in the case of Ref. [114]).

Next, we carry out pulsed ODMR to observe Rabi oscillations and examine the oscillating magnetic field generated by the antenna. After initialization into the $m_S = 0$ state by the laser illumination for 5 μs, microwave is burst for a short time. The spin state is read out by the second laser illumination. As the burst time t is varied, the contrast oscillates reflecting the occupation of the $m_S = 0$ state. Figure 2.14(a) shows an example of measured Rabi oscillations. The data are fitted by the functional form

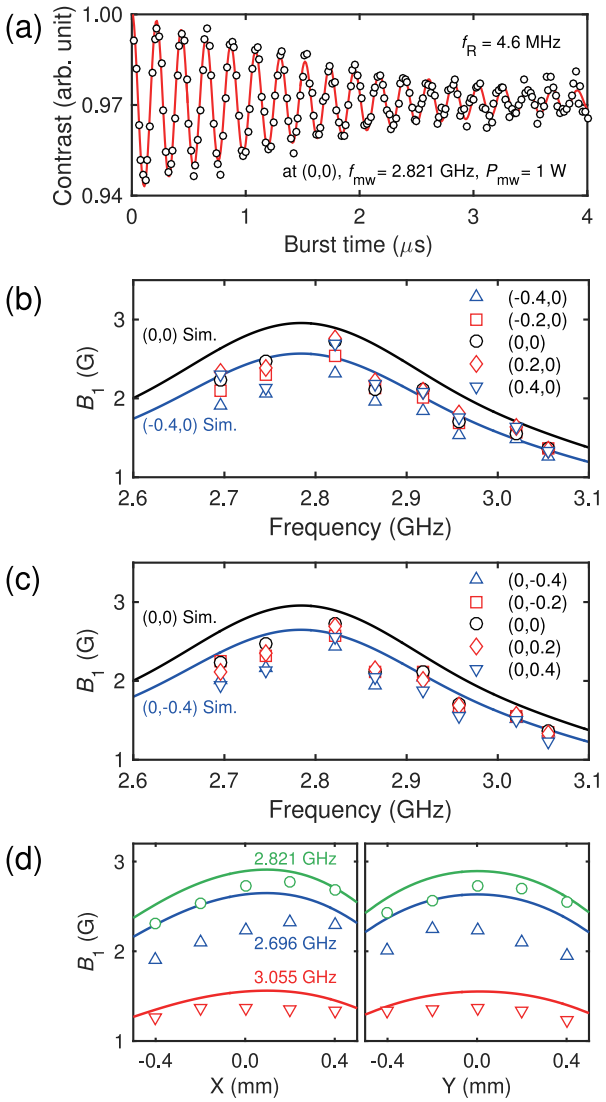

Figure 2.14: (a) An example of Rabi oscillations. The solid line is the fit. ((b),(c)) Plots of B_1 at $P_{\mathrm{mw}} = 1$ W for five positions along the X (b) and Y (c) axes. The solid lines are simulation results at (0,0), (0,−0.4), and (−0.4,0) as indicated. (d) Experimental and simulated (solid lines) spatial distributions of B_1 along the X (left) and Y (right) axes at three frequencies. (This figure is reproduced from Ref. [91].)

$A\exp(-t/\tau_{\mathrm{R}})\cos(2\pi f_{\mathrm{R}}t) + B$, where A is the amplitude, B is the offset, τ_{R} is the decay timescale of the Rabi oscillation, and f_{R} is the Rabi frequency.

We define $\boldsymbol{B}_1$ as $\boldsymbol{B}_{\mathrm{ac}}$ generated at the focal point (i.e., the measurement position). At given P_{mw}, f_{R} and $\boldsymbol{B}_1$ are related by

$$f_{\mathrm{R}} = \frac{\gamma_{\mathrm{e}} B_1 \sin\beta_i}{\sqrt{2}}, \tag{2.16}$$

where β_i is the angle between $\boldsymbol{B}_1$ and the ith NV axis. The components of $\boldsymbol{B}_1$ perpendicular to the NV axis rotate the NV electronic spin. The factor $1/\sqrt{2}$ is due to the rotating wave approximation in the $S = 1$ spin system [18,97]. Through the CW ODMR measurements, we already know the NV axes responsible for the respective resonances [Fig. 2.13], and the simulation results give the orientation of $\boldsymbol{B}_1$ [Fig. 2.11(a)]. They together give β_i, allowing us to convert experimental f_{R} into B_1. Figures 2.14(b) and 2.14(c) plot in total 72 values of B_1 obtained at nine positions [Fig. 2.12(a)] and eight frequencies [Fig. 2.13], covering wide spatial and frequencies ranges. There, B_1 deduced solely from simulation are also shown for (0,0) and (0,-0.4) or (-0.4,0). Other simulated B_1 lines lie between these lines and are not shown. In this simulation, the presence of the double-sided tapes, the thickness of which is 70 μm, are taken into account. This results in a reduction of B_1 compared with Fig. 2.11. Spatial distributions of B_1 along the X and Y axes for three representative frequencies are also shown in Fig. 2.14(d). Overall, the experiments and simulation show similar behaviors with the experimental values slightly smaller than the simulated values. Based on these results, we conclude that our antenna achieves high spatial uniformity and high bandwidth at the same time. As a remark, the fastest f_{R} achieved in our current setup is 10 MHz, which is limited by the saturation power of the microwave amplifier we use. In this condition, we have been able to conduct multi-pulse experiments (dynamical decoupling with hundreds of pulses) without any heating problems. The constraint set by the antenna itself is its bandwidth of 400 MHz, with which the shortest pulse length of 2.5 ns should in principle be possible.

Finally, we make a brief comparison between different methods for applying oscillating magnetic fields to diamond. We simulate coil- and wire-based microwave setups as modeled in Fig. 2.15(a). Figure 2.15(b) shows the distribution of B_{ac} along the Y and Z axes. In all models, the origin of the coordinate is set at the center of the diamond surface. As mentioned in Sec. 2.2.1, B_{ac} is strong near the wire, but weakens as the inverse of the distance from the wire (Ampères law). The coil produces more or less uniform B_{ac} inside of the loop, but the strength is much weaker. The antenna combines both the features. It is also worth noting that B_{ac} of the antenna becomes stronger inside of the diamond. This is advantageous when NV centers deep inside the substrate are investigated, which is important for materials characterization as well as for quantum information processing.

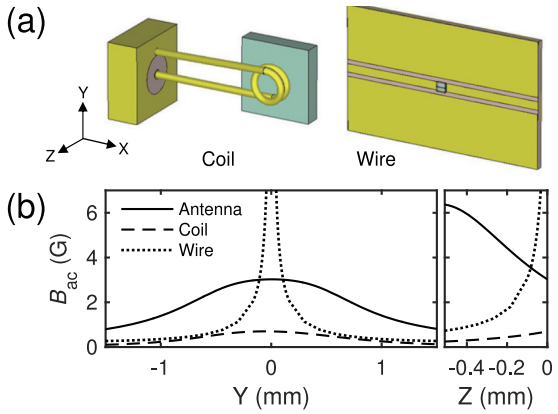

Figure 2.15: Simulation and comparison of different methods for applying oscillating magnetic fields. (a) CAD designs of coil- and wire-based microwave setups. The plates (in moss green) represent diamond substrates with dimensions $w_{\mathrm{d}}^2 \times t_{\mathrm{d}}$ mm^3. On the left is a 1.5-turn coil with the wire diameter of 220 μm and the loop diameter of 1 mm placed in contact with the diamond substrate. One end of the wire is connected to the inner conductor of a 50 Ω connector, through which microwave is supplied. The other end of the wire is terminated at the grounded outer conductor. On the right is a coplanar waveguide matched to 50 Ω with the width of the center line of 2 mm and the gaps of 1 mm. The center line is removed beneath diamond, and instead a 30-μm-diameter copper wire bridges the two ends of the center line. (b) Distribution of B_{ac} along the Y (left) and Z (right) axes at $f_{\mathrm{mw}} = 2.87$ GHz and $P_{\mathrm{mw}} = 1$ W. (This figure is reproduced from Ref. [91].)

When the NV electronic spins are used as quantum bits, the depth from the substrate may be less critical than in sensing application, and the deep NV centers may be preferred for their stability and longer coherence times.

2.2.5 Conclusion

In conclusion, we have designed and characterized a microwave planar ring antenna suitable for ODMR of NV centers in diamond. It has the resonance frequency at around 2.87 GHz with the bandwidth of 400 MHz, ensuring that ODMR can be observed under external magnetic fields up to 100 G without the need of adjustment of the resonance frequency. It is also spatially uniform within the 1-mm-diameter hole, enabling the magnetic-field imaging in the wide spatial range. For imaging experiments, with a piezoelectric actuators, one can scan a few 100^2 μm^2 areas and with a galvanometric mirror even larger areas can be scanned. NV-based wide-field imaging techniques using a CCD or CMOS camera are also compatible with the antenna [38, 111]. These features will facilitate the experiments on quantum sensing and imaging using NV centers at room temperatures.

Chapter 3

DC sensitivity enhancement and electron spin detection

We perform pulsed optically detected electron spin resonance to measure the DC magnetic field sensitivity and electronic spin coherence time T_2 of an ensemble of near-surface, high-density nitrogen-vacancy centers engineered to have a narrow magnetic resonance linewidth. Combining pulsed spectroscopy with dynamic nuclear polarization, we obtain the photon-shot-noise-limited DC magnetic sensitivity of 35 nT $\mathrm{Hz}^{0.5}$. We find that T_2 is controlled by instantaneous diffusion, enabling decoherence spectroscopy on residual nitrogen impurity spins in the diamond lattice and a quantitative determination of their density. The demonstrated high DC magnetic sensitivity and decoherence spectroscopy are expected to broaden the application range for two-dimensional magnetic imaging.

3.1 Principle of DC magnetometry

One of the most important values in magnetic field sensing technique using NV is magnetic field sensitivity. Magnetic field sensitivity is defined as minimum detectable magnetic field per unit time with photon shot noise. The fluctuation of PL intensity δI is converted to the fluctuation of magnetic field $\delta B_0 = \frac{\delta I}{G_I}$ using the gradient of ODMR spectrum $G_I = \frac{\delta I}{\delta B_0}$ with respect to magnetic field strength B_0.

This Chap. 3 is partially reproduced from K. Sasaki, E. E. Kleinsasser, Z. Y. Zhu, W. D. Li, H. Watanabe, K. M. C. Fu, K. M. Itoh and E. Abe, *Dynamic nuclear polarization enhanced magnetic field sensitivity and decoherence spectroscopy of an ensemble of near-surface nitrogen-vacancy centers in diamond. Applied Physics Letters Vol. 110, 192407 (2017)* and *E. Abe and K. Sasaki, Tutorial: Magnetic resonance with nitrogen-vacancy centers in diamond—microwave engineering, materials science, and magnetometry. Journal of Applied Physics Vol. 123, 161101 (2018)*, with the permission of AIP Publishing.

For continuous wave ODMR, PL contrast C, which is the ratio of PL intensity with and without microwave at resonance, resonance dip linewidth $\delta\nu$ and PL intensity without microwave I_0 are critical parameters for DC field sensitivity. Near the half maximum of the resonance dip, the slope is the largest, and can be shown as $G_I = \frac{I_0 C}{\delta\nu/\gamma_e}$ when linearly approximated. Generally, the photon shot noise δI_0 is given by $\sqrt{I_0}$. The DC sensitivity is thus given by

$$\eta_{\rm sn}^{\rm (cw)} = \frac{h}{g\mu_B}\frac{\delta\nu}{CI_0} \times \sqrt{I_0} = \frac{h}{g\mu_B}\frac{\delta\nu}{C\sqrt{I_0}}. \tag{3.1}$$

where $\frac{h}{g\mu_B} = 36$ μT/MHz is the inverse of the gyromagnetic ratio γ_e of the NV electronic spins. It is evident from Eq. (3.1) that the DC sensitivity can be improved by achieving a narrower linewidth $\delta\nu$, a larger contrast C, and larger photon counts I_0. A larger photon counts are attained by using NV ensembles, for which $\delta\nu$ tends to become wider due to the increased inhomogeneity. For such ensemble case, we redefined I_0 as the PL intensity from the NV centers in a unit area (1 μm^2).

3.2 Ensemble-based magnetometry

Submicron scale, two-dimensional (2D) magnetic imaging has potential applications in biological and physical sciences [23, 120]. The realization of utilizing an ensemble of nitrogen-vacancy (NV) centers in diamond is particularly attractive due to its high magnetic sensitivity at ambient conditions [36–38, 95, 111, 113, 121, 122]. Equation (3.1) suggests that simultaneously achieving a high NV density and a narrow linewidth is desired to improve $\eta_{\rm sn}^{\rm (CW)}$. In addition, the NV sensor must be located as close as possible to a magnetic specimen; it is crucial to have an NV ensemble near the diamond surface [48,123].

Recently, Kleinsasser *et al.* have reported the successful creation of a 100-nm-thick layer of NV ensembles at a diamond surface with a density of 10^{17} cm^3 and a $\delta\nu$ of $\sim$200 kHz [59]. This was achieved by a combination of chemical vapor deposition (CVD) growth of a nitrogen-doped, nuclear-spin-free ^{12}C (99.9 %) diamond film [104] and subsequent helium ion implantation to introduce vacancies into the film. The detailed procedure for the NV formation and the characterization of the NV ensemble by photoluminescence (PL) spectroscopy and CW ODMR are given in Ref. [59].

In this Chap. 3, we show that, by concurrently applying pulsed ODMR and dynamic nuclear polarization (DNP) techniques to the same diamond sample, it is possible to realize an $\eta_{\rm sn}$ of 35 nT Hz$^{-0.5}$. We also examine the coherence properties of the NV ensemble to extract quantitative information on residual paramagnetic impurities in the sample. This is an example of decoherence spectroscopy/imaging, in which magnetic signals are

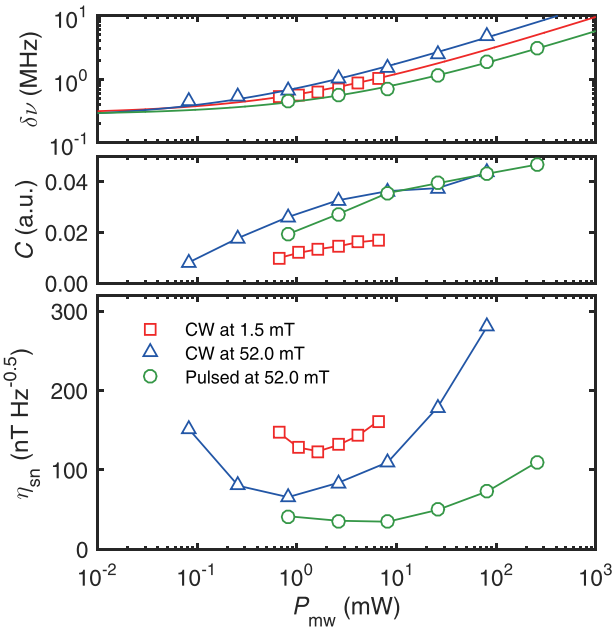

Figure 3.1: $\delta\nu$ (top), C (middle), and $\eta_{\rm sn}$ (bottom) as functions of $P_{\rm mw}$ measured at the input port of the PCB board on which the sample is mounted. The solid lines in the top panel are fits to $\delta\nu_a + bP_{\rm mw}^{0.5}$. The laser power $P_{\rm L}$ was optimized at 100 μW and 1.4 mW for CW and pulsed experiments, respectively. The full-width-at-half-maximum of the laser spot was 520 nm, corresponding to $\sim$ 2100NV centers in the focal volume. The optimized sensitivity $\eta_{\rm sn}^{\rm (pulsed)} = 35$ nT Hz$^{-0.5}$ was obtained at $P_{\rm mw}$ of 8.2 mW, with $\delta\nu = 718$ kHz and $C = 0.036$. (This figure is reproduced from Ref. [92].)

detected via the change in spin coherence time T_2 [41, 42, 56, 124–127]. This method is applicable to identify magnetic signals external to the sample, providing another tool for ensemble-based 2D magnetic field imaging.

3.3 Examination of DC sensitivity

We first recap the main result of Ref. [59] by performing CW ODMR at an external magnetic field B_0 of 1.5 mT. The squares (□) in Fig. 3.1 are the measured $\delta\nu$ (top) and C (middle) together with $\eta_{\rm sn}^{\rm (CW)}$ estimated from Eq. (3.1) (bottom) as a function of the microwave power $P_{\rm mw}$. It demonstrates the minimum sensitivity of 124 nT Hz$^{-0.5}$. The measurement setup in the present work is a home-built confocal microscope combined

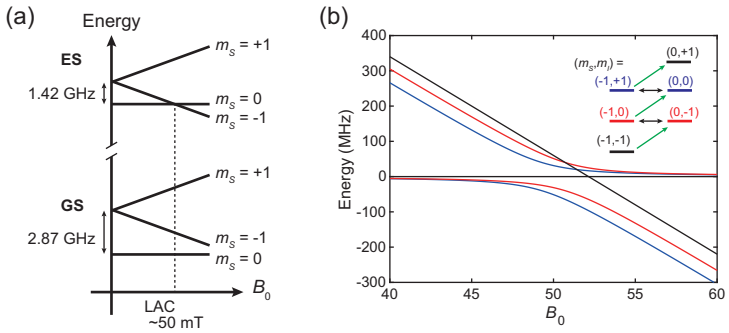

Figure 3.2: (a) A schematic of spin energy levels in magnetic field. $m_S = 0$ and $m_S = -1$ of the excited states come close to each other around $\sim$ 50 mT. (b) Details of the excited energy levels around 50 mT. The spin levels with the same total spin momentum $m_S + m_I$ are mixed and level anticrossings occur. The red solid lines are the spin levels for $m_S + m_I = -1$ and black lines are the spin levels for $m_S + m_I = 0$. The inset shows the mechanism of dynamic nuclear polarization. The electron spin earns a spin momentum by the optical initialization ($m_S = 0 \rightarrow -1$) and the electron spin momentum is transferred into ^{14}N nuclear spin momentum by flip-flop among the mixed spin states. By repeating the process, the sensor spin is initialized into $(m_S, m_I) = (0, +1)$.

with microwave circuitry, enabling CW and pulsed ODMR of single and ensemble NV centers. Throughout this work, B_0 is applied parallel to one of four NV axes, and the $m_S = 0 \leftrightarrow -1$ transition of the NV ensemble aligned to the field is examined, unless otherwise mentioned. The relative improvement in $\eta_{\mathrm{sn}}^{(\mathrm{CW})}$ over the previous result (170 nT $\mathrm{Hz}^{-0.5}$ in Ref. [59]) is attributed to the differences in collection efficiency and measurement location within the sample.

As is evident from Eq. (3.1), the magnetic sensitivity can be improved by optimizing $\delta\nu$, C, and I_0. Indeed, the low-field data in Fig. 3.1 show an interplay between $\delta\nu$ and C; the narrowing of $\delta\nu$ as decreasing P_{mw} is countered by the reduction of C, and $\eta_{\mathrm{sn}}^{(\mathrm{CW})}$ takes its minimum at an intermediate value of $P_{\mathrm{mw}} = 1.64$ mW. We observe $\delta\nu = \delta\nu_a + bP_{\mathrm{mw}}$ with $\delta\nu_a = 250$ kHz [solid line in the top panel of Fig. 3.1]. On the other hand, as demonstrated for a single NV center [128], C and I_0 can be further improved, respectively, by employing the DNP of ^{14}N nuclei ($I = 1$) associated with the NV centers and pulsed ODMR.

It is well-established that the excited state of the NV center experiences a level anti-crossing near 50 mT. Figure 3.2(a) shows a schematic of spin energy levels. The excited state is a spin triplet with $D_{\mathrm{es}} = 1.42$ GHz. This suggests that at $B_0 = D_{\mathrm{es}}/\gamma_{\mathrm{e}} = 51$ mT

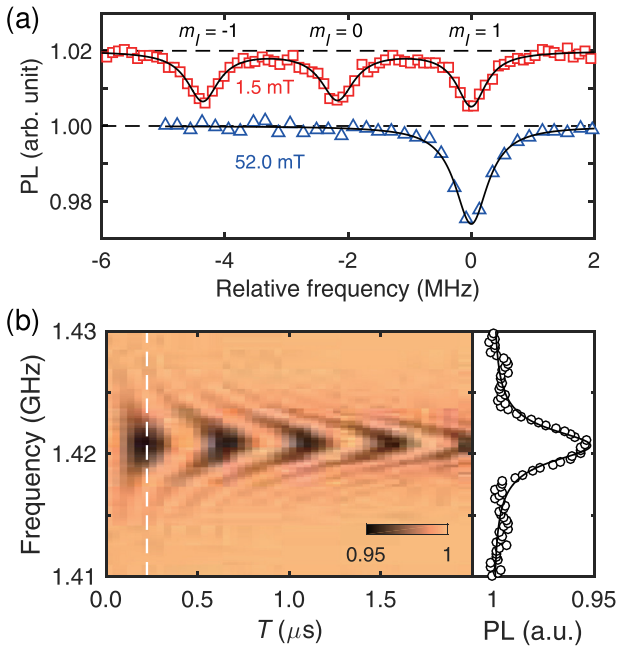

Figure 3.3: (a) CW ODMR spectra at $B_0 = 1.5$ mT and $P_{\rm mw} = 1.64$ mW (shifted upward by 0.02 for clarity) and at $B_0 = 52.0$ mT and $P_{\rm mw} = 0.82$ mW. (b) An example of pulsed spectroscopy. The cross section at $T_{\rm p} = 222$ ns is fitted by a Lorentzian. (This figure is reproduced from Ref. [92].)

the $m_S = 0$ and -1 sublevels of excited state become degenerate. Figure 3.2(b) shows the details of the spin energy levels of excited state. The Zeeman energies of the electronic and nuclear spins are almost equalized, and the hyperfine interaction of the excited state plays a role of mixing the spin state, resulting in the excited state level anticrossing (ESLAC). Using (m_S, m_I) basis for the excited state, the hyperfine interaction induces the flip-flop of the spins: $(m_S, m_I) = (0, -1) \leftrightarrow (-1, 0)$ or $(0, 0) \leftrightarrow (-1, 1)$. Combined with illumination, the role of which is to induce the electronic spin flip from $m_S = -1$ to 0, the system is dynamically driven as $(m_S, m_I) = (-1, 0) \rightarrow (0, 0)$ or $(-1, 1) \rightarrow (0, 1)$. As a result, the ^{14}N nuclei are initialized into the $m_I = 1$ state within a few microsecond laser illumination [129, 130].

Figure 3.3(a) plots CW ODMR spectra taken at 1.5 mT and 52.0 mT, demonstrating clear DNP in the latter. We then repeat the measurements at 52.0 mT [$\triangle$ in Fig. 3.1] to obtain the minimum sensitivity of 66 nT Hz$^{-0.5}$ at $P_{\rm mw} = 0.82$ mW.

In the DNP condition, by pumping the three nuclear spin states into a single state, we should ideally achieve a factor-of-three enhancement of C and thus $\eta_{\rm sn}^{\rm (CW)}$. However,

at a given $P_{\rm mw}$, C under the DNP is typically only twice as deep as that at low fields. Also, the values of C giving the minimum sensitivities are 1.5 % at 1.5 mT and 2.6 % at 52.0 mT [Fig. 3.3(a)], which are reflected in the obtained sensitivities (124 nT Hz$^{-0.5}$ vs. 66 nT Hz$^{-0.5}$). C is determined by a complicated interplay between T_1, T_2^*, and other optical transition probabilities between the NV electronic energy levels (e.g., Eq. (A5) of Ref. [128]). We have examined several physical parameters of our NV ensemble to reproduce the observed C but have not reached a satisfactory explanation. We leave a detailed analysis on this as a future work.

In CW ODMR at a fixed $P_{\rm mw}$, increasing optical excitation power simultaneously increases I_0 and $\delta\nu$ while decreasing C [128]. This leads to an optimal optical power well below the saturation intensity of the NV center. On the other hand, pulsed ODMR temporally separates the optical pumping from the spin manipulation. A higher laser power can be used to significantly increase I_0 while keeping C and $\delta\nu$ intact [128]. An example of pulsed spectroscopy, C as a function of the microwave burst time (T) and the microwave frequency, is shown in Fig. 3.3(b). We denote the experimental sequence as $\tau_{\rm I} - T - \tau_{\rm R}$, where $\tau_{\rm I,R}$ are the durations of green laser excitation for spin initialization and readout. By varying the microwave frequency around $m_I = 1$ resonance, a chevron pattern typical of pulsed spectroscopy is observed. The cross section at the π pulse condition ($T_\pi = 222$ ns) is also shown in Fig. 3.3(b), from which we deduce $\delta\nu$ and C [◯ in Fig. 3.1]. $\eta_{\rm sn}$ for pulsed ODMR is given by [59, 128]

$$\eta_{\rm sn}^{\rm (pulsed)} = \frac{h}{g\mu_B}\frac{\delta\nu}{C}\sqrt{\frac{(\pi\delta\nu)^{-1}+\tau_{\rm I}+\tau_{\rm R}}{\tau_{\rm R} I_0}}, \tag{3.2}$$

and we obtained the minimum sensitivity of 35 nT Hz$^{-0.5}$ for out system.

Through time-resolved fluorescence measurements (data not shown), we optimized $\tau_{\rm I}$ and $\tau_{\rm R}$ as 4.5 μs and 1.5 μs, respectively. These spin initialization and readout times, several times longer than the case of a single NV center (typically about 1 μs and a few 100 ns, respectively), currently limit the achievable $\eta_{\rm sn}^{\rm (pulsed)}$. The long $\tau_{\rm I,R}$ are attributed to the Gaussian profile of the laser spot. Calculations suggest that 58 % of the total fluorescence intensity arise from the region outside of the FWHM of the profile, and the NV ensemble existing in this region is subject to substantially lower laser power, resulting in insufficient initialization for shorter $\tau_{\rm I}$. A long initialization time due to the laser spot profile has also been discussed in Ref. [131].

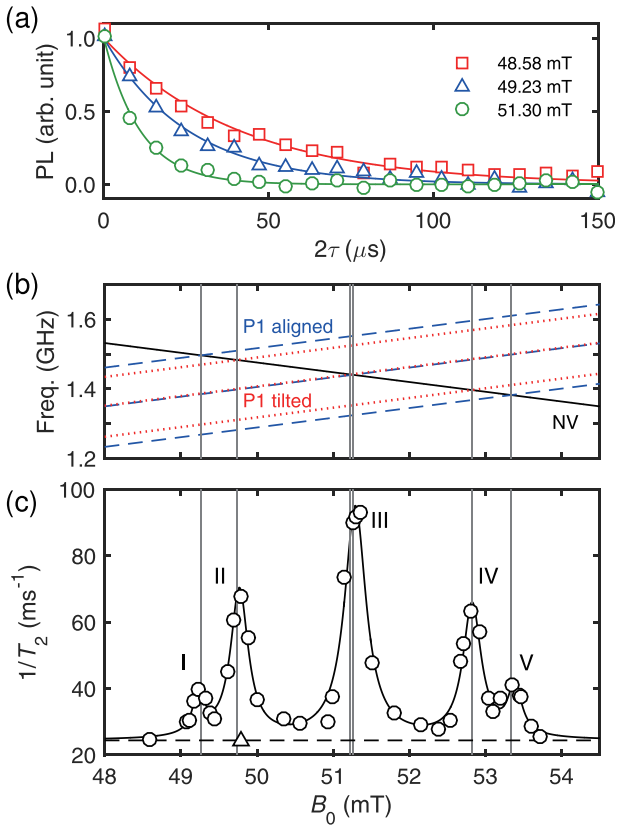

Figure 3.4: (a) Hahn echo decays of the NV ensemble at around $B_0 = 50$ mT. The solid lines are fits by single-exponential decays. (b) The transition frequencies of the NV centers (solid line, $m_S = 0 \leftrightarrow -1$ with $m_I = 1$) and the P1 centers aligned with B_0 (dashed lines) and tilted from B_0 (dotted lines). The unit and scale of the horizontal axis are the same as (c). The vertical lines indicate B_0 at which the SSRs occur. (c) T_2^{-1} as a function of B_0. (This figure is reproduced from Ref. [92].)

Table 3.1: Analysis of Fig. 3.4(c). The peak positions are determined by a quintuple-Lorentzian fit. $(T_{\rm id}^{(i)})^{-1}$ specifies $(T_{\rm id})^{-1}$ at the ith peak after subtraction of $(T_2^{\rm base})^{-1}$. N_i is the impurity density.

Peak	B_0 (mT)	$(T_{\rm id})^{-1}$ (ms^{-1})	N_i (10^{17} cm^{-3})
I	49.23	12.6	0.19
II	49.77	44.8	0.68
III	51.29	70.0	1.05
IV	52.82	40.2	0.61
V	53.38	14.8	0.22

3.4 Decoherence spectroscopy

Having demonstrated the potential of this sample for 2D DC magnetic sensing, we next measure T_2 using a Hahn echo sequence ($\tau_{\rm I} - T_{\pi/2} - \tau - T_\pi - \tau - T_{\pi/2} - \tau_{\rm R}$) and carry out ensemble-based decoherence spectroscopy. Figure 3.4(a) shows three representative Hahn echo decay curves at around 50 mT, all described well by single-exponential decays. We define T_2 by fitting the echo decay curves as $A\exp(-2\tau/T_2)$. A detailed B_0-dependence of the decoherence rate shown in Fig. 3.4(c) reveals a multi-peak structure. As depicted in Fig. 3.4(b), the peak positions [listed in Table 3.1] coincide with the simultaneous spin resonances (SSRs) of the NV and P1 centers: $S = \frac{1}{2}$ substitutional nitrogen impurities with $C_{3\rm v}$ symmetry [16, 132]. In a dipolarly coupled electron spin system, the refocusing pulse flips resonant spins within its bandwidth, instantly changing local dipolar magnetic fields experienced by the individual NV electronic spins: a process known as the instantaneous diffusion (ID). At the SSR, the NV decoherence is accelerated by the increased number of flipped spins. In the case of a homogeneous electron-spin distribution, the ID decay has a form of single-exponential $\exp(-2\tau/T_{\rm id})$ with $T_{\rm id}$ given by [97, 133]

$$\frac{1}{T_{\rm id}} \;=\; DN\sin^2\left(\frac{\beta}{2}\right),\ \text{with}\ D = \frac{\pi\mu_0 g^2\mu_B^2}{9\sqrt{3}\hbar}. \tag{3.3}$$

Here, μ_0 is the vacuum permeability, N is the density of spins rotated, and b is the flip angle of the refocusing pulse. We are thus able to extract the densities of the P1 spins from the increased decoherence rate at the respective peaks.

To do so, we first define the *baseline* decoherence rate $(T_2^{\rm base})^{-1}$ as $T_2^{-1} = 24.4\,{\rm ms}^{-1}$=$(41.1\,\mu{\rm s})^{-1}$ obtained for the $m_S = 0 \leftrightarrow -1$ transition at 49.8 mT driven at 4.2658 GHz [$\triangle$ in Fig. 3.4(c)]. This spin state shares the same decoherence mechanism with the $m_S = 0 \leftrightarrow -1$ one, except for the ID due to the P1 spins. The main contributor to $(T_2^{\rm base})^{-1}$ is the ID among the NV spins, which, for $N_{\rm NV\|B_0} = 0.25 \times 10^{17}$ cm^{-3} (1/4 of the total NV

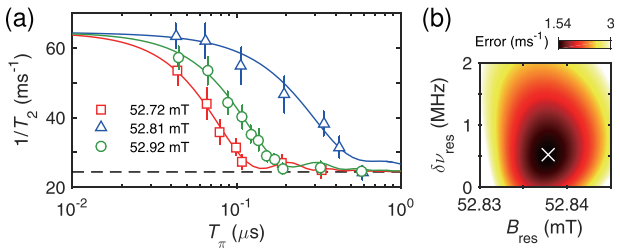

Figure 3.5: (a) T_π-dependence of T_2^{-1} at Peak IV. (b) Fit error as a function of fitting parameters $B_{\rm res}$ and $\delta\nu_{\rm res}$. The cross mark ($\times$) indicates the values giving the best fit. (This figure is reproduced from Ref. [92].)

density [59]), is estimated to be 20.1 ms^{-1}. The rest (4.3 ms^{-1}) should come from (i) the spectral diffusion caused by flip-flops among the P1 spins and (ii) the T_1 relaxation. The lattice ^{13}C nuclei play a negligible role owing to the isotope enrichment of ^{12}C in this sample.

We then calculate the P1-induced $T_{\rm id}$ after subtracting $(T_2^{\rm base})^{-1}$ from the measured T_2^{-1} and the corresponding P1 densities, which are listed in Table 3.1. In Eq. (3.3), $\beta = \pi/\sqrt{2}$ is used, due to the smaller rotation angle for the $S = \frac{1}{2}$ P1 spins relative to the $S = 1$ NV spins [97]. The ratio $(N_{\rm II} + N_{\rm IV})/(N_{\rm I} + N_{\rm V}) = 3.1$ is close to 3: the ratio of the numbers of P1 centers tilted from and aligned with B_0. On the other hand, $(N_{\rm I} + N_{\rm II} + N_{\rm IV} + N_{\rm V})/2 = 0.85 \times 10^{17}$ cm^{-3} is less than $N_{\rm III} = 1.05 \times 10^{17}$ cm^{-3}. The discrepancy may indicate the presence of an additional $S = \frac{1}{2}$ impurity with the density of 2×10^{16} cm^{-3}. We note that, in samples with the P1 density of $\sim 10^{17}$ cm^{-3}, the P1-induced spectral diffusion of the order of a few 100 μs has been observed [107, 134], consistent with our assignment of a-few-ms^{-1} decoherence rate to this mechanism.

From the total P1+NV density of 3.75×10^{17} cm^{-3}, the dipolar-limited linewidth is estimated to be 95 kHz from the second moment [135,136]. This suggests that the present NV linewidth (250 kHz) is still not limited by the dipolar interactions and there is a room for further reducing the NV linewidth while keeping the NV density at 10^{17} cm^{-3}.

Finally, we examine the T_π-dependence of T_2, taking Peak IV as an example. T_π of $\sim$45 ns used in Fig. 3.4(c) is so broadband that the linewidth deduced from the multi-Lorentzian fit (16 MHz) does not necessarily reflect the true width. Figure 3.5(a) demonstrates that, as making T_π longer, T_2^{-1} gradually falls down to $(T_2^{\rm base})^{-1}$, suggesting that less and less P1 spins are flipped. Considering that an effective amount of spins rotated is determined from an overlap between the frequency spectrum of the microwave pulse

$P = (f_{\mathrm{R}}/f_{\mathrm{R,g}})$ and the impurity spin spectrum S, we write T_π-dependent T_2 as

$$\frac{1}{T_2} = \frac{1}{T_2^{\mathrm{base}}} + DN \int PS \sin^2\left(\frac{\beta}{2}\right) df. \tag{3.4}$$

Here, $f_{\mathrm{R}} = (2\sqrt{2}T_\pi)^{-1}$ is the Rabi frequency for $S = \frac{1}{2}$, $f_{\mathrm{R,g}}(f) = \{(f-\delta f)^2 + f_{\mathrm{R}}^2\}$ with $\delta f = 2g\mu_B(B_0 - B_{\mathrm{res}})$ is the generalized Rabi frequency [135], $\beta(f) = 2\pi f_{\mathrm{R,g}} T_\pi$ is the flip angle, and $S(f) = \delta\nu_{\mathrm{res}}/2\pi\{(f-\delta f)^2 + (\delta\nu_{\mathrm{res}}/2)^2\}$ is assumed to be a Lorentzian. Despite the complex form, Eq. (3.4) contains only two fitting parameters (the resonance magnetic field B_{res} and the impurity spin linewidth $\delta\nu_{\mathrm{res}}$) and yet reproduces the experimental data at $(B_{\mathrm{res}}, \delta\nu_{\mathrm{res}}) = (52.838\ \mathrm{mT}, 520\ \mathrm{kHz})$ [solid lines in Fig. 3.5(a)]. The extracted P1 linewidth of 520 kHz is broader than the NV linewidth and the dipolar-limited linewidth, hinting at the presence of additional broadening mechanisms in this sample. On the other hand, Fig. 3.5(b) suggests that, while the error at the best fit is 1.54 ms^{-1}, the 200-kHz-linewidth can be obtained with the error of 1.68 ms^{-1}. Such a small difference in errors can arise, for instance, from the uncertainty in T_1, which is also B_0-dependent around the SSR due to cross relaxation [60, 137–139]. For a more refined estimation of the P1 linewidth, fine-tuning of B_0 to the exact P1 resonance and a detailed measurement of T_1 will be helpful. Nonetheless, the method presented here will be a powerful approach to resolve a spin spectrum when applied to *external* spins.

3.5 Conclusion

In summary, by applying both DNP and pulsed ODMR techniques to a near-surface, narrow-resonance-linewidth NV ensemble, we have shown that a photon-shot-noise-limited magnetic sensitivity of 35 nT $\mathrm{Hz}^{-0.5}$, highly promising for 2D magnetic imaging, is attainable. We have also measured T_2 and deduced quantitative information on residual paramagnetic impurities in the sample. Decoherence spectroscopy as demonstrated here is applicable to detect magnetic signals external to the sample. Although the present work focused on the internal P1 spins for the purpose of demonstrating the power of decoherence spectroscopy, the magnetic field can be readily tuned to avoid the P1 resonances while still maintaining DNP. Such a condition is suitable to concurrently perform highly sensitive DC magnetic imaging and decoherence spectroscopy of external spins [see Appendix. B].

Chapter 4

High resolution AC magnetometry and nuclear spin detection

4.1 AC magnetometry

4.1.1 Introduction

High spatial resolution ac magnetometry with high sensitivity can be a very useful tool. This can be particularly the case in the field of condensed matter physics, chemistry, and materials science, when the spatial resolution and sensitivity reach a single nuclear spin level. It would allow for real space imaging of a single molecule structure by pinpointing each nuclear spin position in the molecule. However, a sensor to do so must be comparable to the size of the atom. Otherwise the required spatial resolution cannot be achieved, and even with such a very small sensing size, it must be sensitive enough to detect a very weak magnetic field from a single nuclear spin, whose strength decays with an inverse of cubic of a distance. Therefore, it is not possible to perform a single nuclear spin imaging with the currently available most sensitive sensors such as superconducting quantum interference devices (SQUID), whose sensing area is much larger than the size of an atom.

A magnetic resonance force microscopy (MRFM) [140] has been developed to achieve spin detection with the nanoscale resolution. It detects an extremely small mechanical motion of a sensitive mechanical cantilever excited by magnetic resonance of the target nuclei under the strong field gradient of a nanometer size magnetic tip in a highly stabilized

This chapter is partially reproduced from *E. Abe and K. Sasaki, Tutorial: Magnetic resonance with nitrogen-vacancy centers in diamond—microwave engineering, materials science, and magnetometry. Journal of Applied Physics Vol. 123, 161101 (2018)*, with the permission of AIP Publishing.

cryogenic ultrahigh vacuum system. Detection of single electron spins of defects in SiO_2 with 25 nm spatial resolution [141] and nanoscale magnetic resonance imaging (MRI) of tabacco mosaic virus particles has been performed with MRFM [142]. However, a single nuclear spin imaging with an atomic scale spatial resolution is yet to be achieved.

The magnetic field sensing using an electron spin of a NV center has emerged as an alternative technique for high spatial resolution magnetometry [20, 21, 26]. NV center is atomically small so that the atomic spatial resolution can be achieved. The NV spin coherence is relatively long (up to 2 ms) compare to other paramagnetic defects in solid state even at ambient conditions leading its high magnetic sensitivity.

It was Maze *et al.* who demonstrated for the first time AC magnetometry using NV centers in nanodiamonds with Hahn echo sequence [24]. By replacing Hahn echo sequence with Carr-Purcell (CP) sequence [143–145], one of a dynamical decoupling sequence, the sensitivity and resolution have been enhanced to Fourier limit of the extended sensor coherence [67–69]. CP sequence has also been used for detection of nuclear spins in diamond [43, 44] or outside of diamond [47]. A high sampling resolution beyond the hardware timing resolution was achieved by appropriate shifting of each pulse timing [146] or shaped pulses [81]. Higher order harmonics, a critical issue for identifying external proton NMR signal, was also mitigated by engineering of pulse timing [70] and novel phase cycling [72, 147]. Moreover, coherence unlimited spectrum resolution was achieved by Fourier transformation of the time series of photon counts obtained with CP sequence [83–85], and it has been used for resolving chemical shift and J coupling of organic molecules with picolitre detection volume at room temperature.

In this Sec. 4.1, state-of-the-art AC magnetometry techniques using CP sequence are introduced and demonstrated. Sec. 4.1.2, shows our experiment setup including a microwave pulse generator and data processing scheme. Sec. 4.1.3 shows the principle of AC magnetometry followed by experiments using an artificial signal. Sec. 4.1.4 shows the principle of coherence unlimited resolution sensing followed by experimental demonstration of achieving 304 μHz spectrum resolution.

4.1.2 Experimental details

Experimental configuration

We use ODMR setup described in Chap. 2. The setup is slightly modified for the artificial signal detection. Figure 4.1 shows the configuration around the sample mount. A bulk of $\mathrm{II_a}$ pure diamond (Element Six electronic-grade) is placed below the waveguide using a double sided tape, and one of the single NV centers in the sample is chosen as a sensor. A permanent magnet attached to an aluminum arm connected to a three-axes

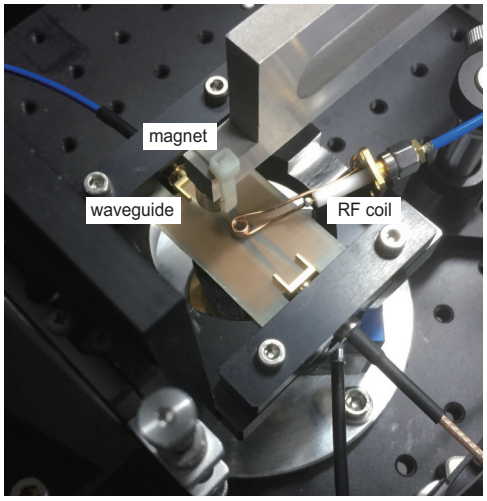

Figure 4.1: A photo of ODMR setup with RF coil.

stage is used to apply the offset magnetic field $B_0 = 29.8$ mT parallel to the sensor symmetry axis. A 30 μm diameter copper wire is placed across the diamond surface, and it is soldered on the waveguide to irradiate a microwave signal. The microwave signals are generated from a vector signal generator (VSG, Stanford research system SG396) modulated by an arbitrary waveform generator (AWG, Tektronix AWG7122c), and they go through an high power amplifier (Mini-Circuits ZHL-16W-43+) before they enter the waveguide. The microwave output frequency is tuned to 2036.4 MHz which is the resonance frequency between $m_S = 0$ and $m_S = -1$ of NV at $B_0 = 29.8$ mT. The pulse duration for CP sequence is calibrated by Rabi oscillation frequency, which is taken with either rectangular or cosine-square shape pulses. We set 23 ns and 76 ns for the rectangular shape $\pi/2$ pulse and the cosine-square shape π pulse, respectively. A handmade RF coil [middle of Fig. 4.1], which is connected to a function generator (FG, NF WF1973), is used to apply the target artificial magnetic field to the sensor spin. FG generates a continuous sinusoidal wave without any triggering or gating with AWG, thus the AC signal phase randomly changes for each measurement cycles.

Microwave generation and shaped pulses

We use IQ modulation of VSG using AWG to control the microwave pulse shape, frequency, and phase. An output signal of IQ modulation is determined by three input signals of IQ mixer; local oscillator (LO), I signal $I(t)$, and Q signal $Q(t)$. LO signal frequency is in the order of gigahertz and is generated from the signal generator part of

VSG. IQ signal frequency is in the order of sub-gigahertz and is generated from AWG. The output signal is given as,

$$V_{\text{out}}(t) = I(t)\cos(\omega_{\text{LO}}t + \phi_{\text{LO}}) + Q(t)\sin(\omega_{\text{LO}}t + \phi_{\text{LO}}), \tag{4.1}$$

where ω_{LO} (ϕ_{LO}) is frequency (phase) of LO signal. When IQ signals are restricted as,

$$I(t) = A_{\text{mod}}(t)\cos(\omega_{\text{mod}}t + \phi_{\text{mod}}), \tag{4.2}$$

$$Q(t) = -A_{\text{mod}}(t)\sin(\omega_{\text{mod}}t + \phi_{\text{mod}}), \tag{4.3}$$

Eq. (4.1) can be simplified to,

$$V_{\text{out}} = A_{\text{mod}}(t)\cos[(\omega_{\text{LO}} + \omega_{\text{mod}})t + (\phi_{\text{LO}} + \phi_{\text{mod}})], \tag{4.4}$$

where $A_{\text{mod}}(t)$, ω_{mod} and ϕ_{mod} are modulation envelope, frequency and phase, respectively. The output signal is synchronized with IQ signals, and its frequency/phase becomes the summation of the frequency/phase of LO and IQ signals.

The waveforms of IQ signals are calculated in MATLAB on the main PC, and they are uploaded to AWG through a GPIB interface for generation from two analog channels of AWG. We set AWG's sampling frequency at 1 GSa/s and ω_{mod} at 100 MHz. The frequency of LO is set as 1936.4 MHz to generate the microwave at 2036.4 MHz.

The three pulse shapes, rectangular pulse, cosine-square pulse, and chirp pulse, are used for the suitable control of the sensor spin. A rectangular pulse is used when the sensor spin needs to be flipped as fast as possible. The rectangular pulse shape is given by,

$$A_{\text{mod}}(t) = \begin{cases} 1 & \text{for } t_{\text{r}} \le t \le t_{\text{r}} + t_{\text{p}} \\ 0 & \text{for otherwise,} \end{cases} \tag{4.5}$$

where t_{r} is the timing of pulse rising and t_{p} is the duration of the pulse. Figure 4.2(a) shows an example of IQ signals for the rectangular pulse. Here t_{r} and t_{p} are restricted by the hardware sampling resolution; they can be tuned at 1 ns resolution for 1 GSa/s.

A cosine-square pulse is used to control the sensor spin with precision. The cosine-square pulse shape is given by,

$$A_{\text{mod}}(t) = \begin{cases} \sin^2\left[\frac{\pi(t-t_{\text{r}})}{t_{\text{p}}}\right] & \text{for } t_{\text{r}} \le t \le t_{\text{r}} + t_{\text{p}} \\ 0 & \text{for otherwise.} \end{cases} \tag{4.6}$$

Figure 4.2(b) shows an example of IQ signals for the cosine-square pulse. The pulse envelope is smoothly modulated, so that t_{r} and t_{p} can be tuned beyond hardware sampling

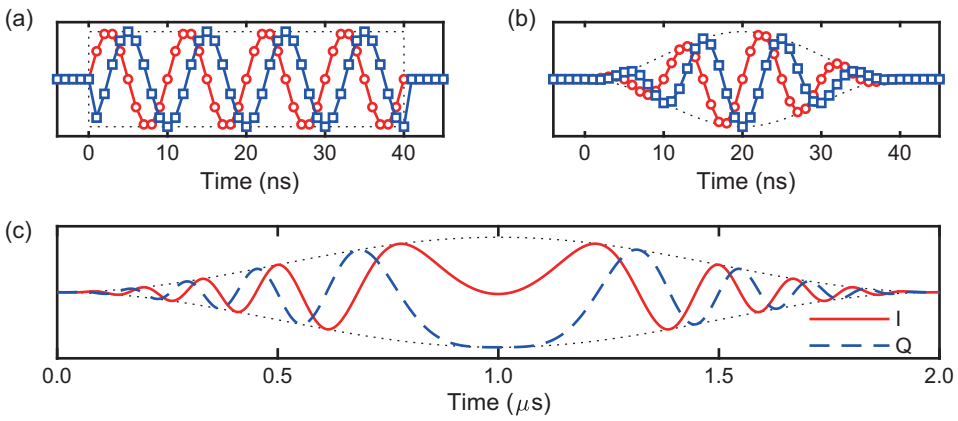

Figure 4.2: IQ signal waveform for the (a) rectangular shape [Eq. (4.5)] and (b) cosine-square pulses [Eq. (4.6)] when $\omega_{\mathrm{mod}}/2\pi = 100$ MHz, $\phi_{\mathrm{mod}} = 0°$, $t_{\mathrm{s}} = 0$, and $t_{\mathrm{p}} = 40$ ns. The circles (squares) represent the waveform for I (Q) signal. The phase of Q signal is shifted by $-\pi/2$ from that of I signal. Sampling frequency is 1 GSa/s and modulation frequency is 100 MHz. (c) IQ signal waveform for the chirped pulse [Eq. (4.7)] when $t_{\mathrm{p}} = 2$ μs, $\alpha_{\mathrm{p}} = 2$, and $\omega_{\mathrm{sweep}} = 20$ MHz. Here the modulation frequency is 0 for the sake of visibility. The dotted lines in (a-c) correspond modulation envelopes.

resolution [81]. We use this pulse shape for π pulses of CP sequence to precisely tune the modulation period.

A chirp pulse called WURST (wideband, uniform rate, smooth truncation) [148, 149] is used to robustly flip the sensor state from $m_S = 0$ to $m_S = -1$. The chirp pulse shape is given by,

$$A_{\mathrm{mod}}(t) = \begin{cases} 1 - \left|\cos\left[\frac{\pi(t-t_{\mathrm{r}})}{t_{\mathrm{p}}}\right]\right|^{\alpha_{\mathrm{p}}} & \text{for } t_{\mathrm{r}} \leq t \leq t_{\mathrm{r}} + t_{\mathrm{p}} \\ 0 & \text{for otherwise,} \end{cases} \tag{4.7}$$

where α_{p} is a parameter for envelope. The modulation frequency is linearly increased during the pulse duration, so that the modulation phase is given by,

$$\int_{t_{\mathrm{r}}}^{t} \left[\omega_{\mathrm{mod}} + \omega_{\mathrm{sweep}}\left(\frac{t' - t_{\mathrm{r}}}{t_{\mathrm{p}}} - \frac{1}{2}\right)\right] dt'. \tag{4.8}$$

where ω_{sweep} is the range of frequency sweep (the microwave frequency is swept from $\omega_{\mathrm{mod}} - \omega_{\mathrm{sweep}}/2$ to $\omega_{\mathrm{mod}} + \omega_{\mathrm{sweep}}/2$). Figure 4.2(c) shows an example IQ signals for the chirp pulse.

Data processing

We repeat each sensing condition until the total photon counts exceeds 10^4 to precisely obtain the averaged photon counts. The obtained photon counts are converted into the transition probability of the sensor spin state using the reference photon counts for $m_S = -1$ ($m_S = 0$). The reference photon count for $m_S = 0$ is obtained as a photon count without any microwave control, whereas the reference photon count for $m_S = -1$ is obtained as a photon count after sensor state flipping using a chirp pulse.

4.1.3 Spectroscopy of artificial signal

We first show principle of AC magnetometry using CP sequence. A timing relation between CP sequence and target AC field are shown in Fig. 4.3(a). A superposition state is prepared via green laser illumination and $\pi/2$ pulse, and Larmor precession of sensor spin starts subsequently. The precession frequency is modulated by target AC field, and the precession phase is accumulated by periodical application of π pulses at half of the target oscillation period. The phase accumulation is reflected in probability of $m_S = -1$ state at readout timing (we call transition probability) by rotating the superposition state by $\pi/2$ pulse.

Here, we introduce a theoretical model to discuss the phase accumulation. Generally, a target AC field is given by,

$$B_{\mathrm{ac}}(t) = b_{\mathrm{ac}} \cos\left(\omega_{\mathrm{ac}} t + \alpha\right), \tag{4.9}$$

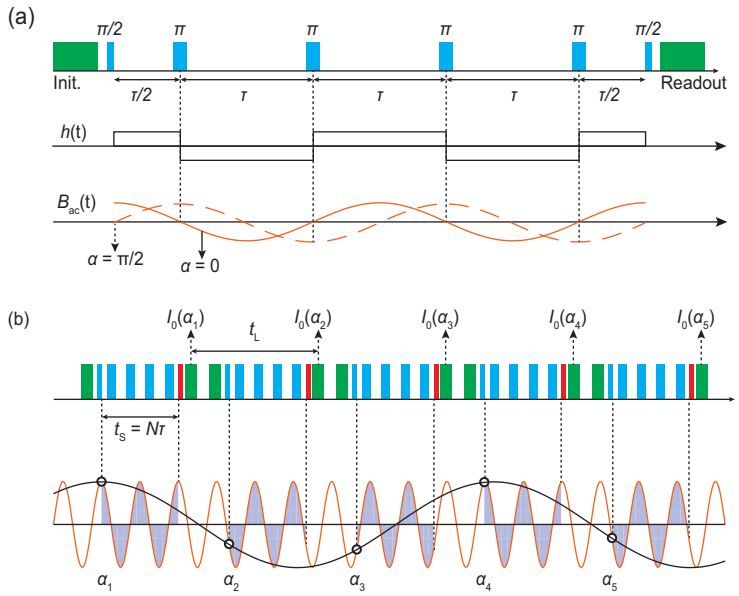

Figure 4.3: Principles of AC magnetometry. (a) Carr-Purcell sequence and (b) ultrahigh resolution sensing. Green blocks represent laser pulses. Blue (Red) blocks represent X (Y) phase microwave pulses. $h(t)$ represents the modulation function. $B_{\mathrm{ac}}(t)$ represents the target AC signal at $\alpha = 0$ (solid line) and $\alpha = \pi/2$ (dashed line).

where $b_{\rm ac}, \omega_{\rm ac}, \alpha$ are amplitude, frequency, and phase of target signal, respectively. Zeeman shift of the precession frequency is given as,

$$\delta\omega(t) \;=\; \gamma_{\rm e} b_{\rm ac} \cos\left(\omega_{\rm ac} t + \alpha\right). \tag{4.10}$$

The integrated phase is then described as,

$$\phi_{\rm acq} \;=\; \int_0^{N\tau} h(t)\gamma_{\rm e} b_{\rm ac} \cos\left(\omega_{\rm ac} t + \alpha\right) dt, \tag{4.11}$$

where N is the even integer representing the number of π pulses for CP sequence, and $\gamma_{\rm e}/2\pi = 28$ GHz/T is the gyromagnetic ratio of electron spin. $h(t)$ is the modulation function given by,

$$h(t) \;=\; \begin{cases} -1 & \left(\frac{1}{2} - n\right)\tau < t < \left(\frac{3}{2} - n\right)\tau \\ 1 & \text{otherwise,} \end{cases} \tag{4.12}$$

where n is the integer below N, and τ is the time interval between π pulses. The sign of the modulation function is changed with the π pulse timing as shown in Fig. 4.3(a). Using Eq. (4.12), Eq. (4.11) is explicated as,

$$\begin{aligned} \phi_{\rm acq} \;&=\; \frac{\gamma_{\rm e} b_{\rm ac}}{\omega_{\rm ac}} [-\sin(\alpha) + (-1)^N \sin\left(\omega_{\rm ac} N\tau + \alpha\right) \\ &\quad +2\sum_{j=1}^{N} (-1)^{N-1} \sin\left(\omega_{\rm ac} t_j + \alpha\right)] \\ &=\; \gamma_{\rm e} b_{\rm ac} N\tau \times W(\tau, \omega_{\rm ac}, \alpha), \end{aligned} \tag{4.13}$$

with

$$W(\tau, \omega_{\rm ac}, \alpha) = \frac{\sin\left(N\omega_{\rm ac}\tau/2\right)}{N\omega_{\rm ac}\tau/2} [1 - \sec\left(\omega_{\rm ac}\tau/2\right)] \cos\left(N\omega_{\rm ac}\tau/2 + \alpha\right), \tag{4.14}$$

where t_j is the time span between first $\pi/2$ pulse to jth π pulse and $W(\tau, f_{\rm ac}, \alpha)$ is the filter function. Similar to DC magnetometry based on Ramsey interferometry, the phase accumulation is proportional to multiple of the target field strength and sensing duration. On the other hand, AC magnetometry is robust against the microwave detuning because it averages out the time independent component ($\int_0^{N\tau} h(t)dt = 0$).

The essential component for AC magnetometry is the filter function, which is controlled with τ to determine the detection frequency component. The filter function depends on α, for example, a finite phase is accumulated when $\alpha = 0$ but no phase is accumulated when $\alpha = \pi$ [Fig. 4.3(a)]. The target signal is not normally synchronized

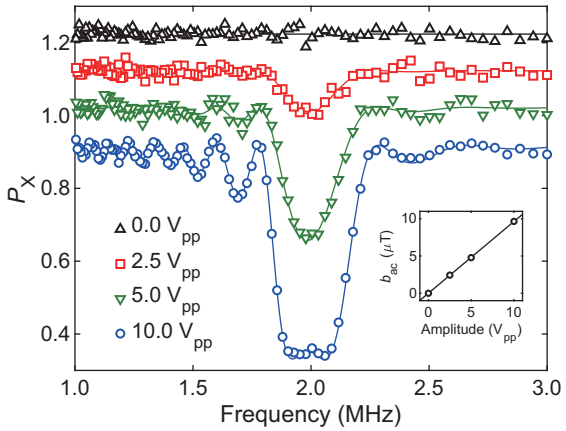

Figure 4.4: AC magnetometry with a single NV center utilizing XY16 sequence ($N = 16$) as sweeping τ. Target AC signal frequency is 2 MHz. The inset shows the relation between FG output amplitude and obtained AC field strength. (This figure is reproduced from Ref. [150].)

with the microwave pulses, and α randomly changes for each measurement cycle. By taking an average against α, the transition probability is calculated as,

$$\begin{aligned} P_{\mathrm{X}} &= \frac{1}{2}\left[1 + \frac{1}{2\pi}\int_0^{2\pi} \cos\left\{\gamma_{\mathrm{e}} b_{\mathrm{ac}} N\tau W(\omega_{\mathrm{ac}}, \alpha)\right\} d\alpha\right] \\ &= \frac{1}{2}\left[1 + J_0(\gamma_{\mathrm{e}} b_{\mathrm{ac}} N\tau W_{N,\tau})\right], \end{aligned} \tag{4.15}$$

where P_{X} is the transition probability after $(\pi/2)_{\mathrm{X}}$ readout pulse, and J_0 is the Bessel function of the first kind for $n = 0$. $W_{N,\tau}$ is the averaged filter function for the random phase measurement, and it is calculated as,

$$W_{N,\tau} = \left|\frac{\sin\left(\omega_{\mathrm{ac}} N\tau/2\right)}{\omega_{\mathrm{ac}} N\tau/2}\left[1 - \sec\left(\omega_{\mathrm{ac}}\tau/2\right)\right]\right|. \tag{4.16}$$

This filter function takes maximum when $\tau \sim \pi/\omega_{\mathrm{ac}}$, so that the detection frequency can be considered as $1/2\tau$, in the unit of Hz.

Now, we experimentally examine AC magnetometry with an artificial signal generated by the RF coil connected with FG. Figure 4.4 shows spectroscopy results taken by CP sequence ($N = 16$) as sweeping τ. We used XY16 phase cycle for CP sequence, such as X–Y–X–Y–Y–X–Y–X–$\bar{\mathrm{X}}$–$\bar{\mathrm{Y}}$–$\bar{\mathrm{X}}$–$\bar{\mathrm{Y}}$–$\bar{\mathrm{Y}}$–$\bar{\mathrm{X}}$–$\bar{\mathrm{Y}}$–$\bar{\mathrm{X}}$, to robustly control the sensor spin against pulse errors [145]. We set FG's output frequency as 2 MHz, and take the spectrum as

sweeping τ for FG's output amplitude of 0.0, 2.5, 5.0, and 10.0 V_{pp}. A visible dip is observed around the target signal frequency when the output amplitude is > 0.0 V_{pp}. The obtained spectrum are well fitted by Eq. (4.15), and b_{ac} for each output amplitude is extracted as in the inset of Fig. 4.4. They linearly depend on the output voltage as expected from Ampére's Law, and we extract the irradiation efficiency of our RF system as 964 nT/V_{pp}.

The spectrum resolution, full width at half maximum (FWHM) of the spectrum, is described as an inverse of the sensing duration $t_s = 1/N\tau$. An ideal resolution for our measurement is given as $\omega_{ac}/\pi N = 250$ kHz when detection frequency is 2 MHz, and it is consistent with our observation in Fig. 4.4. The linewidth of the spectrum for 10.0 V_{pp} is slightly wider than other conditions because the target signal is strong enough to accumulate the phase near π even for our slightly detuned condition.

There are ^{13}C nuclei (1.1 % abundance) around the sensor spin, and its NMR can modulate the transition probability. We can ignore this effect because our measurement range, 1 MHz to 3 MHz, is much far from 319 kHz, the bare Larmor frequency of ^{13}C at $B_0 = 29.8$ mT.

In this session, we have shown the principle of AC magnetometry and the successful detection of the artificial signal with CP sequence. This method is also applicable for NMR spectroscopy. Actually, sensor decoherence degrades the sensing contrast, thus the sensing duration is limited by the sensor coherence time T_2, which is often less than 1 ms in the ambient condition. Even when this sensing duration is limited, the spectrum resolution can be enhanced by prolonging the sequence duration by temporally transferring the sensor phase information into the sensor population [53, 54, 71] or into the nuclear spin memory [78]. The sequence duration can then be prolonged up to the sensor relaxation time $T_1 \sim 10$ ms or to the nuclear spin coherence time $T_{2n}^* \sim 1$ s. Previously, the chemical shift of external diffusing molecules has been resolved using a shallow single NV center in a highly stabilized high magnetic field ODMR system [80]. The improvements of AC magnetometry protocol are important for NV's successful application on nanoscale NMR.

4.1.4 Ultrahigh resolution sensing

The spectrum resolution of AC magnetometry has been enhanced by prolonging the sequence duration, but the sensitivity has not been enhanced. In those high resolution sensing, we often measure multiple sampling points for τ to obtain AC spectrum because their detection bandwidths are narrow. It makes the total measurement time longer, thus the resulting sensitivity can be worse. In the middle of 2017, an ultra high resolution sensing protocol which achieves coherence unlimited spectrum resolution was developed

independently by Ulm University [84], ETH [83], and Harvard University [85]. This protocol requires only single condition of τ with a short sensing duration to obtain a spectrum. Therefore, the high sensitivity and wide detection bandwidth can be achieved at the same time as shown for NMR by Glenn *et al.* who resolved the chemical shift and J coupling of external organic molecule ensembles at the ambient condition.

Here, we show how to perform this ultrahigh resolution sensing. We describe the mechanism based on theoretical model followed by experimental demonstration of the coherence unlimited spectrum resolution by detecting an artificial signal.

The basic idea of ultrahigh resolution is simple. Figure 4.1(b) shows the principle of the ultrahigh resolution sensing. In this protocol, CP sequence near the resonance condition is repeated many times. The target signal phase for each CP sequence advances as,

$$\alpha_{j+1} = \omega_{\rm ac} t_{\rm L} + \alpha_j \tag{4.17}$$

where $\alpha_{\rm j}$ is the target signal phase at jth measurement and $t_{\rm L}$ is the sequence length including initialization and readout. α_j is reflected in the photon counts because the filter function depends on the target phase. We can extract the target signal frequency information from Fourier transform of the photon counts. The timing of CP sequences is kept by a classical clock of microwave system, so that the spectrum resolution can be as good as the clock stability, which is normally better than 1 ppm.

Now, we discuss the ultrahigh resolution sensing based on the theoretical model. We assume that target frequency is vaguely determined, and signal strength is weak. Such situation can be found for detection of a single nuclear spin in a calibrated magnetic field. At the resonance condition $\tau = \pi/\omega_{\rm ac}$, the filter function [Eq. (4.14)] is simplified as,

$$W(\pi/\omega_{\rm ac}, \omega_{\rm ac}, \alpha) = \frac{2}{\pi}\cos\alpha, \tag{4.18}$$

thus the transition probability at jth CP sequence with $(\pi/2)_{\rm Y}$ readout pulse is obtained as,

$$\begin{aligned} P_{{\rm Y},j} &= \frac{1}{2}\left[1 + \sin\left\{\frac{2}{\pi}\gamma_{\rm e} b_{\rm ac} N\tau\cos\alpha_j\right\}\right] \\ &\approx \frac{1}{2}\left[1 + \frac{2}{\pi}\gamma_{\rm e} b_{\rm ac} N\tau\cos\alpha_j\right], \end{aligned} \tag{4.19}$$

where $P_{\rm Y}$ is the transition probability. We use an approximation, $\sin(\phi_{\rm acq}) \approx \phi_{\rm acq}$, by assuming a weak signal condition which satisfies $\phi_{\rm acq} = \frac{2}{\pi}\gamma_{\rm e} b_{\rm ac} N\tau << 1$. On the other hand, the probability with $(\pi/2)_{\rm X}$ readout pulse is given as $P_{\rm X} \approx 1 - \frac{\phi_{\rm acq}^2}{2}$. Y phase readout has a benefit for high sensitivity detection because $\phi_{\rm acq} > \phi_{\rm acq}^2$ is valid, thus the

signal contrast for Y phase readout is larger than that of X phase readout. Estimated photon counts at jth CP sequence are then given by,

$$I_0(\alpha_j) \approx \frac{\beta_0 - \beta_1}{2}\left[1 + \frac{2}{\pi}\gamma_e b_{ac} N\tau \cos\alpha_j\right] + \frac{\beta_0 + \beta_1}{2}, \tag{4.20}$$

where β_0 and β_1 are the photon counts for $m_S = 0$ and $m_S = -1$, respectively. Using Eq. (4.17) and Eq (4.20), the phase dependent component of the photon counts is extracted as,

$$\delta I_0(t) \approx \frac{\beta_0 - \beta_1}{\pi}\gamma_e b_{ac} N\tau \cos(\omega_{ac} t + \alpha), \tag{4.21}$$

where t is the timing of CP sequences and α is the initial phase of target signal. According to Eq. (4.21), the target signal frequency can be obtained by Fourier transform of the photon counts, and the spectrum resolution is determined as $1/T$, where $T = Mt_L$ is the total measurement duration. The resolution can be arbitrarily tuned by M, thus sensor coherence unlimited resolution is achievable. The spectroscopy is much faster than the AC magnetometry shown in Fig. 4.4 because we don't have to sweep τ. Additionally, the detection bandwidth is same as the AC magnetometry because single CP sequence duration is same.

To extract the original frequency and phase of the target signal, appropriate conversion of the obtained frequency and phase is required. The sampling interval t_L is always longer than the sensing duration $t_s \geq \pi/\omega_{ac}$, so that Nyquist frequency $\omega_L \equiv \pi/t_L$ is smaller than the target frequency. This situation is called an undersampling condition. The relation between Nyquist frequency and the target frequency is written as,

$$m\omega_N \leq \omega_{ac} < (m+1)\omega_N, \tag{4.22}$$

where m is the integer which characterizes the undersampling condition. The slowly oscillating signal in Fig. 4.1(b) is an example of undersampled signal for $m = 6$. When m is even, the original frequency is extracted as,

$$\omega_{ac} = \omega_{ac}^{(m)} + m\omega_N, \tag{4.23}$$

where $\omega_{ac}^{(m)}$ is the obtained frequency of the undersampled signal. These frequencies should satisfy a relation,

$$\omega_{ac}^{(m)}(t_0 + jt_L) + \alpha^{(m)} = \omega_{ac}(t_0 + t_L) + \alpha, \tag{4.24}$$

where j is the integer, t_0 is the first sampling timing, and $\alpha^{(m)}$ is the obtained phase of the undersampled signal. Using Eq. (4.23) and Eq. (4.24), the original phase is extracted

as,

$$\begin{aligned} \alpha &= \alpha^{(m)} - m\omega_{\mathrm{N}}(t_0 + kt_{\mathrm{L}}), \\ &= \alpha^{(m)} - m\frac{\pi t_0}{t_{\mathrm{L}}} \ (\mathrm{mod}\ 2\pi). \end{aligned} \tag{4.25}$$

Using Eq. (4.23) and Eq. (4.25), the target signal parameters are obtained with the vague knowledge of original frequency.

Now, we experimentally demonstrate the ultrahigh resolution sensing. We set the FG output frequency and amplitude as $\omega_{\mathrm{ac}}/2\pi = 2.001$ MHz and 0.1 V_{pp}, respectively. The output amplitude corresponds to the target field amplitude of 96.4 nT, which is extracted using irradiation efficiency obtained in Sec. 4.1.2. CP sequence ($N = 256$ and $\tau = 250$ ns) with XY 16 phase cycle is used for the weak signal detection. We set the sampling interval as $t_{\mathrm{L}} = 69.5$ μs so the undersampling condition is estimated as $m = 278$ from Eq. (4.22). According to Eq. (4.23), the original frequency should be extracted as $\omega_{\mathrm{ac}} = \omega_{\mathrm{ac}}^{(278)} + 2\pi \times 2$ MHz. We set $M = 51798562$ and it corresponds to the total measurement duration of 1 hour.

Figure 4.5(a-d) show FFT spectra of photon counts obtained with the ultrahigh resolution sensing until $T = 300$ s, $T = 900$ s, $T = 1800$ s, and $T = 3600$ s. The red solid lines in Fig. 4.5(a-d) are Gaussian fitting including the baseline. Figure 4.5(e) shows a relation between obtained FWHM and T. The relation agrees very well with the Fourier limit resolution FWHM $= 1/T$ shown by the dashed line in Fig. 4.5(e), and we experimentally obtain 304 μs resolution for $T = 3600$ s. Figure 4.5(f) shows signal-to-noise-ratio (SNR) extracted as the ratio between Gaussian peak amplitude and its baseline. It can be well fitted with the photon shot noise scaling SNR $\propto \sqrt{T}$ as expected. The frequency precision thus scales with $T^{-1} \times T^{-0.5} = T^{-1.5}$, which is much better than AC magnetometry described in Sec. 4.1.3.

Additionally, the original phase can also be extracted as $-165.8°$ from Eq. (4.25) using $t_0 = 0$ and the obtained FFT phase. We extract the original phase just for demonstration because the target signal is not synchronized with the microwave pulse system, and the phase can be different on other measurement shots.

4.1.5 Conclusion

In this section, we have examined the state-of-the-art AC magnetometry, including CP sequence and the ultrahigh resolution sensing. Using the ultrahigh resolution sensing, we have successfully achieved spectrum resolution of 304 μHz with 1-hour measurement duration which is high enough to resolve the chemical shift and J coupling. The next step towards NV-based nanoscale NMR is to obtain the single nuclear spin sensitivity. Unlike

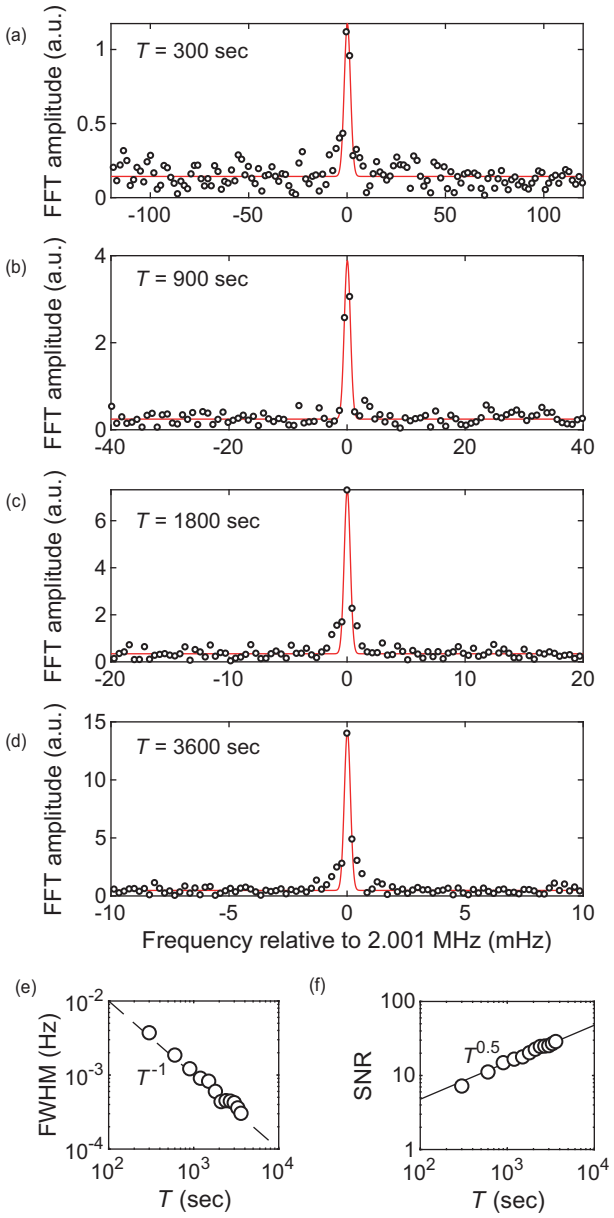

Figure 4.5: Ultrahigh resolution sensing of AC signal at 2.001 MHz. FFT spectra of photon counts for (a) $T = 300$ s, (b) $T = 900$ s, (c) $T = 1800$ s, and (d) $T = 3600$ s. Red solid lines are Gaussian fitting including baseline. The explicit fitting formula is given as, $C_{\text{base}} + C_{\text{peak}} e^{-\left(\frac{x-\omega_{\text{ac}}}{\delta\nu/\sqrt{2\log 2}}\right)^2}$, where C_{base} is the baseline, C_{peak} is the peak strength, and ω_{ac} is the target frequency, and $\delta\nu$ is FWHM. (e) FWHM as a function of T. The dashed line represents Fourier resolution limit. (f) SNR as a function of T. The solid line represents $\text{SNR} = 0.48 \times T^{0.5}$. (This figure is partially reproduced from Ref. [150].)

the artificial signal sensing demonstrated in this section, a sensor spin in the actual nano NMR is not continuously exposed to the free nuclear precession due to the mixed-state nature of nuclear spins at the ambient condition. Therefore, abilities to excite and detect the free nuclear precession, polarization and tipping of a target spin are essential. We will further discuss how to apply these state-of-the-art AC magnetometry for NMR in Sec. 4.2,

4.2 Nuclear spin detection

We report on a nanoscale quantum sensing protocol which tracks a free precession of a single nuclear spin and is capable of estimating an azimuthal angle—a parameter which standard multipulse protocols cannot determine—of the target nucleus. Our protocol combines pulsed dynamic nuclear polarization, a phase-controlled radio-frequency pulse, and a multipulse ac sensing sequence with a modified readout pulse. Using a single nitrogen-vacancy center as a solid-state quantum sensor, we experimentally demonstrate this protocol on a single ^{13}C nuclear spin in diamond and uniquely determine the lattice site of the target nucleus. Our result paves the way for magnetic resonance imaging at the single-molecular level.

4.2.1 Introduction

Nuclear magnetic resonance (NMR) spectroscopy is an analytical technique extensively used in chemistry, biology, and medicine. It achieves sub-ppm spectral resolutions to provide a wealth of information on the structure and chemical environment of molecules, but requires at least nanoliter-volume analytes containing an ensemble of identical nuclei, due to the insensitive induction detection the technique relies on. In recent years, single isolated electron spins in solids, most prominently those associated with nitrogen-vacancy (NV) centers in diamond [95, 96, 150], have emerged as atomic-scale quantum sensors capable of detecting weakly coupled external nuclei in as small as zeptoliter volumes, a dramatic decrease compared with conventional NMR [46, 47, 49]. Furthermore, various NMR protocols, in which a train of properly timed microwave pulses interrogates precessing nuclear spins via the interaction with the sensor electron spin, have been devised and applied to external nuclei, demonstrating identifications of isotopes [51,151,152], detection

This chapter is reproduced from *K. Sasaki, K. M. Itoh and E. Abe, Determination of the position of a single nuclear spin from free nuclear precessions detected by a solid-state quantum sensor. Physics Review B Vol. 98, 121405 (2018)*, with the permission of APS Publishing.

of single protons [52], spectroscopy of single proteins [79], spectral resolution approaching that of conventional NMR [80, 85], and so on [153–156]. A far-reaching yet natural goal of this line of research is a chemical structure analysis at the single-molecular level, i.e., the determination of chemical identities and locations of the constituent nuclei in a single molecule.

For nuclei dipolarly coupled with a sensor, the knowledge of the hyperfine parameters $A_\parallel$ and $A_\perp$ (the parallel and perpendicular components, respectively) translates to the coordinate parameters r and θ, the distance from the sensor and the tilt (polar angle) from the applied static magnetic field B_0, respectively, owing to the form of the interaction $\propto (3\cos^2\theta - 1)/r^3$ or $3\cos\theta\sin\theta/r^3$ [Fig. 4.6(a), left]. ^{13}C nuclei ($I = 1/2$) in diamond sensed by the NV electronic spin ($S = 1$) have served as a canonical testbed for various NMR protocols to characterize the hyperfine parameters [43–45,53,54,71,78,150,157]. For instance, in correlation spectroscopy, a multipulse sequence is repeated with the interval of $t_{\rm corr}$, during which a target nuclear spin evolves freely. Boss *et al.* demonstrated that, by engineering the Hamiltonian during the free nuclear precession, both $A_\parallel$ and $A_\perp$ can be estimated with high precision [71]. The information that is still missing in order to uniquely determine the position of a target nuclear spin is the azimuthal angle ϕ [158–160], which, due to the symmetry of the interaction, does not formally appear in the Hamiltonian.

In this Sec. 4.2, we show that the azimuthal angle can be determined by a multipulse protocol combined with dynamic nuclear polarization (DNP) and radio-frequency (rf) control of a target spin. As a proof of principle, we apply this protocol to the NV-^{13}C-coupled system, and uniquely assign the lattice site that the ^{13}C nucleus sits in, even when multiple sites equivalent to it exist.

4.2.2 Method

Our protocol proceeds as follows [see Figs. 4.6(b)- 4.6(g) for the pulse sequences used]. The target nuclear spin is first polarized by transferring the polarization of the sensor electron spin using a multipulse sequence called PulsePol [86], and is tipped to the xy plane by an rf $\pi/2$ pulse. The dipolar field experienced by this tipped nuclear spin is dependent on ϕ; an example to appreciate this is that, when two nuclear spins are located on opposite sides of the sensor, the directions of the dipolar fields are also opposite [Fig. 4.6(a), middle]. A subsequent free precession of each nuclear spin carries this information as the initial phase of the oscillation [Fig. 4.6(a), right].

A central issue that must be addressed in this scenario is how to detect the phase of a nuclear precession. Here, we consider a particular example in which $|m_S = 0\rangle$ and

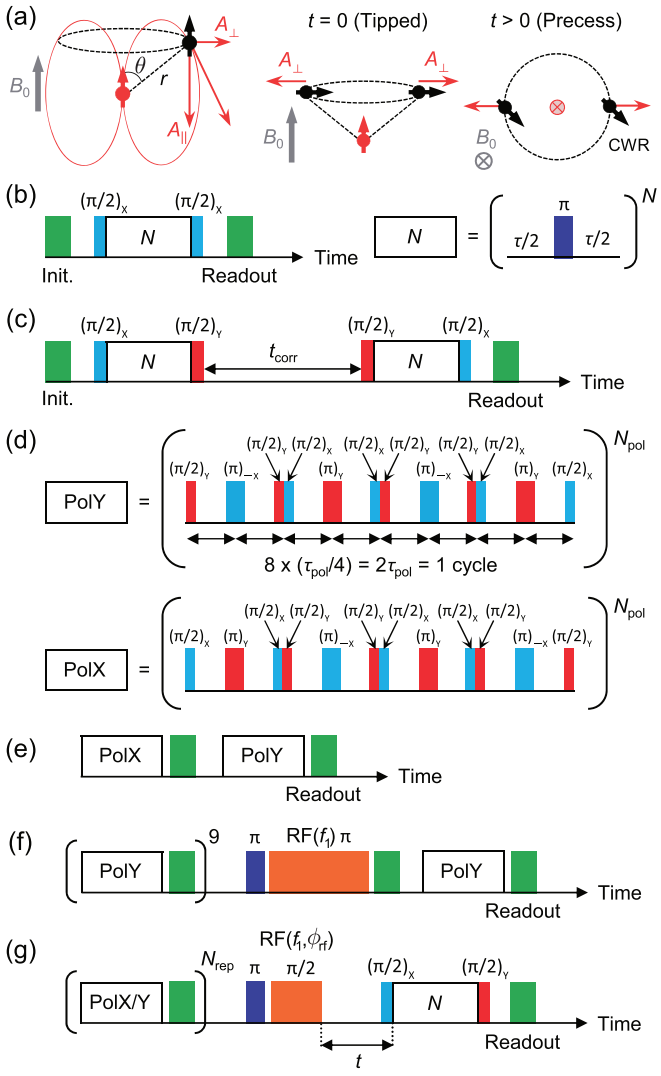

Figure 4.6: (a) Schematic showing the sensor electron spin (in red) and the target nuclear spin (in black) coupled via the dipolar interaction under a static magnetic field B_0 (left). When a nuclear spin is tipped, the direction of the hyperfine field relative to the nuclear spin is dependent on the azimuthal angle (middle), and this information is reflected on the phase of a subsequent nuclear precession (right). CWR: Clockwise rotation. (b)(g) Pulse sequences used in the present work. (b) Carr-Purcell (CP) sequence. (c) Correlation spectroscopy. (d) PulsePol sequences for DNP. (e) Successive application of PolX and PolY to examine the polarization transfer. (f) Sequence to selectively polarize a single nuclear spin. (g) Protocol to determine the azimuthal angle. (This figure is reproduced from Ref. [93].)

$|m_S = -1\rangle$ sublevels of the NV spin serve respectively as $|0\rangle$ and $|1\rangle$ of the sensor two-level system, but the concept is general. To detect a dynamics of a single nuclear spin, the sensor spin is prepared in a superposition of $|m_S = 0\rangle$ and $|m_S = -1\rangle$, and is subject to a Carr-Purcell (CP) sequence [143] consisting of N π pulses equally separated by τ [Fig. 4.6(b)]. Because only $|m_S = -1\rangle$ can hyperfine couple with the nuclear spin, the two sensor states act differently on the nuclear spin, making it rotate around different axes, say, $\boldsymbol{n}_0$ and $\boldsymbol{n}_1$. Different nuclear dynamics are combined by the final $(\pi/2)_{\rm X}$ pulse ($\pi/2$ pulse with the X phase defined in the rotating frame of reference). The transition probability $P_{\rm X}$ of the sensor is given by [44]

$$P_{\rm X} = 1 - \frac{1}{2}(1 - \boldsymbol{n}_0 \cdot \boldsymbol{n}_1) \sin^2 \frac{N\phi_{\rm cp}}{2}. \tag{4.26}$$

When τ is chosen properly, $\phi_{\rm cp}$ and $\boldsymbol{n}_0 \cdot \boldsymbol{n}_1$ carry the information on a single nuclear spin. This readout pulse has been extensively used to probe the nuclear dynamics in the past [44, 161], but does not depend on the free precession angle of the nuclear spin.

In our protocol, we instead use a $(\pi/2)_{\rm Y}$ pulse for the readout. The transition probability becomes

$$P_{\rm Y} = \frac{1}{2} - \frac{1}{2} \cos(\phi - \phi_{\rm n}) \sin N\phi_{\rm cp}, \tag{4.27}$$

where $\phi_{\rm n}$ is the azimuthal angle of the nuclear spin measured in real space. A detailed deviation of Eq. (4.27) is given in the Appendix C. We measure a free precession of a nuclear spin, which oscillates as $\cos(2\pi f_{\rm p} t + \phi_0)$. ϕ is determined as $\phi = \phi_{\rm n}(0) + \phi_0$. $\phi_{\rm n}(0)$ is the azimuthal angle of the nuclear spin at $t = 0$ [defined as the end time of an rf pulse, Fig. 4.6(g)]. While to our knowledge Eq. (4.27) has not been explicitly given in previous literature, a recent demonstration of high-resolution spectroscopy of nuclear spin ensembles does employ this $(\pi/2)_{\rm Y}$ readout [85]. There, an oscillating collective magnetization induced by an rf pulse is phase coherent, and a free nuclear precession analogous to a free induction decay in conventional NMR has been recorded (called the coherently averaged synchronized readout). It should be noted that, for a single unpolarized nuclear spin, random nuclear orientations average out nuclear precession signals. We detect a freely precessing single nuclear spin by polarizing it, and in this case the signal is coherently averaged to reveal its oscillation phase.

4.2.3 Determination of r and θ of a single ^{13}C spin position

Experiments were performed using a type-IIa (001) diamond substrate from Element Six. Single negatively charged NV centers in bulk (~ 50 μm deep) are optically resolved by a home-built confocal microscope equipped with a 515-nm excitation laser for the

initialization and readout of the NV spin. The fluorescence from a single NV center is collected by a single-photon counting module, and the microwave to manipulate the NV spin is delivered through a copper wire running across the diamond surface. The rf signal to control ^{13}C nuclei (1.1 % abundance and the gyromagnetic ratio γ_c of 10.705 kHz/mT) is generated by a hand-wound coil bonded on the back side of the sample mount. This configuration makes the magnetic field from the coil roughly point normal to the sample surface, but the deviation from it is carefully calibrated [see Appendix C]. We select an NV center with its symmetry axis along the $[\bar{1}\bar{1}1]$ crystallographic direction, and B_0 of 36.2 mT is applied along the same direction.

We first characterize the magnetic environment of this NV sensor. The primary purpose here is to find a single ^{13}C nucleus whose coordinate parameters r and θ are known so that our protocol may be applied to determine ϕ and thus its exact position (lattice site). We apply the CP sequence, in which τ is incremented with N fixed as 16, and obtain the spectrum shown in Fig. 4.7(a). The broad dip observed around the bare ^{13}C Larmor frequency $f_c = \gamma_c B_0 = 387.5$ kHz originates from weakly coupled bath ^{13}C nuclei, whereas the sharp dip at $f_t = 301.6$ kHz is indicative of a single ^{13}C nucleus strongly coupled to the sensor. The latter signal is examined in more detail by incrementing N of the CP sequence with τ fixed at a near-resonance condition of 1.6875 μs $= 1/(2\times 296$ kHz) [Fig. 4.7(b)]. The ^{13}C nuclear spin then nutates approximately about the $A_\perp$ axis. For sufficiently large N, it makes coherent, full 2π rotations multiple times at the frequency f_{cp} of 10.2 kHz. Simulations also confirm that we are observing a single nuclear spin and not multiple nuclear spins with the same hyperfine parameters [see Appendix C].

We further analyze this ^{13}C nucleus by correlation spectroscopy [Fig. 4.6(c)]. Figure 4.7(c) shows a modulated oscillation as increasing t_{corr}, and its Fourier transformation reveals two peaks at $f_0 = 387.5$ kHz and $f_1 = 215.6$ kHz. f_0 corresponds exactly to f_c, and therefore results from the coupling with $|m_S = 0\rangle$. On the other hand, $|m_S = -1\rangle$ exerts the hyperfine field on the nuclear spin, shifting its precession frequency. The target nuclear spin is properly probed because $(f_0 + f_1)/2 = 301.55$ kHz $= f_t$, and the negative shift ($f_1 f_0 < 0$) suggests negative $A_\parallel$. Combining these results, we deduce $A_\parallel = -173.1$ kHz and $A_\perp = 22.3$ kHz with an accuracy of about 0.1 kHz [see Appendix C].

It should be noted that, unlike the case of external nuclear spins, $A_\parallel$ and $A_\perp$ estimated here are not purely dipolar in nature due to the presence of a relatively strong contact hyperfine interaction. This usually complicates the direct estimation of the coordinate parameters r and θ from $A_\parallel$ and $A_\perp$. However, the estimated values are accurate enough to be compared with theoretical calculations. Nizovtsev *et al.* have recently performed an extensive density functional theory (DFT) simulation of a $C_{510}[NV]H_{252}$ cluster [162]. From their list of hyperfine parameters for 510 carbon sites, we find that six sites labeled as

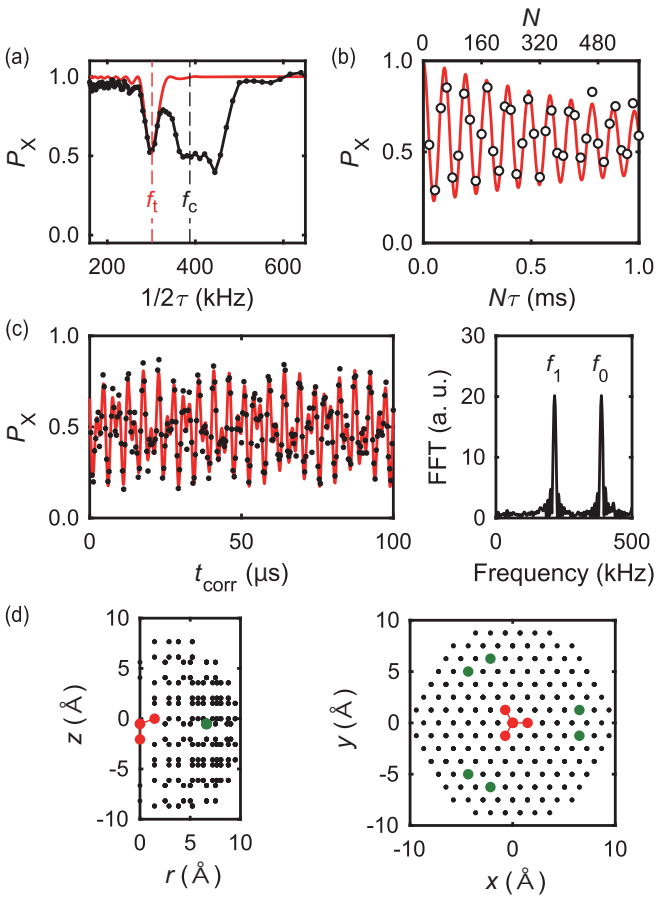

Figure 4.7: (a) NMR spectrum taken by the CP sequence ($N = 16$). $f_c = 387.5$ kHz and $f_t = 301.6$ kHz. (b) CP sequence as N is incremented ($\tau = 1.6875$ μs). (c) Correlation spectroscopy and its Fourier transform. $f_0 = 387.5$ kHz and $f_1 = 215.6$ kHz. In (a)(c), the red solid lines are simulations using the estimated values of $A_\parallel$ and $A_\perp$. (d) Map of the diamond lattice. The x, y, and z axes are parallel to the $[\bar{1}\bar{1}2]$, $[1\bar{1}0]$, and $[\bar{1}\bar{1}1]$ crystallographic directions, respectively. The black dots represent carbon sites, and the green dots are the candidate sites of the ^{13}C nucleus examined. It is assumed that the vacancy site locates above the nitrogen site, and the origin is taken 0.75 Å above the vacancy site [see Appendix C]. (This figure is reproduced from Ref. [93].)

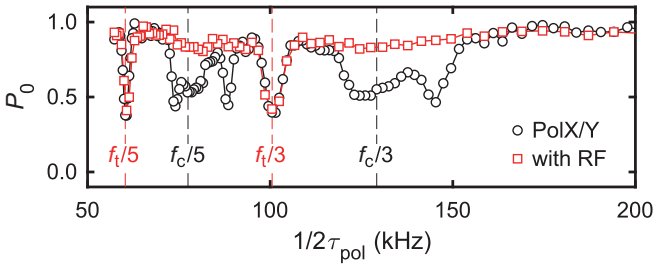

Figure 4.8: Demonstration of PulsePol on bath nuclear spins (∘) and on a single, selectively addressed nuclear spin (□). (This figure is reproduced from Ref. [93].)

C_{218}, C_{226}, C_{230}, C_{240}, C_{280}, and C_{282} show close agreement with the experimental values. The hyperfine parameters of these sites are, in kHz units, $(A_\parallel, A_\perp) = (-175.4, 21.7)$, $(-176.7, 21.7)$, $(-174.7, 21.7)$, $(-177.1, 21.9)$, $(-173, 22)$, and $(-173.4, 22.1)$, respectively [average: $(-175.1 \pm 2.1, 21.9 \pm 0.2)$]. The positions of these candidate sites are given in Fig. 4.7(d). In all cases, we obtain $r = 6.84$ Å and $\theta = 94.8°$ [see Appendix C].

4.2.4 Dynamic nuclear polarization of the ^{13}C spin

The next task is to polarize the target nuclear spin. For this, we use a pulsed technique called PulsePol, which is yet another application of Hamiltonian engineering [86]. Figure 4.6(d) shows two PulsePol sequences labeled as PolY and PolX. One cycle consists of eight pulses with a total duration of $2\tau_{\rm pol}$. When $2\tau_{\rm pol} = k/f_{\rm n}$ is satisfied (k: odd integer; $f_{\rm n}$: nuclear Larmor frequency), the average Hamiltonian of a hyperfine-coupled electron-nuclear system becomes proportional to $S_+I_- + S_-I_+$ (flip-flop) or $S_+I_+ + S_-I_-$ (flip-flip), driving the polarization transfer between the electron and the nuclei. It is shown that for $k = 3$ PolY (PolX) drives flip-flip (flip-flop), whereas for $k = 5$ PolY (PolX) does flip-flop (flipflip) [see Appendix C]. Because the NV spin is optically initialized into $m_S = 0$, PolY (PolX) for $k = 3$ polarizes the nuclei into $m_I = \frac{1}{2}$ ($\frac{1}{2}$). For $k = 5$, the direction of the nuclear polarization becomes opposite.

We test the performance of PulsePol by successive application of PolX and PolY, as shown in Fig. 4.6(e). The first PolX serves to depolarize the nuclear polarization during a previous run, and the polarization transfer by PolY is read out as a decrease of the $m_S = 0$ polarization (P_0) [163]. The circle (∘) points in Fig. 4.8 are the result of this measurement with $N_{\rm pol} = 5$. Two replicas of the NMR spectrum in Fig. 4.7(a) are clearly observed at $\frac{1}{3}$ and $\frac{1}{5}$ of the NMR conditions, as expected. Furthermore, a single nuclear spin can be selectively polarized by applying the sequence of Fig. 4.6(f). This sequence

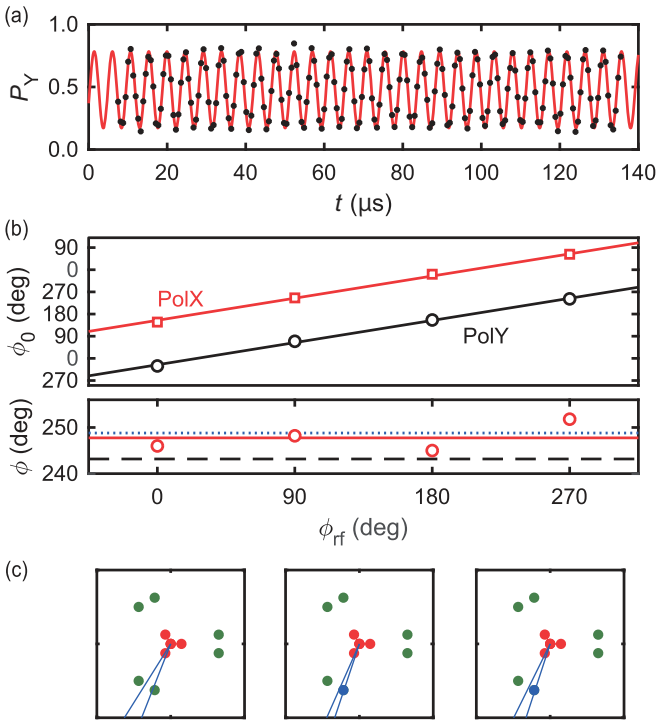

Figure 4.9: (a) P_Y as a function of t reveals a free precession of a single nuclear spin. (b) ϕ_0 as a function of ϕ_{rf} (upper panel). The solid lines are linear fits. Estimated ϕ (lower panel). (c) The blue lines indicate the accuracy ranges of ϕ, based on three estimations of $\phi_n(0)$. At most one lattice site (in blue) with $\phi = 250.9°$ falls on the estimated ranges. (This figure is reproduced from Ref. [93].)

works as follows: (1) PolY is executed nine times in order to fully polarize the nuclei. (2) A microwave π pulse drives the NV spin into $|m_S = -1\rangle$. (3) An rf π pulse tuned at $f_1 = 215.6$ kHz is applied. The NV spin being $|m_S = -1\rangle$, only the target nuclear spin is resonantly flipped by this rf pulse. (4) By the final PolY, the polarization transfer acts only on the flipped nuclear spin, as other nuclei have already been polarized. The square (□) points in Fig. 4.8 clearly demonstrate the power of selective polarization; dips are observed only at $f_t/3$ and $f_t/5$, with all other dips almost completely disappeared.

4.2.5 Determine unique lattice site of the target ^{13}C spin

We now demonstrate the protocol of Fig. 4.6(g) to determine ϕ. Either PolY or PolX is applied with $N_{pol} = 5$, $N_{rep} = 5$, and $\tau_{pol} = 4.9760$ μs. τ_{pol} satisfies $3/(2\tau_{pol}) = f_t$, for which PolY (PolX) polarizes the target nuclear spin into $m_I = -\frac{1}{2}$ ($\frac{1}{2}$). A phase-controlled

selective rf $\pi/2$ pulse tuned at f_1 is applied, followed by the CP sequence with the $(\pi/2)_{\mathrm{Y}}$ readout ($N = 16$, $\tau = 1.6608$ μs). The rf pulse length is chosen to be 102.041 μs, matched with 22 oscillation periods ($22/f_1$), in order to suppress unwanted phase acquisitions by the rf field along the z axis [see Appendix C]. Figure 4.9(a) shows an exemplary trace as changing t. Here, PolY is used, and the waveform of the rf signal is a sine wave, for which we define the rf phase $\phi_{\mathrm{rf}} = 270°$. The data are fitted by $A\cos(2\pi f_{\mathrm{p}} + \phi_0) + B$ (red curve). f_{p} agrees well with f_1, confirming that the free precession of the target nuclear spin is indeed detected.

We note that the minimum t is set as $t_0 = 6.872$ μs in order to avoid an overlap with an rf pulse, whereas our aim here is to estimate the oscillation phase at $t = 0$. To accurately estimate ϕ_0 under this constraint, oscillations should be taken as long as possible. This requires a dauntingly long measurement time, and at the same time exceedingly high stability of the experimental setup. We therefore choose to undersample the data points for further measurements; by taking less points, t is instead increased up to 1 ms ($< T_1 \approx 5$ ms), and yet the original ϕ_0 is recovered by appropriately setting the measurement parameters [see Appendix C]. Figure 4.9(b) shows ϕ_0 determined in this way. The linear dependence on ϕ_{rf} is observed, as expected [see Appendix C]. ϕ_0 is 180° shifted between PolY and PolX, confirming that the two sequences polarize the nuclear spin into opposite directions. From the fit, we obtain $\phi_0 = \phi_{\mathrm{rf}} + 334.0°$ (mod 360°). On the other hand, if we take into account the azimuthal angle of the rf field in this coordinate and the effect of detuning $(f_p - f_1)$, we can estimate $\phi_{\mathrm{n}}(0)$ as $-\phi_{\mathrm{rf}} + 89.2°$ [see Appendix C]. Together, we obtain ϕ as $243.2 \pm 5.3°$ [dashed line in Fig. 4.9(b)]. $\phi_{\mathrm{n}}(0)$ can be estimated more accurately by simulating the dynamics of the nuclear spin [see Appendix C]. The simulations give $\phi = 248.8 \pm 2.7°$ (dotted line) or $247.8 \pm 4.1°$ (solid line), marginally dependent on the parameters used. Figure 4.9(c) shows the accuracy ranges of ϕ determined by these estimations, and there is at most one lattice site that falls on this range; we have been able to pinpoint the lattice site of the target nuclear spin [see Appendix C].

4.2.6 Conclusion

To summarize, we have described a protocol which tracks a free precession of a single nuclear spin. Combined with DNP and a phase-controlled rf pulse, our method is capable of determining the azimuthal angle of the target nuclear spin. A particular experimental demonstration was performed on a single ^{13}C nuclear spin and its lattice position was uniquely pinpointed. Previously, the position of a single ^{13}C nuclear spin in diamond had been estimated by analyzing NMR spectra taken at three differently oriented $\boldsymbol{B}_0$ [45].

When the NV center or other solid-state defects with $S > \frac{1}{2}$ electron spin is used as a sensor, an application of $\boldsymbol{B}_0$ misaligned from the sensor quantization axis complicates the analysis. The present protocol circumvents this issue. Looking ahead, we imagine that the present protocol could be employed for three-dimensional mapping of nuclear spins in a single molecule positioned on a near-surface NV sensor [123]. The nuclear-nuclear interactions within the immobilized molecule can be suppressed using dipolar decoupling sequences such as WAHUHA and MREV [80,164], which are compatible with our protocol. The protocol can also be combined with the high-resolution spectroscopy method [83–85], so that chemical shifts and J couplings could be resolved. Thus, our result paves the way for magnetic resonance imaging at the single-molecular level.

Chapter 5

Conclusion and outlook

5.1 Conclusion

This thesis has described electron and nuclear spin sensing using nitrogen-vacancy centers in diamond. We have developed measurement protocols for NV-based magnetometry achieving high sensitivity, and high spectrum and spatial resolutions that can not be approached by the conventional sensors.

We have developed a NV characterization setup including a specially designed wide-field microwave antenna for ODMR of NV centers. The antenna's resonance frequency at around zero-field splitting with large bandwidth allows for ODMR at finite magnetic field up to 10 mT and wide range scanning of 1 mm^2 with reasonable spatially uniformity.

We have also demonstrated magnetometry with a novel NV ensemble placed near the diamond surface having a narrow linewidth $\sim$ 200 kHz . Optical dynamic nuclear polarization and pulse sequences were introduced for achieving high sensitivity. Electron spins of paramagnetic impurities, P1 and some other $S = 1/2$ defects, were detected and spectroscopically resolved by the decoherence characterized by Hahn-echo pulse sequence as a function of sweeping magnetic field. This technique would be applicable in the future for detection and imaging of electron spins placed outside of diamond.

Lastly, state-of-the-art AC magnetometry with a single NV center was discussed. The spectrum resolution of 304 μHz, which is high enough to resolve the chemical shift and J coupling in NMR of single molecules, was achieved using the ultrahigh resolution protocol based on time series of dynamical decoupling sequences.

Previously reported state-of-the-art nuclear spin detection using dynamical decoupling and correlation measurements was reproduced successfully using ^{13}C nuclear spins as targets; the approach widely accepted as a testbed for NV-based magnetometry. Experimentally obtained hyperfine parameters were compared with simulations to extract

spin position parameters, such as distance r and tilt angle from magnetic field θ. The remaining parameter, azimuthal angle ϕ, was determined from the phase of free nuclear precession obtained using a newly developed novel protocol in this thesis. The protocol is based on dynamic nuclear polarization combined with phase controlled radio-frequency pulses. As a result, exact lattice sites of the target ^{13}C spins were determined successfully. This protocol would be applicable in the future for nuclear spin position imaging of molecules placed outside of diamond.

5.2 Outlook

The advances shown in this thesis will serve as building blocks for single molecule structure analysis in the future. Recently, Pfender *et al.* successfully obtained hyperfine parameters $A_{\parallel}$ and $A_{\perp}$ from the correlation of nuclear spin precession taken with the ultrahigh resolution sensing scheme [87]. Introduction of the correlation spectroscopy developed in this thesis would improve the precision in the nuclear spin position determination.

The obvious next step is the individual nuclear spin MRI of a molecule using a shallow single NV center. To reach this ultimate goal, not only sufficient detection sensitivity, but also the spectrum resolution are needed. Moreover, reliable methods to place a target molecule at the surface right above a shallow NV needs to be developed.

As stated in the abstract, NV is capable of sensing many physical parameters of the ambient such as electric fields [40] and temperatures [34, 108, 109, 165]. The electron and nuclear spin sensing protocols developed in this thesis are expected to serve in a variety of future applications. Recent sensing applications of NVs include thermometry in living cells [110, 166], magnetic imaging of a living magnetostactic bacteria [111, 121] and cells [167], measurements of action potentials of single neuron [168], magnetic imaging of meteorites [112], detection of superconducting Meissner effects [169–178], imaging of electric current flows [179–184], imaging of nanoscale magnetic domain structures [185–192], detection of noises in metal films [193, 194] and superparamagnetic nanoparticles [127], detection of ferromagnetic resonances [195–198], detection of spinwaves [199], detection of propagating spin waves [200, 201], probing nuclear dynamics in two dimensional materials [202], and spin resonance detection at the single spin/molecule level [41, 51, 52, 79, 203–205] (See review articles [95, 96, 150, 206–212]). There also exists a proposal to utilize NV sensors for detection of dark-matter [213]. Diamonds are forever.

Appendix A

Supplementary materials for Sec. 2.1

Here we derive the relation between magnetic field and NV's resonance frequencies. The matrix formula of the Hamiltonian shown in Eq. (2.1) is rewritten as,

$$\hat{H} = \begin{pmatrix} D+\gamma_e B_0 \cos\beta & \gamma_e B_0 \sin\beta/\sqrt{2} & 0 \\ \gamma_e B_0 \sin\beta/\sqrt{2} & 0 & \gamma_e B_0 \sin\beta/\sqrt{2} \\ 0 & \gamma_e B_0 \sin\beta/\sqrt{2} & D-\gamma_e B_0 \cos\beta \end{pmatrix}, \quad \text{(A.1)}$$

where B_0 is magnetic field strength and β is tilt angle between NV-axis and magnetic field. Here we restrict magnetic field tilt for x direction. It is allowed for calculating resonance frequencies because NV Hamiltonian is axisymmetric. The eigenvalue λ is calculated as,

$$\det(\hat{H}-\lambda\mathbf{1}) = -\lambda^3 + 2D\lambda^2 + (\gamma_e^2 B_0^2 - D^2)\lambda - D\gamma_e^2 B_0^2 \sin^2\beta = 0, \quad \text{(A.2)}$$

where $\mathbf{1}$ is identity matrix. The eigenvalues corresponding to the energies of the $m_S = 0$, -1, and $+1$ states are represented by λ_0, λ_-, and λ_+, respectively. The resonance frequencies are obtained as $f_+ = \lambda_+ - \lambda_0$ and $f_- = \lambda_- - \lambda_0$.

By taking the difference between the middle part of Eq. (A.2) substituting λ_+ and λ_0 for λ, we get

$$-3(f_+ + 2\lambda_0)^2 + 8D(f_+ + 2\lambda_0) + 4(\gamma_e^2 B_0^2 - D^2) - f_+^2 = 0. \quad \text{(A.3)}$$

Here we use a relation $(\lambda_+^3 - \lambda_0^3)/(\lambda_+ - \lambda_0) = \frac{(\lambda_+ - \lambda_0)^2 + 3(\lambda_+ + \lambda_0)^2}{4}$. Similarly, using λ_- instead of λ_+, we get

$$-3(f_- + 2\lambda_0)^2 + 8D(f_- + 2\lambda_0) + 4(\gamma_e^2 B_0^2 - D^2) - f_-^2 = 0. \quad \text{(A.4)}$$

Using the difference between the left parts of Eq. (A.3) and Eq. (A.4), λ_0 is extracted as

$$\lambda_0 = (-f_+ - f_- + 2D)/3. \quad \text{(A.5)}$$

The all eigenvalues are thus described using f_- and f_+ as $\lambda_- = (-f_+ + 2f_- + 2D)/3$ and $\lambda_+ = (2f_+ - f_- + 2D)/3$.

Using Eq. (A.3) and Eq. (A.5), magnetic field strength is extracted as,

$$B_0 = \frac{1}{\gamma_e}\sqrt{\frac{f_+^2 + f_-^2 - f_+ f_- - D^2}{3}}. \tag{A.6}$$

Using Eq. (A.2), Eq. (A.5) and Eq. (A.6), the tilt angle is extracted as,

$$\beta = \arcsin\left(\sqrt{\frac{-\lambda_0^3 + 2D\lambda_0^2 + (\gamma_e^2 B_0^2 - D^2)\lambda_0}{D\gamma_e^2 B_0^2}}\right). \tag{A.7}$$

Appendix B

Supplementary materials for Chap. 3

In this Appendix, we discuss the feasibility of decoherence spectroscopy in detecting *external* spins. In Chap. 3, we used Eq. (3.3) in order to estimate the instantaneous diffusion of the sensor spins caused by the *internal* target spins (P1 centers). Equation (3.3) is derived by evaluating the dipolar interaction between the sensor and target spins. Both target and sensor spins are treated as ensembles, and therefore, the integration over the entire volume is taken; In the polar coordinates (r, θ, ϕ), this procedure is explicitly written as

$$N \int_0^{2\pi} d\phi \int_0^{\pi} d\theta \int_0^{\infty} dr \cdot r^2 \sin\theta \left[1 - \cos\left(\frac{\mu_0}{4\pi} \frac{g^2 \mu_B^2}{\hbar} \times \frac{3\cos^2\theta - 1}{r^3} \right) \right] = 2\pi \frac{\pi \mu_0 g^2 \mu_B^2}{9\sqrt{3}\hbar} N, \tag{B.1}$$

yielding Eq. (3.3) for $\beta = \pi$. We estimate the effect of external spins with the density of $N_{\rm ext}$ by changing the integration range. Moving to the cylindrical coordinates (R, ϕ, z), we rewrite the integral as

$$N_{\rm ext} \int_0^{2\pi} d\phi \int_{d_{\rm NV}}^{\infty} dz \int_0^{\infty} dR \cdot R \left[1 - \cos\left(\frac{\mu_0}{4\pi} \frac{g^2 \mu_B^2}{\hbar} \tau \left\{ \frac{3z^2}{R^2 + z^2} - 1 \right) \frac{1}{(R^2 + z^2)^{\frac{3}{2}}} \right\} \right] \tag{B.2}$$

Here, the origin is taken at the NV center located $d_{\rm NV}$ beneath the surface. For simplicity, the static magnetic field is applied perpendicular to the surface. When a large (compared with the imaging resolution) specimen is placed on the surface, we may restrict the integration to $z > d_{\rm NV}$ (outside of diamond). For the surface NV layer with the thickness of $t_{\rm NV}$, the instantaneous diffusion time $T_{\rm id}$ is estimated by superposing the contributions from the NV spins residing in $d_{\rm NV} \leq t_{\rm NV}$. Figure B.1 shows the result of numerically calculated $(T_{\rm id})^{-1}$ for various $t_{\rm NV}$ and $N_{\rm ext}$. These values correspond to the changes in $(T_2)^{-1}$ from the baseline decoherence rate $(T_2^{\rm base})^{-1}$. $(T_{\rm id})^{-1}$ decreases as increasing $t_{\rm NV}$ because the deeper NV spins decay only slightly within the timescale of

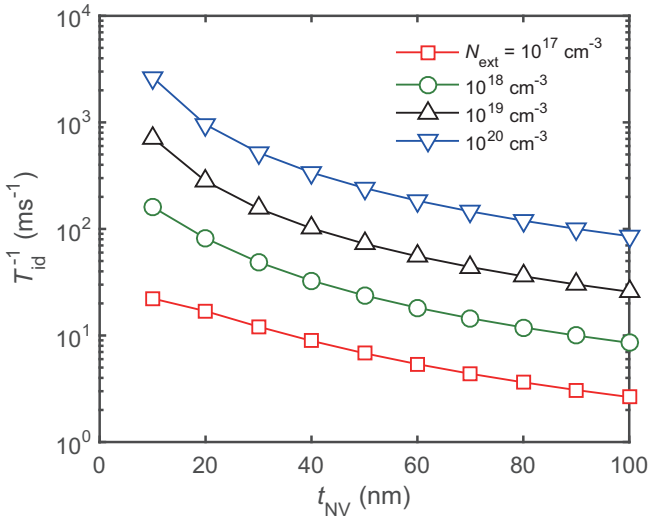

Figure B.1: Numerically calculated $T_{\rm id}^{-1}$ caused by external spins as a function of the NV layer thickness $t_{\rm NV}$ and the external spin density $N_{\rm ext}$.

$T_{\rm id}$ of the shallower NV spins. When these signals are superposed, the total $T_{\rm id}$ becomes longer. Nonethelss, we observe that, with the current NV layer thickness of 100 nm and $N_{\rm ext} = 10^{18}$ cm^{-3}, $(T_2)^{-1}$ will change by more than 10 ms^{-1}, which is detectable with decoherence spectroscopy. While we still expect a finite change in T_2 for $N_{\rm ext} = 10^{17}$ cm^{-3} this concentration is comparable with the density of internal spins in the present sample and decoherence spectroscopy thus will be less sensitive. However, we emphasize that this is not a fundamental limit. As discussed in above and Ref. [135], there is much room for improvement in future sensors; Reducing the residual P1 density leads to narrower NV linewidths, and allows to use a thinner NV layer ($t_{\rm NV} \ll 100$ nm) while keeping the DC magnetic field sensitivity. Such improvement will also ensure decoherence spectroscopy on $N_{\rm ext} = 10^{17}$ cm^{-3}.

Finally, we remark on the effect of the T_1 relaxation of target spins on decoherence spectroscopy. Although the effect of T_1 can in principle be incorporated into the analysis of decoherence spectroscopy, it is desired that T_1 of the target spins is long compared with the timescale of decoherence spectroscopy ($\sim T_2$ of the sensor spins) so that the target spins do not introduce additional decoherence on the sensor spins. In the case of the P1 spins, long T_1 (order of ms) has caused little complication in the analysis. On the other hand, radicals in organic molecules or proteins, which are candidates for external spins in future experiments, may have shorter T_1, depending on their respective environments.

While it is difficult to discuss T_1 of these materials from a general perspective, a tendency is that T_1 becomes longer as decreasing the spin density and lowing temperatures. For instance, electron spins of diphenylpicrylhydrazyl (DPPH) in polystyrene have $T_1 = 6.7$ μs for $\sim 10^{20}$ cm^{-3} at 300 K, $T_1 = 65$ μs for $\sim 10^{17}$ cm^{-3} and $T_1 = 1.2$ ms for $\sim 10^{17}$ cm^{-3} at 100 K [214]. These values indicate that Next of 10^{17} cm^{-3} is an appropriate regime to carry out decoherence spectroscopy, and is in line with the target regime of our future sensors.

Appendix C

Supplementary materials for Sec. 4.2

C.1 Definition of coordinates

In Sec. 4.2, the Cartesian coordinate depicted in Fig. C.1(a) was adopted. The x, y, and z axes of this coordinate are parallel to the $[\bar{1}\bar{1}\bar{2}]$, $[1\bar{1}0]$, and $[\bar{1}\bar{1}1]$ crystallographic directions of diamond, respectively. Since a single nitrogen-vacancy (NV) center with its symmetry axis parallel to the $[\bar{1}\bar{1}1]$ direction was used as a quantum sensor and the static external magnetic field B_0 was applied along the same direction, this coordinate is suitable to discuss the position of the target nucleus with respect to that of the sensor, and is henceforth termed as "sensor coordinate". The spherical coordinate parameters (r, θ, ϕ) with the distance r (≥ 0), the polar angle θ ($0 \leq \theta \leq \pi$), and the azimuthal angle ϕ ($0 \leq \phi \leq 2\pi$) are used to specify the position of the target nucleus.

The origin is taken at an approximate "center of mass" of the NV center, where the NV spin is regarded as a point dipole. It resides in the crossing point of the NV symmetry axis and the plane spanned by the three carbon atoms adjacent to the vacancy, or in other

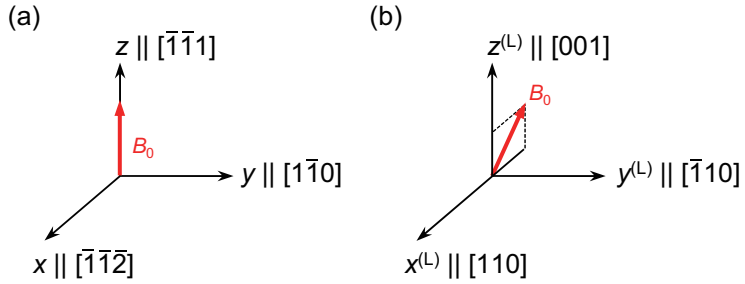

Figure C.1: (a) Sensor coordinate. (b) Laboratory coordinate.

words, 0.75 Å above the vacancy site. It is assumed that the vacancy site locates above the nitrogen site. The motivation of this definition is that the direction of $A_\perp$ is conditional on θ and changes a sign at $\theta = \frac{\pi}{2}$ [Eq. (C.10) in Sec. C.3], and that the target nuclear spin we measured lies coincidentally in the plane including the vacancy. It is generally accepted that the "center of mass" of the NV center lies above the vacancy, even though the precise position has not been determined. For analysis of ϕ of the target nuclear spin, we take the direction of $A_\perp$ inward. Our definition gives θ of the target spin as 94.8°, so that it is consistent with Eq. (C.10).

Here, we introduce "laboratory coordinate", the second coordinate that is to be used in this Appendix C. The sensor coordinate and the laboratory coordinate are readily transformed each other, and the purpose of using two coordinates is purely for convenience sake. The laboratory coordinate is depicted in Fig. C.1(b). The $x^{(\mathrm{L})}$, $y^{(\mathrm{L})}$, and $z^{(\mathrm{L})}$ axes are parallel to the [110], [$\bar{1}$10], and [001] crystallographic directions, respectively. Because of the configuration of our experimental setup [Fig. C.2(a)], this coordinate is suitable to discuss the direction of the magnetic field generated by a coil bonded on the back side of the sample mount (Sec. C.2). The following matrix transforms a vector $a^{(\mathrm{L})}$ defined in the laboratory coordinate into a vector $a^{(\mathrm{S})}$ in the sensor coordinate:

$$T^{(\mathrm{L}\to\mathrm{S})} = R_y(-\Theta_0^{(\mathrm{L})})R_z(-\Phi_0^{(\mathrm{L})}), \tag{C.1}$$

where $\Theta_0^{(\mathrm{L})} = 54.7°$ and $\Phi_0^{(\mathrm{L})} = 180°$ and the polar and azimuthal angles of $\boldsymbol{B}_0$ as seen in the laboratory coordinate, respectively. $R_y(\Theta)$ and $R_z(\Phi)$ are the rotation matrices defined as,

$$R_y(-\Theta) = \begin{pmatrix} \cos\Theta & 0 & \sin\Theta \\ 0 & 1 & 0 \\ -\sin\Theta & 0 & \cos\Theta \end{pmatrix} \text{ and } R_z(-\Phi) = \begin{pmatrix} \cos\Phi & -\sin\Phi & 0 \\ \sin\Phi & \cos\Phi & 0 \\ 0 & 0 & 1 \end{pmatrix}. \tag{C.2}$$

C.2 Experimental setup

C.2.1 Electronics

As described in Sec. 4.2, a single NV center in a type-IIa (001) diamond was measured by a home-built confocal microscope. We here focus on the electronics aspect of our setup, which is schematically shown in Fig. C.2(b). Microwave pulses are generated by a vector signal generator (VSG, Stanford Research Systems SG396), amplified by a high-power broadband amplifier (Mini-Circuits ZHL-16W-43+), and delivered to the NV center through a copper wire running across the diamond surface [Fig. C.2(a)]. An arbitrary waveform generator (AWG, Tektronix AWG7122C) provides IQ signals to the VSG. RF

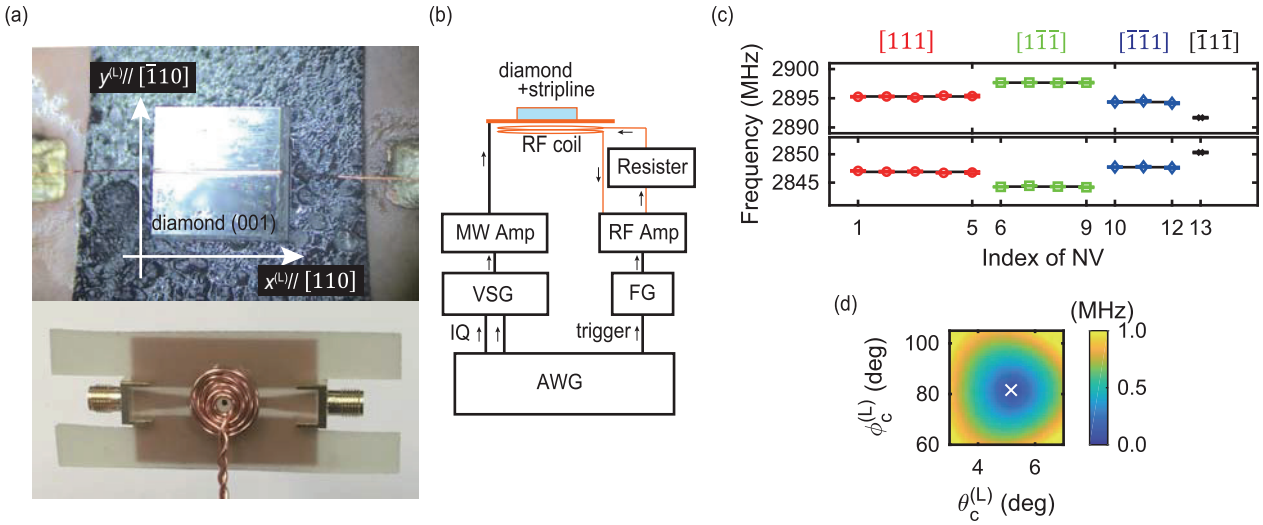

Figure C.2: (a) Front and back sides of the sample mount (PCB board) with a diamond sample, a copper wire, and a coil. (b) Schematic of electronics. AWG: arbitrary waveform generator, VSG: vector signal generator, FG: function generator. (c) Resonance frequencies of single NV centers found in a $80 \times 80 \times 10$ μm^3 volume. The black lines indicate the average resonance frequencies of the NV centers having the same symmetry axis. (d) Determination of the direction of B_c. The fit errors are minimized at $(\theta_c^{(L)}, \phi_c^{(L)}) = (5.2°, 81.6°)$.

pulses are triggered by the same AWG. Waveforms generated by a function generator (FG, NF WF1973) and amplified by a low-impedance amplifier (Accel Instruments TS200-HF) are sent to a hand-wound coil bonded on the back side of the sample mount [Fig. C.2(a)]. This coil has an inductance L_c of 3.5 μH and a resistance R_c of 0.3 Ω. A low-impedance-high-power resister ($R = 4.7\ \Omega$) is series-connected to the coil. By this resistor, the rising time is reduced down to $L_c = (R + R_c) = 0.7\ \mu$s, allowing us to generate RF signals at several hundreds of kHz.

C.2.2 Magnetic fields generated by the coil

To calibrate the direction of the magnetic fields generated by the coil, we conduct vector DC magnetometry using multiple single NV centers. We optically resolve single NV centers in a $80 \times 80 \times 10\ \mu\text{m}^3$ scan volume within diamond, and apply DC voltages on the coil to generate the DC magnetic field $\boldsymbol{B}_c$. Note that this $\boldsymbol{B}_c$ is different from $\boldsymbol{B}_0$. The latter was supplied using a permanent magnet, and in the present measurement, the magnet was removed ($B_0 = 0$ mT). The spin resonance frequencies of 13 single NV centers under $\boldsymbol{B}_c$ are plotted in Fig. C.2(c). Among the NV centers having the same symmetry axis, the deviation from the averaged resonance frequency [solid lines in Fig. C.2(c)] is found to be less than 0.1 kHz, certifying high homogeneity of $\boldsymbol{B}_c$ within the observed volume. The resonance frequencies of the ith NV center are calculated from the spin Hamiltonian

$$\hat{H}^{(j)} = D(\hat{S}_z^{(j)})^2 + \gamma_e \boldsymbol{B}_c \cdot \hat{\boldsymbol{S}}^{(j)}, \tag{C.3}$$

where D is the zero-field splitting, $\gamma_e = 28$ MHz/mT is the gyromagnetic ratio of the electron, and $S^{(i)}$ is the $S = 1$ spin operator with its quantization axis taken as the symmetry axis of the ith NV center. The direction and strength of $\boldsymbol{B}_c$ are determined by minimizing the errors between the observed and calculated resonance frequencies [Fig. C.2(d)]. As a result, we obtain $D = 2870.4$ MHz, $\boldsymbol{B}_c = 1.47$ mT, $\theta_c^{(L)} = 5.2°$, and $\phi_c^{(L)} = 81.6°$, where $\theta_c^{(L)}$ and $\phi_c^{(L)}$ are the polar and azimuthal angles of Bc as seen in the laboratory coordinate. In the sensor coordinate, these angles are given by $\theta_c = 55.7°$ and $\phi_c = 186.2°$.

C.2.3 Delay time in the RF electronics

The presence of an unknown delay directly affects the accuracy of the estimation of ϕ. For instance, at $f_1 = 215.6$ kHz used in our experiments, the delay of 13 ns amounts to the angle difference of $-1°$. The sources of the delay include trigger jitters in the AWG and the FG, the electrical length of the coaxial cables, the time constant of the LC circuit, and so on. Some of them can be characterized independently, but the total delay *at the*

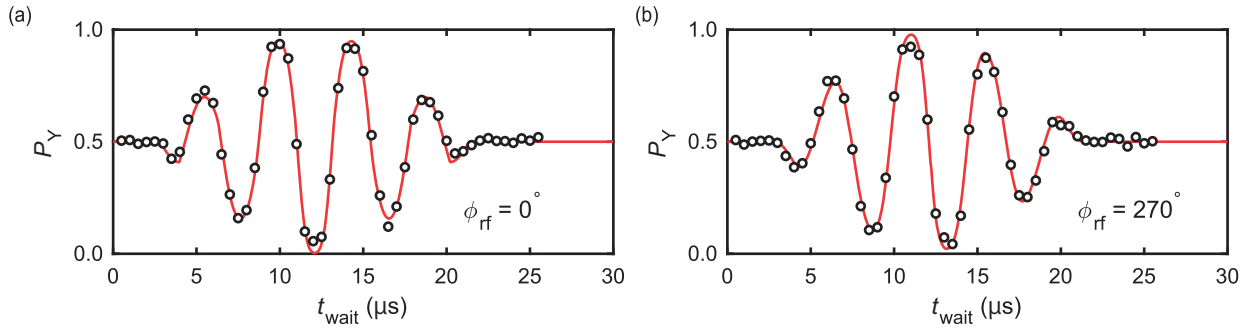

Figure C.3: AC sensing for (a) $\phi_{\rm rf} = 0°$ and (b) $\phi_{\rm rf} = 270°$.

position of the NV center, $t_{\rm delay}$ can only be measured using the NV center itself. For this purpose, we use a waveform

$$W(t) = \begin{cases} V_{\rm pp} \cos\left[2\pi f_1 (t - \tau_0) + \phi_{\rm rf}\right] & \text{for } \tau_0 \leq t \leq \tau_0 + 4\tau \\ 0 & \text{otherwise,} \end{cases} \tag{C.4}$$

with $V_{\rm pp} = 10$ mV, $\tau_0 = 11$ μs, $\tau = 2.319$ μs $= (2f_1)^{-1}$, and $\phi_{\rm rf} = 0°$ or $270°$. The coil receives an amplified waveform $t_{\rm delay}$ seconds after the trigger of the AWG. At the same time, the CP sequence with $N = 4$ and $\tau = 2.319$ μs, starting $t_{\rm wait}$ seconds after the trigger, detects this AC field. When read out by the $(\pi/2)_{\rm Y}$ pulse, the transition probability is given by [84]

$$\hat{P}_{\rm Y} = \frac{1}{2}(1 - \sin\psi), \tag{C.5}$$

with

$$\psi = \frac{\gamma_{\rm e} b_{\rm rf}}{V_{\rm pp}} \int W(t - t_{\rm delay}) y(t - t_{\rm wait}) dt, \tag{C.6}$$

$b_{\rm rf}$ is the AC signal amplitude at the position of the NV center, and $y(t)$ is the modulation function

$$y(t) = \begin{cases} 1 & \text{for } 0 \leq t < \frac{\tau}{2}, \frac{3\tau}{2} \leq t < \frac{5\tau}{2}, \frac{7\tau}{2} \leq t < 4\tau \\ -1 & \text{for } \frac{\tau}{2} \leq t < \frac{3\tau}{2}, \frac{5\tau}{2} \leq t < \frac{7\tau}{2} \\ 0 & \text{otherwise.} \end{cases} \tag{C.7}$$

Equation (C.6) means that the accumulated phase ψ is a convolution of a signal wave with delay $t_{\rm delay}$ and a "sensing window" of the CP sequence. When the timing of the CP

sequence matches with that of the signal wave, $P_{\rm Y}$ is modified accordingly. Therefore, by sweeping $t_{\rm wait}$, we can estimate $t_{\rm wait}$. Figure C.3 shows $P_{\rm Y}$ as a function of $t_{\rm wait}$ for $\phi_{\rm rf} = 0°$ (a) and 270° (b). The data is fitted by Eq. (C.5), and we extract $t_{\rm delay} = 1.088 \pm 0.003$ μs. The error of ± 3 ns corresponds to only $\pm 0.2°$.

C.2.4 Chirped pulse

In our experiments based on the pulse sequences shown in Fig. 4.6 of Sec. 4.2, single photons emitted from the NV center are counted by a single-photon counting module (Laser Components COUNT-10C). These events are indicated as *Readout* in Fig. 4.6 of Sec. 4.2. The recorded photon counts are converted into the "transition probabilities" (Sec. C.3). For accurate conversion, calibration of the photon counts marking $|m_S = 0\rangle$ to $|m_S = -1\rangle$ is crucial. To robustly flip the NV spin from laser-initialized $|m_S = 0\rangle$ to $|m_S = -1\rangle$, we use a chirped microwave pulse known as WURST (wideband, uniform rate, smooth truncation) [148, 149]. The amplitude modulation of WURST is given by

$$1 - \left| \cos\left(\frac{\pi t}{t_{\rm p}}\right) \right|^{\alpha_{\rm p}}, \tag{C.8}$$

where $t_{\rm p}$ is the pulse length and $\alpha_{\rm p}$ characterizes the envelope shape. We set $t_{\rm p} = 2$ μs and $\alpha_{\rm p} = 2$, and sweep the microwave frequency from -10 to 10 MHz around the resonance frequency during the pulse. The pulse shaping and frequency modulation are done by the AWG. Prior to the respective pulse sequences, we record the reference photon counts with and without a chirped pulse.

A chirped pulse is also used in the protocol of Fig. 4.6(g) of Sec. 4.2, when the NV spin is prepared in $|m_S = -1\rangle$ before applying an RF $\pi/2$ pulse (Sec. C.8). Note that microwave pulses in the CP and PulsePol sequences are not chirped.

C.3 Dynamics of a single nuclear spin under the CP sequence

Here, we derive Eqs. (4.26) and (4.26) of Sec. 4.2, closely following the descriptions in [44] and [71]. In the sensor coordinate, the spin Hamiltonian of the NV-^{13}C-coupled system is given by

$$H \;=\; DS_z^2 + \gamma_{\rm e} B_0 S_z - \gamma_{\rm c} B_0 I_z + S_z(A_\perp \boldsymbol{e}_\perp \cdot \boldsymbol{I} + A_\parallel I_z). \tag{C.9}$$

The target ^{13}C nuclear spin is located at $(r,\, \theta,\, \phi)$. $\boldsymbol{e}_\perp$ is given by

$$\boldsymbol{e}_\perp \;=\; \begin{cases} \cos\phi \boldsymbol{e}_x + \sin\phi \boldsymbol{e}_y & \text{for } 0 \le \theta < \frac{\pi}{2} \\ -\cos\phi \boldsymbol{e}_x - \sin\phi \boldsymbol{e}_y & \text{for } \frac{\pi}{2} \le \theta \le \pi. \end{cases} \tag{C.10}$$

The direction of $A_\perp$ is conditional on θ; when the nuclear spin locates above (below) the sensor spin, $A_\perp$ points outward (inward) because $A_\perp \propto 3\cos\theta\sin\theta/r^3$ in a dipolarly-coupled system. Figure 4.6(a) of Sec. 4.2 depicts the case for $0 \le \theta \le \frac{\pi}{2}$. The operator $\boldsymbol{e}_\perp \cdot \boldsymbol{I}$ can be simplified as I_x by an appropriate unitary transformation (a rotation about the z axis), so that the eigenenergies of Eq. (C.9) are independent of ϕ. However, we keep this form in order to examine how the real-space position of the ^{13}C nuclear spin is reflected in its dynamics.

In our experiments, $|m_S = 0\rangle$ and $|m_S = -1\rangle$of the NV spin, separated by $D - \gamma_\mathrm{e} B_0 = 1.8582$ GHz, are used as $|0\rangle$ and $|1\rangle$ of the sensor, respectively. (Strictly speaking, ^{14}N isotope of the NV center has a nuclear spin $I = 1$, and the $m_I = 1$ state we used has the transition frequency 2 MHz higher than $D - \gamma_\mathrm{e} B_0$, due to the NV-^{14}N hyperfine interaction. In addition, the ^{14}N nuclear spin is polarized into the $m_I = 1$ state by optical hyperpolarization [150]. Other nuclear sublevels thus do not play any roles in the present work, and are not considered below.) We move to the rotating frame of the NV spin and rewrite Eq. (C.9) as

$$H_\mathrm{r} \;=\; -\gamma_\mathrm{c} B_0 I_z + S_z (A_\perp \boldsymbol{e}_\perp \cdot \boldsymbol{I} + A_\parallel I_z). \tag{C.11}$$

Note that the nuclear spin stays in the original sensor coordinate. When the NV spin is $|m_S = 0\rangle$, H_r is reduced to

$$H_0 \;=\; -\gamma_\mathrm{c} B_0 I_z = -f_0 I_z. \tag{C.12}$$

For $|m_S = -1\rangle$, we obtain

$$H_1 \;=\; -f_0 I_z - (A_\perp \boldsymbol{e}_\perp \cdot \boldsymbol{I} + A_\parallel I_z) = -f_1 \boldsymbol{e}_\mathrm{p} \cdot \boldsymbol{I}, \tag{C.13}$$

with

$$f_1 \;=\; \sqrt{(f_0 + A_\parallel)^2 + A_\perp^2} \tag{C.14}$$

$$\boldsymbol{e}_p \;=\; \frac{f_0 + A_\parallel}{f_1} \boldsymbol{e}_z + \frac{A_\perp}{f_1} \boldsymbol{e}_\perp = \cos\theta_\mathrm{p} \boldsymbol{e}_z + \sin\theta_\mathrm{p} \boldsymbol{e}_\perp. \tag{C.15}$$

In our experiments, the polar angle is calculated as $\theta_\mathrm{p} = \arctan\left[A_\perp/(f_0 + A_\parallel)\right] = 5.9^\circ$. In the protocol of Fig. 4.6(g) of Sec. 4.2, the nuclear spin is driven by an RF field while

the sensor is $|m_S = -1\rangle$. Therefore, $\boldsymbol{e}_{\rm p}$ is the precession axis of the target nuclear spin (hence the suffix "p"). We detail this point in Sec. C.8.

We now examine the dynamics of a single nuclear spin under the CP sequence by calculating the transition prob-abilities, which are the probabilities that, at the end of the CP sequence, the NV spin is found to be in the state opposite to the state right before the application of the first $(\pi/2)_{\rm X}$ pulse. In our experiments, both $|m_S = 0\rangle$ and $|m_S = -1\rangle$ are used as the initial state of the CP sequence, but the expressions of the transition probabilities obtained below [Eqs. (C.25) and (C.26)] do not depend on the initial state. We assume that the sensor is initialized to $|m_S = 0\rangle$ with its pure state density matrix given by $|m_S = 0\rangle \langle m_S = 0|$. We also introduce a density matrix of the nuclear spin as

$$\rho_{\rm n} = \frac{1}{2}\mathbf{1} + \boldsymbol{\nu}_{\rm n} \cdot \boldsymbol{I}, \tag{C.16}$$

where $\boldsymbol{\nu}_{\rm n}$ is the Bloch vector of the nuclear spin defined in the sensor coordinate. Again, we assume that the nuclear spin is in the pure state, which is relevant because the nuclear spin is polarized in our protocol, and the coherence time of the nuclear spin is long. Therefore, $\boldsymbol{\nu}_{\rm n}$ is parametrized by $(\theta_{\rm n}, \phi_{\rm n})$. Note that both $\theta_{\rm n}$ and $\phi_{\rm n}$ are time-dependent in the sensor coordinate. The density matrix of an uncoupled NV-^{13}C system is written as

$$\rho_0 = |0\rangle \langle 0| \otimes \rho_{\rm n}. \tag{C.17}$$

The $(\pi/2)_{\rm X}$ pulse is applied first to create a superposition of $|0\rangle$ and $|1\rangle$, which couple with the nuclear spin differently. The unitary operator for the $(\pi/2)_{\rm X}$ pulse is given as

$$U_{\rm X} = \frac{1}{\sqrt{2}}(|0\rangle \langle 0| + |1\rangle \langle 1| - i\,|1\rangle \langle 0| - i\,|0\rangle \langle 1|). \tag{C.18}$$

The evolution of the nuclear spin during the CP sequence is described as

$$U_{\rm cp} = (U_0 U_1^2 U_0)^{\frac{N}{2}} |0\rangle \langle 0| + (U_1 U_0^2 U_1)^{\frac{N}{2}} |1\rangle \langle 1| \tag{C.19}$$

with

$$U_0 = e^{-2\pi i H_0 \frac{\tau}{2}} = e^{i\pi f_0 \tau I_z} = e^{i\alpha I_z} \tag{C.20}$$

$$U_1 = e^{-2\pi i H_1 \frac{\tau}{2}} = e^{i\pi f_1 \tau \boldsymbol{e}_{\rm p}\cdot\boldsymbol{I}} = e^{i\beta \boldsymbol{e}_{\rm p}\cdot\boldsymbol{I}}. \tag{C.21}$$

By noting that any unitary evolution of a single spin can be described as a rotation around a certain axis, we can rewrite Eq. (C.19) as

$$U_{\rm cp} = e^{-iN\phi_{\rm cp}\boldsymbol{n}_0\cdot\boldsymbol{I}} |0\rangle \langle 0| + e^{-iN\phi_{\rm cp}\boldsymbol{n}_1\cdot\boldsymbol{I}} |1\rangle \langle 1|, \tag{C.22}$$

where $\boldsymbol{n}_0$ and $\boldsymbol{n}_1$ define the rotation axes of the respective unitary operations, and $N\phi_{\rm cp}$ is the rotation angle. From straightforward calculations, we obtain $\phi_{\rm cp}$ as

$$\cos\phi_{\rm cp} \;=\; \cos\alpha\cos\beta - \cos\theta_{\rm p}\sin\alpha\sin\beta. \tag{C.23}$$

with $\alpha = \pi f_0\tau$ and $\beta = \pi f_1\tau$ [as defined by Eqs. (C.20) and (C.21)]. For later convenience, we also give an explicit form of $\boldsymbol{n}_0$:

$$\boldsymbol{n}_0 \;=\; -\frac{\sin\theta_{\rm p}\sin\beta}{\sin\theta_{\rm cp}}\boldsymbol{e}_\perp - \frac{\sin\alpha\cos\beta+\cos\theta_{\rm p}\cos\alpha\sin\beta}{\sin\theta_{\rm cp}}\boldsymbol{e}_z. \tag{C.24}$$

The transition probability with the $(\pi/2)_{\rm X}$ readout pulse is calculated as

$$P_{\rm X} \;=\; {\rm Tr}\left[(S_z^2)U_{\rm X}U_{\rm cp}U_{\rm X}\rho_0 U_{\rm X}^\dagger U_{\rm cp}^\dagger U_{\rm X}^\dagger\right] = 1-\frac{1}{2}(1-\boldsymbol{n}_0\cdot\boldsymbol{n}_1)\sin^2\frac{N\phi_{\rm cp}}{2}. \tag{C.25}$$

This is Eq. (4.26) of Sec. 4.2. When the $(\pi/2)_{\rm Y}$ pulse is used, the transition probability becomes

$$\begin{aligned} P_{\rm Y} \;&=\; {\rm Tr}\left[(S_z^2)U_{\rm Y}U_{\rm cp}U_{\rm X}\rho_0 U_{\rm X}^\dagger U_{\rm cp}^\dagger U_{\rm Y}^\dagger\right] \\ &=\; \frac{1}{2}-\frac{1}{4}\boldsymbol{\nu}_{\rm n}\cdot\left\{(\boldsymbol{n}_0-\boldsymbol{n}_1)\sin(N\phi_{\rm cp})+2(\boldsymbol{n}_0\times\boldsymbol{n}_1)\sin^2\frac{N\phi_{\rm cp}}{2}\right\}. \end{aligned} \tag{C.26}$$

$U_{\rm Y}$, the unitary operator for the $(\pi/2)_{\rm Y}$ pulse, is given as

$$U_{\rm Y} \;=\; \frac{1}{\sqrt{2}}(|0\rangle\langle 0| + |1\rangle\langle 1| + |1\rangle\langle 0| - |0\rangle\langle 1|). \tag{C.27}$$

Up to this point, calculations are rigorous and general. We now consider a situation appropriate to our experiments. Both $P_{\rm X}$ and $P_{\rm Y}$ are strongly modulated when $\boldsymbol{n}_0$ and $\boldsymbol{n}_1$ are anti-parallel i.e., $\boldsymbol{n}_0\cdot\boldsymbol{n}_1 = -1$. This also means $\boldsymbol{n}_1 = -\boldsymbol{n}_0$ and $\boldsymbol{n}_0+\boldsymbol{n}_1 = 0$. Equation (C.26) is simplified as

$$P_{\rm Y} = \frac{1}{2}+\frac{1}{2}\boldsymbol{\nu}_{\rm n}\cdot\boldsymbol{n}_0\sin(N\phi_{\rm cp}). \tag{C.28}$$

In the high-field regime ($f_0 >> A_\parallel, A_\perp$), the condition $\boldsymbol{n}_0\cdot\boldsymbol{n}_1 = -1$ is realized, for instance, by choosing τ such that [44]

$$2\tau \approx \frac{1}{f_0 + A_\parallel/2} \approx 1/f_{\rm t}, \tag{C.29}$$

which is also the setting of our protocol. In this case, we evaluate $\alpha \approx \frac{\pi f_0}{2f_0+A_\parallel} \approx \frac{\pi}{2}$, $\beta \approx \frac{\pi f_1}{2f_0+A_\parallel} \approx \frac{\pi}{2}$, and $\cos\theta_{\rm p} = 1$. From Eq. (C.23), we obtain $\cos\phi_{\rm cp} \approx cos\theta_{\rm p} \approx -1$, and hence $\phi_{\rm cp} \approx \pi$. It should be noted that we can assume either $\phi_{\rm cp} > \pi$ or $\phi_{\rm cp} < \pi$ [71]. This arbitrariness affects the directions of $\boldsymbol{n}_{0,1}$ and a sign of $\sin(N\phi_{\rm cp})$, but does not affect the

final results, because $U_{\rm cp}$ is identical in both cases. We set $\phi_{\rm cp} \approx \pi - \theta_{\rm p} < \pi$. In this case, for sufficiently small and even N, $\sin(N\phi_{\rm cp}) < 0$. From Eq. (C.24), and by noting $(\sin\theta_{\rm p}/\sin\phi_{\rm cp} \approx 1)$, we obtain $\boldsymbol{n}_0 \approx \boldsymbol{e}_\perp$. Moreover, after the application of the RF $\pi/2$ pulse, the nuclear spin is also in the xy plane ($\theta_{\rm n} = \pi/2$). Equation (C.28) becomes

$$P_{\rm Y} = \begin{cases} \frac{1}{2} - \frac{1}{2}\cos(\phi - \phi_{\rm n})\sin(N\phi_{\rm cp}) & \text{for } 0 \le \theta < \frac{\pi}{2} \\ \frac{1}{2} - \frac{1}{2}\cos(\phi - \phi_{\rm n} + \pi)\sin(N\phi_{\rm cp}) & \text{for } \frac{\pi}{2} \le \theta \le \pi. \end{cases} \tag{C.30}$$

which is Eq. (4.27) of Sec. 4.2.

C.4 Estimation of hyperfine parameters

From Eqs. (C.14) and (C.23), we obtain

$$A_\parallel = \frac{\cos\alpha\cos\beta - \cos(\pi - 2\pi f_{\rm cp}\tau)}{\sin\alpha\sin\beta} f_1 - f_1 \tag{C.31}$$

$$A_\perp = \sqrt{f_1^2 - (f_0 + A_\parallel)^2}. \tag{C.32}$$

$f_{\rm cp}$ was determined in Fig. 4.6(b) of Sec. 4.2. We relate $f_{\rm cp}$ and $\phi_{\rm cp}$ as $\phi_{\rm cp} = \pi - 2\pi f_{\rm cp}\tau$. f_0 and f_1 were determined in Fig. 4.7(c) of Sec. 4.2. Substituting $f_{\rm cp} = 10.2$ kHz, $f_0 = 387.5$ kHz, and $f_1 = 215.6$ kHz, and $\tau = 1.6875$ μs into Eqs. (C.31) and (C.32), we deduce $A_\parallel = -173.1$ kHz and $A_\perp = 22.3$ kHz as given in Sec. 4.2.

C.5 The number of nuclear spins contributing to the signal

Even though $A_\parallel$ and $A_\perp$ are determined with high precisions, there is still a possibility that multiple nuclear spins are contributing to the experimental data. This is possible if multiple nuclear spins share the same hyperfine parameters (within experimental accuracy). This occurs, for instance, if they occupy lattice sites equivalent to each other by symmetry. When multiple nuclear spins are involved but can be regarded as independent, $P_{\rm X}$ is given as

$$P_{\rm X} = \frac{1}{2}[1 + \prod_{i=1}^{N_{\rm nuc}} (2P_{{\rm X},i} - 1)], \tag{C.33}$$

where $N_{\rm nuc}$ is the number of nuclear spins. Figure C.4 shows the data in Fig. 4.7(b) of Sec. 4.2, together with simulations ($N_{\rm nuc} = 1$, 2, and 3) performed using the experimental values. A large oscillation amplitude with its minimum less than 0.5 and a

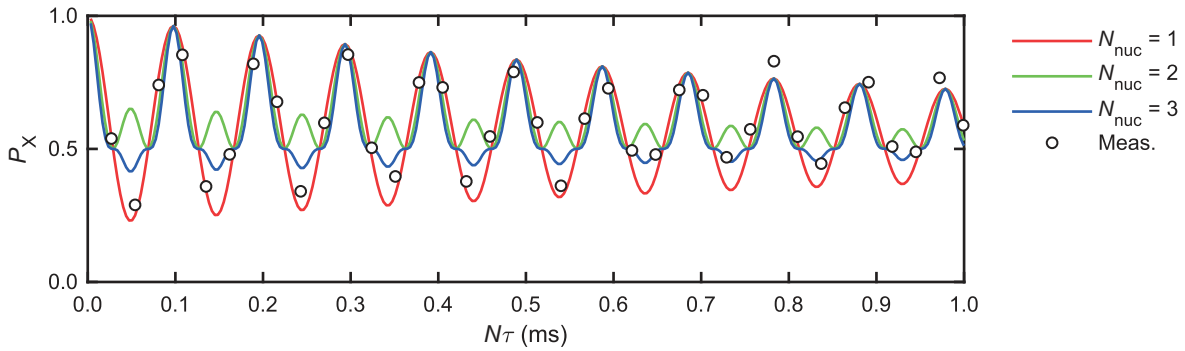

Figure C.4: Data in Fig. 4.7(b) of Sec. 4.2, together with simulations for $N_{\mathrm{nuc}} = 1$, 2, and 3. A single exponential decay with the time constant of 1.23 ms is superposed.

single-component oscillation are hallmarks of a single nuclear spin. The experimental data clearly shows these features, especially at early times before the damping occurs.

C.6 PulsePol method and calibration of the RF pulse length

Sec. 4.2, PulsePol, a pulsed DNP technique recently developed by Schwartz *et al.* [86], was used for the polarization transfer between the NV electron spin and the ^{13}C nuclear spins. While other DNP techniques such as NOVEL [215] and optical pumping [216] may also be applied to this system, we find PulsePol particularly useful because of its robustness and control exibility. Even at low magnetic fields used in our experiments ($B_0 = 36.2$ mT), highly efficient polarization transfer was achieved. In addition, the direction of the polarization can be controlled. Here, we elaborate these features of PulsePol by simulations.

In Fig. C.5(a), we simulate the polarization transfer signal (upper) and the nuclear spin state (lower) after PolX/Y with $N_{\mathrm{pol}} = 5$. The initial state of the target nuclear spin is assumed to be completely mixed ($\rho_n = \frac{1}{2}\mathbf{1}$). The NV spin is initialized to $|m_S = 0\rangle$, and the probability of staying in $|m_S = 0\rangle$, P_0, is reduced when the polarization transfer occurs. Simulated P_0 reproduces well with the experimental observation shown in Fig. 4.8 (□) of Sec. 4.2. Simulated $\langle I \rangle$ shows that the polarization direction is controllable by k ($= 2\tau_{\mathrm{pol}}/f_{\mathrm{t}}$) and the phase-cycling of the sequence (PolX or PolY). N_{pol} is a tunable parameter that determines the bandwidth. We used$N_{\mathrm{pol}} = 5$ to selectively polarize the target nuclei at $k = 3$ by tuning the bandwidth close to that of the $N = 16$ CP sequence.

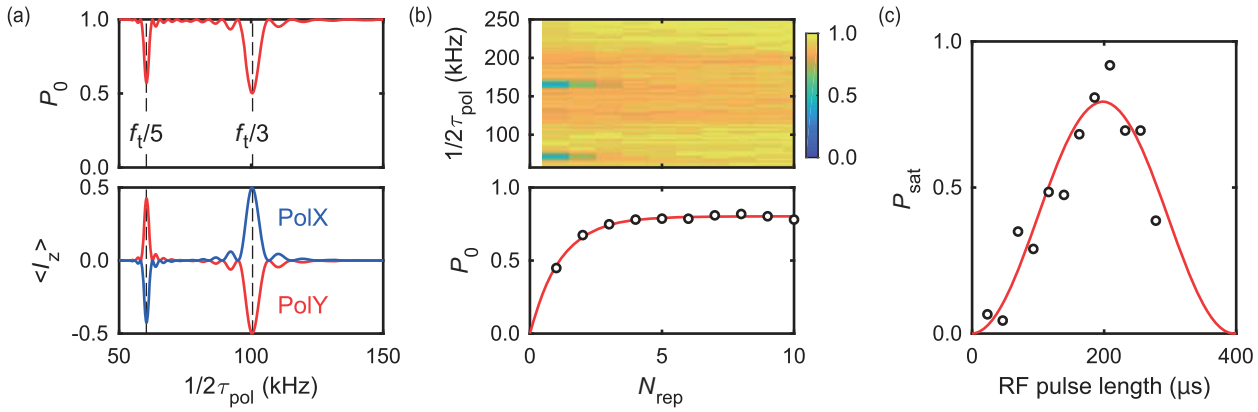

Figure C.5: (a) Simulations of the polarization transfer (upper) and the nuclear spin state (lower) after PolX/Y with $N_{\rm pol} = 5$. (b) Selective polarization transfer by PulsePol as a function of $N_{\rm rep}$. (c) $P_{\rm sat}$ at $k = 3$ as a function of the RF pulse length.

As described in [86] and Appendix D, the rate of polarization transfer is maximized at $k = 3$. The number of repetitions required to transfer an angular momentum of 1 ($\times\hbar$) is estimated as $N_{\rm rep} \geq \pi f_{\rm t}/(3(2+\sqrt{2})A_\perp N_{\rm pol}) \sim 2.5$, where $f_{\rm t} = 301.6$ kHz and $A_\perp = 22.3$ kHz are the experimental values. The color plot in Fig. C.5(b) shows the evolution of the polarization transfer as $N_{\rm rep}$ is increased. The spectrum for $N_{\rm rep} = 1$ corresponds to the square (□) points of Fig. 4.8 of Sec. 4.2. The transferred polarization is evaluated by integrating the $k = 3$ dip [the lower panel of Fig. C.5(b)]. The transfer is efficient up to $N_{\rm rep} = 3$, consistent with the estimation above.

The RF pulse length was calibrated by observing the saturated polarization $P_{\rm sat}$ as a function of the RF pulse length [Fig. C.5(c)]. In order to accurately track the motion of the nuclear spin, we want the lengths of the RF pulses to be integer multiples of oscillation periods. We set the length of the RF π ($\pi/2$) pulse as 199.443 μs (102.041 μs), corresponding to 43 (22) oscillation periods of $f_1 = 215.6$ kHz.

C.7 Analysis of undersampled oscillations

The data in Fig. 4.9(b) of Sec. 4.2 was intentionally undersampled in order to secure sufficiently long $t > 1$ ms [Fig. C.6(a)]. We outline a procedure to analyze undersampled data. In signal processing, the sampling theorem asserts that an oscillation at frequency

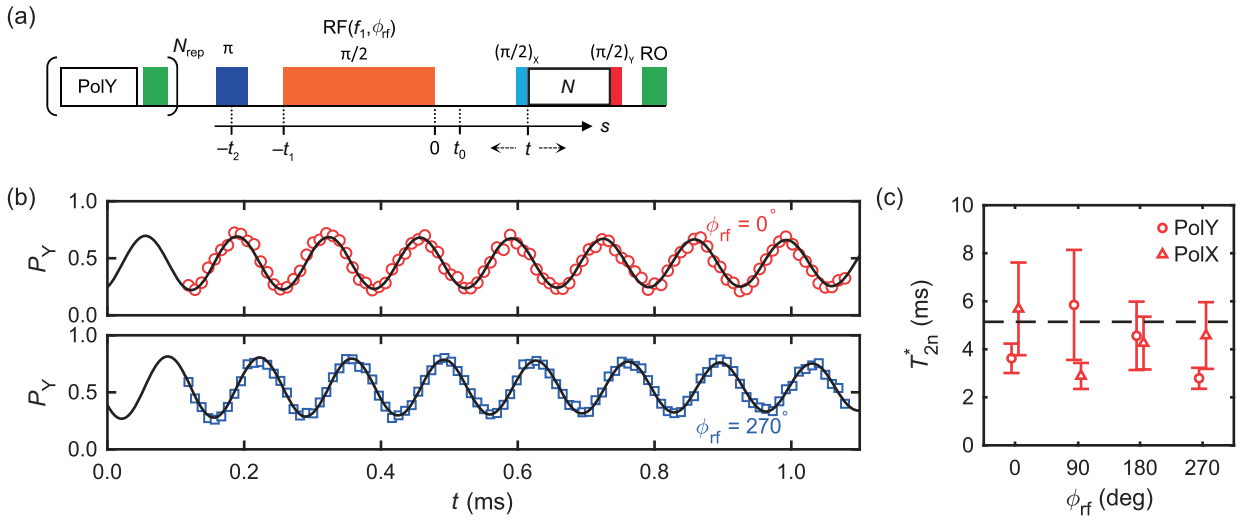

Figure C.6: (a) Pulse protocol to observe nuclear free precessions. See also Fig. 4.6(f) of Sec. 4.2. (b) Undersampled nuclear free precessions. Solid lines are $Ae^{-t/T^*_{2n}}\cos\left(2\pi f^{(4)}t+\eta^{(4)}\right)+B$. (c) T^*_{2n} of the measured nuclear free precessions. ○: PolY, □: PoX. The dashed line indicates T_1 of the sensor spin.

f can be recovered if the sampling rate $(\Delta t)^{-1}$ is set to satisfy

$$\frac{1}{\Delta t}\geq 2f \text{ or } f_{\rm N}\equiv\frac{1}{2\Delta t}\geq f, \tag{C.34}$$

where $f_{\rm N}$ is called the Nyquist frequency. When this condition is not met, measurement points are undersampled. There is a non-zero integer m that satisfies

$$mf_{\rm N}\leq f<(m+1)f_{\rm N}. \tag{C.35}$$

For even m, f and the frequency obtained by undersampling, $f^{(m)}$, is connected by

$$f^{(m)} \;=\; f-mf_{\rm N}. \tag{C.36}$$

Suppose that by fitting to the undersampled data we obtain the phase $\eta^{(m)}$ but the original oscillation has the phase η. The following relation must be satisfied for any integer k:

$$2\pi f^{(m)}(t_0+k\Delta t)+\eta^{(m)}=2\pi f(t_0+k\Delta t)+\eta, \tag{C.37}$$

where t_0 is the starting time of the sampling. It follows that $\eta=\eta^{(m)}-2\pi mf_{\rm N}(t_0+k\Delta t)$ and therefore

$$\eta \;=\; \eta^{(m)}-m\frac{\pi t_0}{\Delta t}\ (\mathrm{mod}\ 2\pi). \tag{C.38}$$

From Fig. 4.9(a) of Sec. 4.2, we already know the oscillation frequency to be 216 kHz. The frequency resolution is limited by relatively short t of about 100 μs, but is sufficient to determine an appropriate undersampling condition. We chose $\Delta t = 9.600$ μs for undersampling of $m = 4$, and $t_0 = 6.872$ μs in order to account for the RF pulse length. We can then recover the original phase using Eq. (C.38).

Figure C.6(b) shows undersampled nuclear free precessions for $\phi_{\rm rf} = 0°$ and $\phi_{\rm rf} = 270°$ (see Sec. C.8 for the definition of $\phi_{\rm rf}$). From fits to the data, we obtain 7.5 kHz, consistent with undersampling of $m = 4$. The recovered original frequency is 215.8 kHz. The phases determined by Eq. (C.38) are plotted in Fig. 4.9(b) of Sec. 4.2. Even though t is extended longer than 1 ms, no significant decays are observed, as expected for nuclear spins. The decay times $T_{2\rm n}^*$ are plotted in Fig. C.6(c). They all take similar values, and fall on around $T_1 = 5.1$ ms of the sensor spin. It is likely that true $T_{2\rm n}^*$ could be longer. Nonetheless, t can still be extended up to T_1 to achieve better precisions.

C.8 Determination of ϕ

In our demonstration shown in Fig. 4.9(a) of Sec. 4.2, the origin of the time axis is defined as the end time of the RF pulse [Fig. C.6(a)], after which the CP sequence to detect nuclear spin precessions can be applied (otherwise the RF field much stronger than the nuclear spin signal will be detected, as performed in Sec. C.2). The crucial information is the azimuthal angle of $\boldsymbol{\nu}_{\rm n}(s = 0)$, $\phi_{\rm n}(0)$. If $\phi_{\rm n}(s = 0)$ is known and the initial phase of the free precession is experimentally determined as ϕ_0, Eq. (C.30) allows us to determine ϕ as

$$\phi \;=\; \begin{cases} \phi_{\rm n}(0) + \phi_0 & \text{for } 0 \le \theta < \frac{\pi}{2} \\ \phi_{\rm n}(0) + \phi_0 + \pi & \text{for } \frac{\pi}{2} \le \theta \le \pi. \end{cases} \tag{C.39}$$

Since we have determined the polar angle θ of the target nuclear spin to be 94.8° in Sec. 4.2, the second relation applies to our case. In future applications aiming at single-molecular NMR spectroscopy, target molecules will be placed at a diamond surface, and the polar angles of target nuclei will always be less than $\pi/2$.

A primary task in this section is to determine $\phi_{\rm n}(0)$ accurately. It should be noted that in real space no sooner does the nuclear spin feel the RF field at $s = -t_1$than the nuclear spin Bloch vector $\boldsymbol{\nu}_{\rm n}(s)$ has a transverse component. We have also seen in Sec. C.3 that the precession axis of the nuclear spin is tilted from the z axis, due to the hyperfine interaction. Therefore, it is important to carefully examine the dynamics of the target nuclear spin in the time range $s \le 0$. To set the stage, we review the experimental sequence of Fig. C.7(a) step by step. See also Fig. C.7.

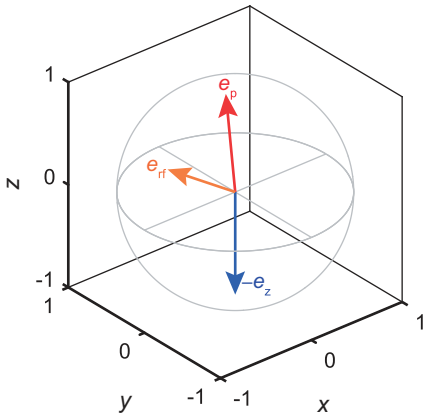

Figure C.7: $\boldsymbol{\nu}_{\mathrm{n}}(s < -t_2) = -\boldsymbol{e}_z$ (blue arrow), $\boldsymbol{e}_{\mathrm{p}}$ (red arrow) and $\boldsymbol{e}_{\mathrm{rf}}$ (orange arrow) in the sensor coordinate.

$s < -t_2$**:**

The target nuclear spin is polarized by PulsePol. We assume that PolY at $k = 3$ is used, so that the nuclear spin is initialized into $\boldsymbol{\nu}_{\mathrm{n}}(s < -t_2) = -\boldsymbol{e}_z$ (Sec. C.6).

$-t_2 \leq s < -t_1$**:**

A 2-μs-long chirped microwave π pulse is applied to flip the NV spin (Sec. C.2). During this time, the NV spin is coherently driven from $|m_S = 0\rangle$ to $|m_S = -1\rangle$, and the precession axis of the nuclear spin tilts from $\boldsymbol{e}_z$ to $\boldsymbol{e}_{\mathrm{p}}$ concurrently (Sec. C.3). We approximate that the precession axis is $\boldsymbol{e}_z$ until the midpoint of the chirped pulse ($s = -t_2$. It then jumps to $\boldsymbol{e}_{\mathrm{p}}$ and is fixed subsequently. In our experiments, $(t_2 - t_1) = 2.288$ μs, which is broken down into 1 μs of the latter half of the chirped pulse, 0.2 μs of the trigger time for the following RF pulse, and $t_{\mathrm{delay}} = 1.088$ μs (Sec. C.2).

$-t_1 \leq s < 0$**:**

An RF $\pi/2$ pulse at $f_1 = 215.6$ kHz is applied to tip the nuclear spin. The pulse length is set as $t_1 = 22/f_1 = 102.041$ μs (Sec. C.6). We define e_{rf} as

$$\boldsymbol{e}_{\mathrm{rf}} = \frac{\boldsymbol{B}_{\mathrm{c}}}{B_{\mathrm{c}}} = \begin{pmatrix} \sin\theta_{\mathrm{c}} \cos\phi_{\mathrm{c}} \\ \sin\theta_{\mathrm{c}} \sin\phi_{\mathrm{c}} \\ \cos\theta_{\mathrm{c}} \end{pmatrix}, \tag{C.40}$$

where $\theta_{\mathrm{c}} = 55.7°$ and $\phi_{\mathrm{c}} = 186.2°$ (Sec. C.2). When a cosine wave $\cos(2\pi f_1 t)$ is applied on the coil, the RF magnetic field $\boldsymbol{B}_{\mathrm{rf}}$ first points to e_{rf}, and after half

the oscillation period it points to $-e_{\rm rf}$; the coil generates a linearly-polarized RF magnetic field along $e_{\rm rf}$.

$0 \leq s < t_0$**:**

The RF pulse is turned off, and the nuclear spin precesses freely. We set $t_0 = 6.872$ μs.

$t_0 \leq s$**:**

The free precession of the nuclear spin is detected by the CP sequence with the $(\pi/2)_{\rm Y}$ readout pulse (Sec. C.3). We experimentally determine the precession frequency $f_{\rm p}$ and ϕ_0.

With this setting, let us first consider the simplest case, in which both $e_{\rm p} \parallel \boldsymbol{e}_z$ and $f_1 = f_{\rm p}$ are satisfied. The first condition is justified when B_0 is higher than a few hundreds of mT. For instance, at $B_0 = 1$ T, $\theta_{\rm p}$ should be suppressed to less than 0.1°. We define the waveform of the RF field as

$$\boldsymbol{B}_{\rm rf}(s) \;=\; 2b(s)\cos\left(2\pi f_1 s + \phi_{\rm rf}\right)\boldsymbol{e}_{\rm rf}, \tag{C.41}$$

with

$$b(s) \;=\; \begin{cases} (4t_1)^{-1} & \text{for } -t_1 \leq s \leq 0 \\ 0 & \text{otherwise.} \end{cases} \tag{C.42}$$

Because $e_{\rm p} \parallel \boldsymbol{e}_z$, the component of $\boldsymbol{B}_{\rm rf}$ projected onto the xy plane ($\boldsymbol{B}_{{\rm rf},\perp}$) only acts to rotate the nuclear spin. In addition, by invoking the rotating wave approximation, it is sufficient to consider a clockwise-rotating component of $\boldsymbol{B}_{{\rm rf},\perp}$, which co-rotates with the nuclear spin. The component of $\boldsymbol{B}_{\rm rf}$ parallel to the z axis ($\boldsymbol{B}_{{\rm rf},\parallel}$) modifies the nuclear precession frequency. However, such a frequency modulation averages out by setting the RF pulse length as an integer multiple of the oscillation period (Sec. C.6), and the effect of $\boldsymbol{B}_{{\rm rf},\parallel}$ becomes negligible.

$\phi_{\rm n}(0)$ is evaluated as

$$\phi_{\rm n}(0) = -\phi_{\rm rf} + \phi_{\rm c} - \frac{\pi}{2} = -\phi_{\rm rf} + 96.2^\circ \ (\mathrm{mod}\ 360^\circ). \tag{C.43}$$

Here, $-\phi_{\rm rf} + \phi_{\rm c}$ s the azimuthal angle of the rotation axis of the nuclear spin (note that $\phi_{\rm rf}$ changes clockwise), and by the RF $\pi/2$ pulse the nuclear spin ends up in the direction orthogonal to it (the negative sign in $-\frac{\pi}{2}$ reflects the rotation direction of the nuclear spin).

When $f_1 \neq f_{\rm p}$, the detuning accumulates as $-2\pi(f_{\rm p}-f_1)t_1$, relative to $-\phi_{\rm rf}+\phi_{\rm c}$. Again, the negative sign is due to the fact that the nuclear spin precesses clockwise, whereas ϕ is

defined counter-clockwise. Experimentally obtained $f_{\rm p}$ is on average $\bar{f}_{\rm p} = 215.7908$ kHz, so the effect of detuning amounts to $-0.319^\circ \times 22 = -7.0^\circ$. $\phi_{\rm n}(0)$ is evaluated as

$$\phi_{\rm n}(0) = -\phi_{\rm rf} + \phi_{\rm c} - \frac{\pi}{2} - 2\pi(\bar{f}_{\rm p} - f_1)t_1 = -\phi_{\rm rf} + 89.2^\circ \ (\text{mod } 360^\circ). \tag{C.44}$$

In Fig. 4.9(b) of Sec. 4.2, we experimentally obtain ϕ_0 as

$$\phi_0 = \phi_{\rm rf} + 334.0^\circ \ (\text{mod } 360^\circ). \tag{C.45}$$

From Eqs. (C.39), (C.44), and (C.45), we obtain

$$\phi = (-\phi_{\rm rf} + 89.2^\circ) + (\phi_{\rm rf} + 334.0^\circ) + 180^\circ = 243.2^\circ (\text{mod } 360^\circ). \tag{C.46}$$

$\phi = 243.2^\circ$ is given as the dashed line in the lower panel of Fig. 4.9(b) of Sec. 4.2, and the accuracy range $243.2^\circ \pm 5.3^\circ$ is shown in the left panel of Fig. 4.9(c).

For more accurate estimation, we consider the case $\boldsymbol{e}_{\rm p} \nparallel \boldsymbol{e}_z$. As mentioned above, this effect is suppressed by applying large B_0, but the present experiments are performed at $B_0 = 36.2$ mT, rendering the polar angle of $\boldsymbol{e}_{\rm p}$ to be 5.9° (Sec. C.3). The effect of $\boldsymbol{e}_{\rm p}$ is worth a careful analysis. This is best done by simulating real-space trajectories of the target nuclear spin in the time range $-t_2 \le s \le 0$, based on the Bloch equation:

$$\frac{d\boldsymbol{\nu}_{\rm n}(s)}{ds} = 2\pi\boldsymbol{\nu}_{\rm n}(s) \times [f_{\rm p}\boldsymbol{e}_{\rm p} + B_{\rm rf}(s)\boldsymbol{e}_{\rm rf}], \tag{C.47}$$

where $b(s)$ appearing in $B_{\rm rf}$ is now

$$b(s) \ = \ \begin{cases} (4t_1|\boldsymbol{e}_z \times e_{\rm p}|)^{-1} & \text{for } -t_1 \le s \le 0 \\ 0 & \text{otherwise.} \end{cases} \tag{C.48}$$

To gain physical insights, we first perform simulations by setting $\phi = 0$ and $f_1 = f_{\rm p} = 215.6$ kHz. The results are shown in Fig. C.8. Simulated $\phi_{\rm n}(0)$ deviates from Eq. (C.43) on the order of $\theta_{\rm p}$. We observe that the inital precession about $\boldsymbol{e}_{\rm p}$, before the RF pulse is applied, is a major source of deviation. Since the azimuthal angle of $\boldsymbol{e}_{\rm p}$ is ϕ, this type of deviation sinusoidally depends on ϕ as well as on $\phi_{\rm rf}$ and $(t_2 - t_1)$. One way to suppress this effect at low fields may be to set $(t_2 - t_1)$ as an integer multiple of the precession period, so that the nuclear spin returns to $-\boldsymbol{e}_z$ when the RF field is applied.

We remark that there is a more subtle, additional effect of $\boldsymbol{e}_{\rm p}$ that is in play during the RF pulse. Once the RF field is applied, the nuclear spin rotates, to a good approximation, around $B_{\rm rf,\perp}$. However, because now the nuclear spin feels a circularly-polarized RF field that is rotating in the plane perpendicular to $\boldsymbol{e}_{\rm p}$, the nuclear spin does not end up in the xy plane exactly (even when the nuclear spin starts to rotate from $-\boldsymbol{e}_z$). When the

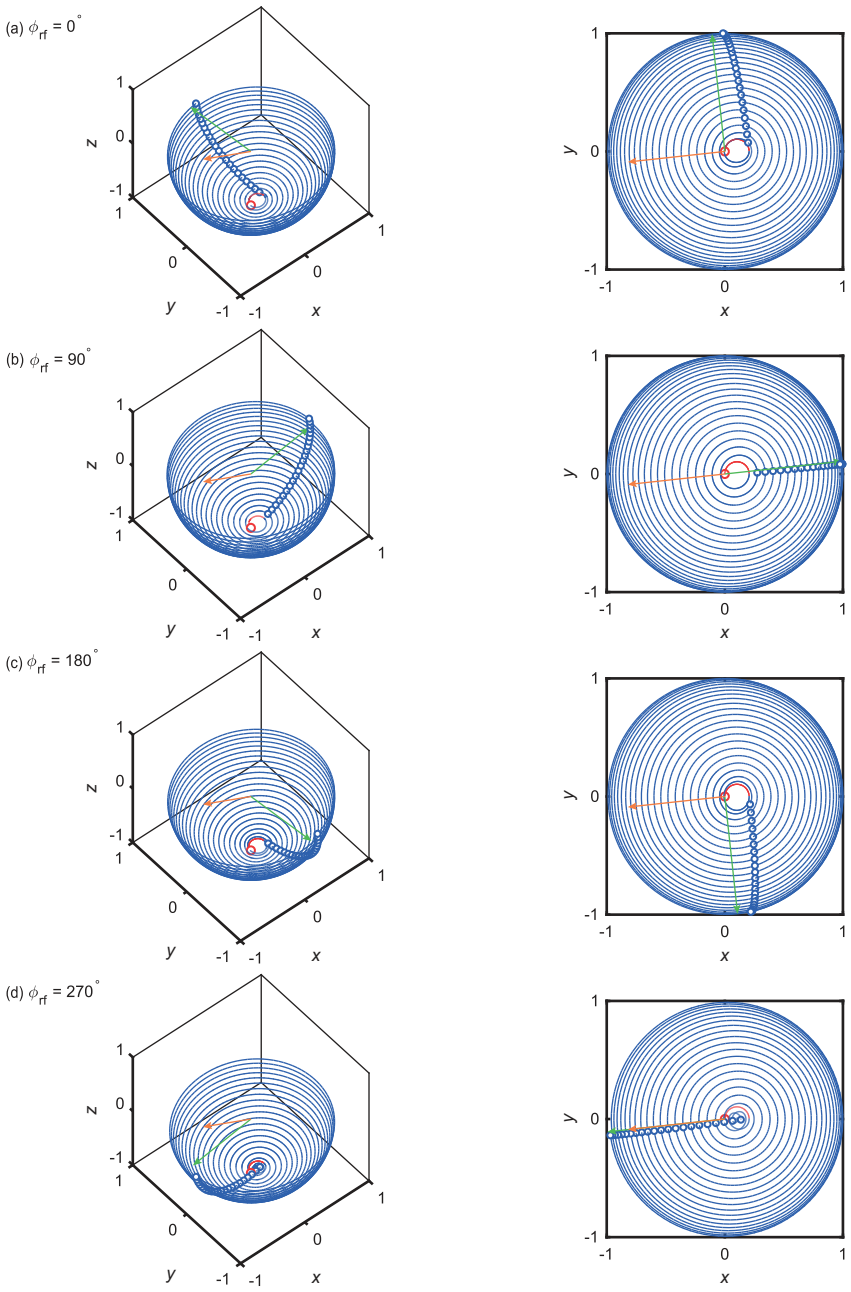

Figure C.8: Dynamics of the target nuclear spin with the simulation parameters $\phi = 0$ and $f_1 = f_p = 215.6$ kHz. (a) $\phi_{rf} = 0°$, (b) 90°, (c) 180°, and (d) 270°. The orange arrow indicates $\boldsymbol{e}_{rf}$. The red circles ($\circ$) indicate the initial position. The red (blue) curves are the trajectories during $-t_2 \leq s < -t_1$ ($-t_1 \leq s \leq 0$). The blue circles ($\circ$) follow the stroboscopic trajectories at $s = -t_1 + k/f_1$, with $k = 0, 1, \cdots, 22$, similar to the ones observed in the rotating frame. The green arrows indicate $\phi_n(0)$ evaluated using Eq. (C.43). The values of simulated $\phi_n(0)$ are 90.9° at $\phi_{rf} = 0°$, 4.8° at $\phi_{rf} = 90°$, 282.7° at $\phi_{rf} = 180°$, and 188.1° at $\phi_{rf} = 270°$.

nuclear spin is projected onto the xy plane, this effect is seen to depend on ϕ, but not on $\phi_{\rm rf}$. What is seen in Fig. C.8 is a cumulative effect of two roles that $\boldsymbol{e}_{\rm p}$ plays, making the deviation from Eq. (C.43) less systematic as changing $\phi_{\rm rf}$. If $(t_2 - t_1)$ is as an integer multiple of the precession period, only the latter is effective. The deviation becomes systematic, and the analysis will be facilitated.

We set ϕ and $\phi_{\rm rf}$ as parameters in the simulation, and find the value of ϕ that best reproduces the experimental data. The precession frequency is set as $\bar{f}_{\rm p}$, and assumed to be independent of $\phi_{\rm rf}$. The simulation result for $\phi = 248.8°$ is shown in Fig. C.9, for which the deviation from the experimental data is minimized. $\phi = 248.8°$ is given as the dotted line in the lower panel of Fig. 4.9(b) of Sec. 4.2, and the accuracy range $248.8° \pm 2.7°$ is shown in the middle panel of Fig. 4.9(c).

Strictly speaking, measured precession frequencies $f_{\rm p}$ vary from one measurement to another. This is partly attributed to errors in the fits, but it is also conceivable that the precession frequency indeed differs in different measurements, due to, for instance, temperature drifts (which can change B_0 provided by a permanent magnet). Therefore, lastly, we perform simulations by setting ϕ as the only parameter and using the values of $f_{\rm p}$ for the respective runs. The results are shown as the circles ($\circ$) in the lower panel of Fig. 4.9(b) of Sec. 4.2, and their average value, 247.8°, is given as the solid line. The accuracy range $247.8° \pm 4.1°$ is shown in the right panel of Fig. 4.9(c).

The lattice site that falls on these accuracy ranges are shown as blue circles in Fig. 4.9(c), which have $\phi = 250.9°$. Therefore, we determine is the position of the target nuclear spin as (r,θ,ϕ) = (6.84 Å, 94.8°, 250.9°).

C.9 Demonstration of the protocol on a different single ^{13}C nuclear spin

Here, we show results on a single nuclear spin different from the one discussed in Sec. 4.2. Figure C.10(a) shows the NMR spectrum given in Fig. 4.7(a) of Sec. 4.2. We observe that there is another dip at $f_{\rm t} = 443.4$ kHz, albeit overlapping with the broad dip arising from the bath nuclei. We examined this signal in more detail (as done on the first nuclear spin in Sec. 4.2), and determined its hyperfine parameters as $A_{\parallel} = 112.1$ kHz and $A_{\perp} = 59.9$ kHz. Unfortunately, we have not been able to narrow down the lattice site it belongs to, because we do not find theoretical values sufficiently close to them. Although we do not have r and θ of this second nuclear spin, the protocol can still be applied to estimate ϕ. A summary of the experiments are shown in Figs. C.10(b) and (c). All the experimental parameters, given in the caption of Fig. C.10, are optimized for this nuclear

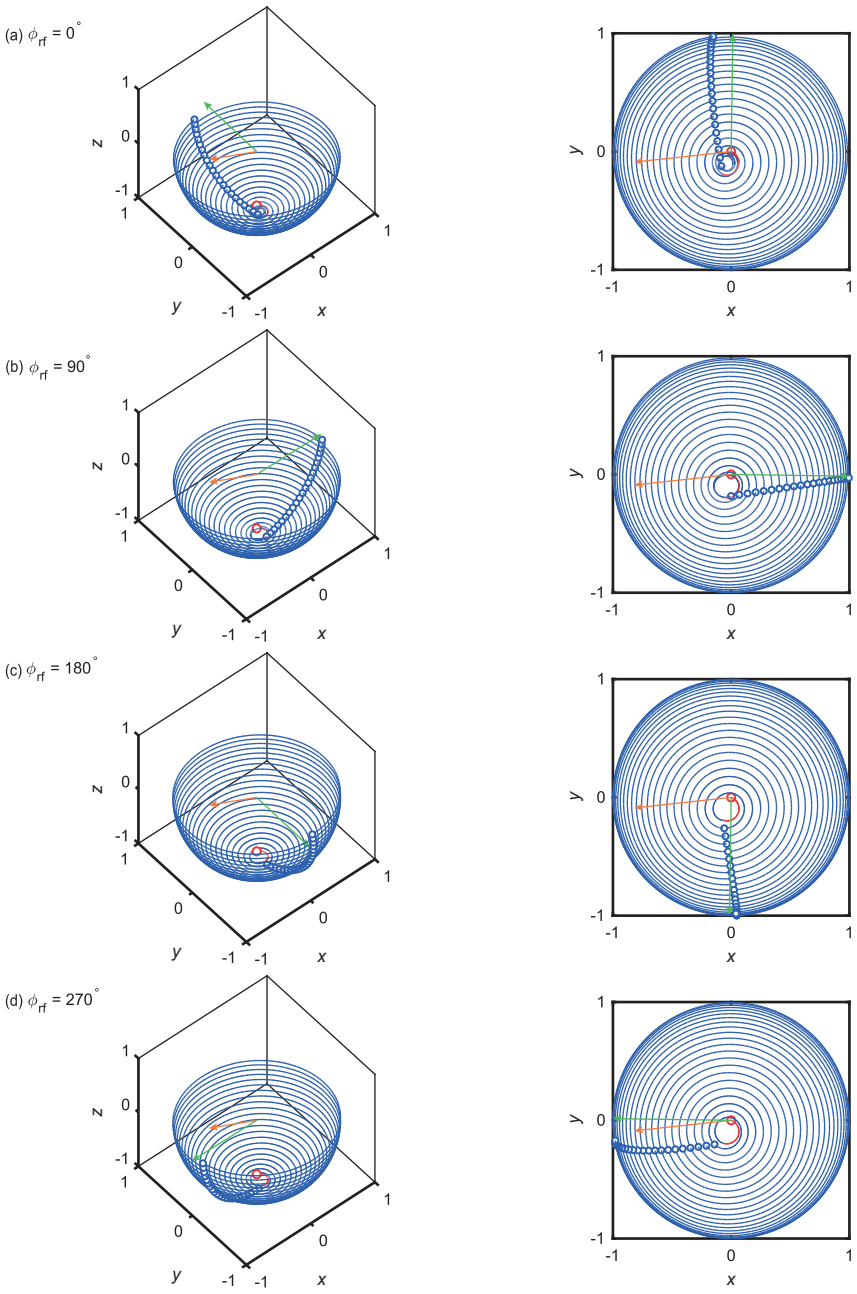

Figure C.9: Dynamics of the target nuclear spin with the simulation parameters $\phi = 248.8$, $f_1 = 215.6$ kHz, and $f_p = 215.7908$ kHz. (a) $\phi_{rf} = 0°$, (b) 90°, (c) 180°, and (d) 270°. The green arrows indicate $\phi_n(0)$ evaluated using Eq. (C.44). The values of simulated $\phi_n(0)$ are 98.9° at $\phi_{rf} = 0°$, 358.4° at $\phi_{rf} = 90°$, 272.4° at $\phi_{rf} = 180°$, and 189.9° at $\phi_{rf} = 270°$.

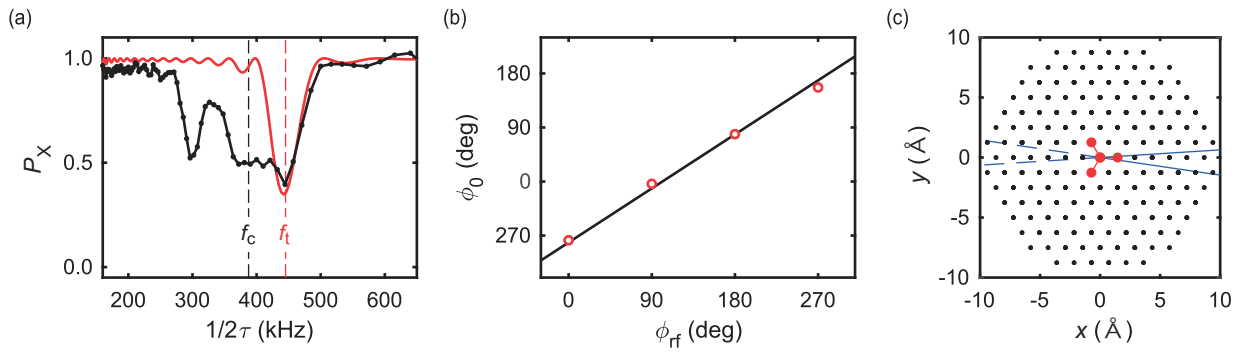

Figure C.10: (a) Data in Fig. 4.7(a) of Sec. 4.2 with a simulation to a different dip at $f_t = 443.4$ kHz. (b) $\phi_{\rm rf}$ vs. ϕ_0 for the second target nuclear spin. The experimental parameters are $f_1 = 503.0$ kHz, $t_0 = 4.403$ μs, $t_1 = 214.725$ μs (108 periods), and $t_2 = 216.797$ μs. $\bar{f}_{\rm p} = 503.0$ kHz is obtained. (c) Estimated ϕ of the second target nuclear spin. The accuracy ranges are $357.7^\circ \pm 8.6^\circ$ for $0 \leq \theta \leq \frac{\pi}{2}$ and $177.7^\circ \pm 8.6^\circ$ for $\frac{\pi}{2} \leq \theta \leq \pi$.

spin. Note that there remain two possible ranges of ϕ, differing by 180°, due to the lack of knowledge on θ. Nonetheless, these values are different from those obtained from the first target nuclear spin, and support our claim that the values of ϕ obtained in our protocol are specific to the individual nuclear spins.

C.10 Observation of bath ^{13}C nuclear spins by coherent averaging

As commented Sec. 4.2, our protocol can be combined with the ultrahigh resolution sensing protocol reported in [83–85, 150]. We reinforce this claim by observing bath ^{13}C nuclear spins, using the sequence shown in Fig. C.11(a). On the one hand, this sequence is essentially the same as coherently averaged synchronized readout described in [85]; after inducing free precessions of bath nuclei by an RF $\pi/2$ pulse, we record them by repeating the CP sequence with the regular interval of $t_{\rm L}$. On the other hand, coherent averaging of the signal from a handful of nuclear spins is possible only when PulsePol is applied prior to the RF $\pi/2$ pulse. Even though the bath nuclei contain multiple nuclear spins, they cannot be regarded as an ensemble as in the case of external proton spins in [85]. Rather, the bath nuclei are a collection of independent single nuclear spins, the individual hyperfine parameters of which could in principle be resolved by ultrahigh

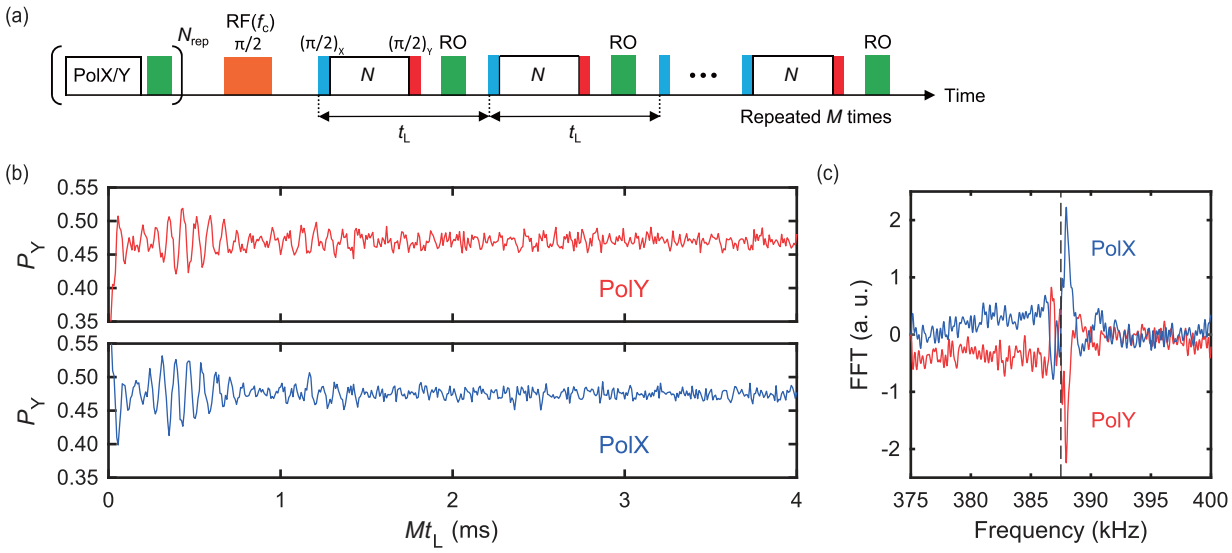

Figure C.11: (a) Pulse protocol to observe the bath nuclear spins. The RF frequency is set at $f_c = \gamma_c B_0 = 387.5$ kHz. (b) P_Y as a function of Mt_L. (c) FFT of (b). The dashed line indicates f_c.

resolution sensing protocol.

We polarize the bath nuclei by PulsePol with $2\tau_{pol} = 7.744$ μs ($= 3f_c^{-1}$), $N_{pol} = 1$, and $N_{rep} = 200$. The RF ($\pi/2$) pulse tuned at f_c is applied, and the CP sequence with $N = 2$ and $2\tau = 2.581$ μs ($= f_c^{-1}$) was repeated $M = 501$ times with the interval of $t_L = 8.000$ μs. To mitigate possible back actions on the nuclear spins, the number of pulses in the CP sequence was minimized ($N = 2$). For the same reason, the signals are undersampled at $m = 6$. Figure C.11(b) shows measured oscillations for PolY and PolX, and their FFT spectra (real part, with the frequency shift due to undersampling corrected) are shown in Fig. C.11(c). Clearly, the oscillation phases are opposite, consistent with our main result on the single nuclear spin [Fig. 4.9(b) of Sec. 4.2]. While a further analysis of Figs. C.11(b) and (c) is outside of the scope of the present work, multiple signals present in the data suggest that we are detecting multiple nuclear spins simultaneously and the phases of the respective frequency components carry the information on the azimuthal angles of the respective nuclear spins. We note that the sequence in Fig. C.11(a) does not use a microwave π pulse prior to the RF $\pi/2$ pulse, and therefore the precession axis of the nuclear spins is fixed as $\boldsymbol{e}_z$.

Finally, we checked that the signal decay time does not depend on t_L, indicating that the present decay time is not limited by the back actions that the sequence exerts on

the nuclear spins. An understanding of sources of the decay will be a subject of future research.

Appendix D

Detail analysis of PulsePol

Calculation of average Hamiltonian during PulsePol is shown here. We follow calculation steps of the original PulsePol paper [86]. We further simplify the condition of flip-flop and flip-flip and its interaction amplitude.

D.1 Resonance condition and behavior of PulsePol

PolY and PolX consists of two sequence blocks, (1) $(\pi/2)_{\mathrm{Y}}$-$(\pi)_{-\mathrm{X}}$-$(\pi/2)_{\mathrm{Y}}$ and (2) $(\pi/2)_{\mathrm{X}}$-$(\pi)_{\mathrm{Y}}$-$(\pi/2)_{\mathrm{X}}$. We consider a simple Hamiltonian in nuclear spin rotating frame which is given as,

$$\hat{H}_0 = A_\perp \hat{S}_z \left[\cos(\omega_{\mathrm{n}} t)\hat{I}_x + \sin(\omega_{\mathrm{n}} t)\hat{I}_y\right]. \tag{D.1}$$

The electron spin evolution during (1) is given by,

$$U_{(1)} = U_{\pi/2,\mathrm{Y}} U_z U^\dagger_{\pi,\mathrm{X}} U_z U_{\pi/2,\mathrm{Y}} \tag{D.2}$$

$$= U^\dagger_{\pi,\mathrm{X}} U_x U_{-x}, \tag{D.3}$$

with

$$U_j = e^{-iA_\perp \boldsymbol{e}_j \cdot \hat{\boldsymbol{S}}\left[\cos(\omega_{\mathrm{n}} t)\hat{I}_x + \sin(\omega_{\mathrm{n}} t)\hat{I}_y\right]\frac{\tau_{\mathrm{pol}}}{4}}, \tag{D.4}$$

where $\boldsymbol{e}_j$ is unit vector along j direction ($j = -x, -y, -z, x, y$ and z). $\hat{S}_x$ component is modulated during (1) sequence block. Whereas, the electron spin evolution during (2) is given by,

$$U_{(2)} = U_{\pi,\mathrm{Y}} U_{-y} U_y. \tag{D.5}$$

$\hat{S}_x$ component is modulated during (2) sequence block. In PulsePol, these sequence blocks are alternatively repeated, and they create effective electron spin precession at nuclear

precession frequency. Using Eq. (D.3) and Eq. (D.5), the evolution of PolY is simplified as,

$$U_{\rm pol} = [U_{(2)}U_{(1)}U_{(2)}U_{(1)}]^{N_{\rm pol}}, \tag{D.6}$$
$$= [U_{-y}U_yU_{-x}U_xU_yU_{-y}U_xU_{-x}]^{N_{\rm pol}}. \tag{D.7}$$

The effective Hamiltonian during PulsePol sequence is given as,

$$\hat{H}_{0,\rm eff} = A_\perp(f_x(t)\hat{S}_x + f_y(t)\hat{S}_y)\left[\cos(\omega_{\rm n}t)\hat{I}_x + \sin(\omega_{\rm n}t)\hat{I}_y\right], \tag{D.8}$$

with

$$f_x(t+2\tau_{\rm pol}m) = \begin{cases} -1 & \text{for} \quad 0 \le \mathrm{t} \le \tau_{\rm pol}/4, 5\tau_{\rm pol}/4 \le \mathrm{t} \le 3\tau_{\rm pol}/2 \\ +1 & \text{for} \quad \tau_{\rm pol}/4 \le \mathrm{t} \le \tau_{\rm pol}/2, \tau_{\rm pol} \le \mathrm{t} \le 5\tau_{\rm pol}/4 \\ 0 & \text{otherwise,} \end{cases} \tag{D.9}$$
$$= \sum_{k=1}^{\rm inf} a_k^x \cos\left(\frac{\pi k t}{\tau_{\rm pol}}\right) + b_k^x \sin\left(\frac{\pi k t}{\tau_{\rm pol}}\right), \tag{D.10}$$
$$f_y(t+2\tau_{\rm pol}m) = \sum_{k=1}^{\rm inf} a_k^y \cos\left(\frac{\pi k t}{\tau_{\rm pol}}\right) + b_k^y \sin\left(\frac{\pi k t}{\tau_{\rm pol}}\right) = f_x\left(t - \frac{\tau_{\rm pol}}{2}\right). \tag{D.11}$$

The Fourier components are obtained by Fourier transform, for example,

$$a_k^x = \frac{1}{\tau_{\rm pol}}\int_0^{2\tau_{\rm pol}} f_x(t)\cos\left(\frac{\pi k t}{\tau_{\rm pol}}\right)dt \tag{D.12}$$
$$= -\frac{2\sin\left(\frac{\pi k}{4}\right) - \sin\left(\frac{\pi k}{2}\right) + \sin(\pi k) - 2\sin\left(\frac{5\pi k}{4}\right) + \sin\left(\frac{3\pi k}{2}\right)}{\pi k}. \tag{D.13}$$

They are periodical against k, and take non-zero value when k is odd integer. All five cases for a_k^x are given as,

$$a_k^x = \begin{cases} -2(\sqrt{2}-1)/k\pi & \text{for mod}(k,8) = 1 \\ -2(\sqrt{2}+1)/k\pi & \text{for mod}(k,8) = 3 \\ 2(\sqrt{2}+1)/k\pi & \text{for mod}(k,8) = 5 \\ 2(\sqrt{2}-1)/k\pi & \text{for mod}(k,8) = 7 \\ 0 & \text{otherwise.} \end{cases} \tag{D.14}$$

Another Fourier component of f_x is calculated by similar way, and it can be described with a_k^x as,

$$b_k^x = (-1)^{\frac{k+1}{2}} a_k^x. \tag{D.15}$$

According to Eq. (D.11), Fourier components of f_y are obtained from f_x, and they are described using a_k^x as,

$$a_k^y = a_k^x \tag{D.16}$$
$$b_k^y = (-1)^{\frac{k-1}{2}} a_k^x. \tag{D.17}$$

Polarization transfer condition is realized when frequency of Fourier components is matched with target precession, i.e. $\omega_{\rm n} = \frac{k\pi}{\tau_{\rm pol}}$. At this condition, the time average of effective Hamiltonian [Eq. (D.7)] is described as,

$$\hat{H}_{0,\rm ave} = \frac{\sqrt{2}a_k^x A_\perp}{2}(\hat{S}'_x\hat{I}_x - (-1)^{\frac{k+1}{2}}\hat{S}'_y\hat{I}_y), \tag{D.18}$$

where $\hat{S}'_x = \frac{\hat{S}_x+\hat{S}_y}{\sqrt{2}}$,$\hat{S}'_y = \frac{-\hat{S}_x+\hat{S}_y}{\sqrt{2}}$ are 45° rotated $\hat{S}_x$ and $\hat{S}_y$ operators, respectively. The averaged Hamiltonian depends on resonance conditions, and it gets flip-flop (flip-flip) when $\frac{k+1}{2}$ is odd (even) integer. For PolX case, the phase relation between f_x and f_y is different from PolY, and averaged Hamiltonian gets flip-flop (flip-flip) when $\frac{k+1}{2}$ is even (odd) integer, which is opposite situation from PolY. The efficiency of the polarization transfer is described by $\alpha_{\rm pol} = \sqrt{2}|a_k^x|$, which is the ratio of the interaction strength between this method and ideal Hartmann-Hahn condition under NOVEL. The maximum efficiency is achieved as $\alpha_{\rm pol} = 2(2+\sqrt{2})/3\pi \approx 0.72$ at $k = 3$ resonance condition.

The polarization transfer condition is robust against microwave detuning, because the resonance condition defined by pulse timing. $\pi/2$ pulse and π pulse used for PulsePol is also robust against microwave detuning at high microwave power. Even this method has high robustness against microwave detuning, the efficiency at $k = 3$ condition is comparable with NOVEL or much better than ISE technique at practical condition. Detail comparison of PulsePol, NOVEL and ISE techniques has been examined in Ref. [86].

D.2 Systematic simplification of unitary operations

The phase controlled pulses are used for measurement sequences to engineer spin directions. An unitary operation for a sequence block for PulsePol, $(\pi/2)_{\rm Y}$-$(\pi)_{-\rm X}$-$(\pi/2)_{\rm Y}$, is given in Eq. (D.2). To discuss electron spin motion, we simplify Eq. (D.2) by calculating net rotation of free evolution with pulse operations. Eq. (D.2) is rewritten by introducing identity operation $\mathbf{1} = (U_{\pi/2,\rm Y}U^\dagger_{\pi/2,\rm Y})$ as,

$$U_{(1)} = U_{\pi/2,\rm Y}(U_{\pi/2,\rm Y}U^\dagger_{\pi/2,\rm Y})U_z U^\dagger_{\pi,\rm X}U_z U_{\pi/2,\rm Y} \tag{D.19}$$
$$= U_{\pi,\rm Y}U^\dagger_{\pi/2,\rm Y}(U_z U^\dagger_{\pi,\rm X}U_z)U_{\pi/2,\rm Y}, \tag{D.20}$$

In side of the brackets, $U_z U^\dagger_{\pi,\mathrm{X}} U_z$ are rotated by $\pi/2$ about $-\mathrm{Y}$ axes with $U^\dagger_{\pi/2,\mathrm{Y}}$. Eq. (D.20) is then simplified as,

$$U_{(1)} = U_{\pi,\mathrm{Y}} U_{-x} U^\dagger_{\pi,\mathrm{Z}} U_{-x}. \tag{D.21}$$

We further simplify Eq. (D.21) by introducing $\mathbf{1} = (U^\dagger_{\pi/2,\mathrm{Z}} U_{\pi/2,\mathrm{Z}})$,

$$\begin{aligned} U_{(1)} &= U_{\pi,\mathrm{Y}} (U^\dagger_{\pi/2,\mathrm{Z}} U_{\pi/2,\mathrm{Z}}) U_{-x} U^\dagger_{\pi,\mathrm{Z}} U_{-x} && \text{(D.22)} \\ &= U_{\pi,\mathrm{Y}} U^\dagger_{\pi/2,\mathrm{Z}} U_x U_{-x}. && \text{(D.23)} \end{aligned}$$

Using a relation, $U_{\pi,\mathrm{Y}} U^\dagger_{\pi/2,\mathrm{Z}} = U^\dagger_{\pi,\mathrm{X}}$, we obtain Eq. (D.3),

$$U_{(1)} = U^\dagger_{\pi,\mathrm{X}} U_x U_{-x}. \tag{D.24}$$

Similarly, an unitary operation for another sequence block for PulsePol, $(\pi/2)_{\mathrm{X}}$-$(\pi)_{\mathrm{Y}}$-$(\pi/2)_{\mathrm{X}}$, is given as,

$$\begin{aligned} U_{(2)} &= U_{\pi/2,\mathrm{X}} U_z U_{\pi,\mathrm{Y}} U_z U_{\pi/2,\mathrm{X}} && \text{(D.25)} \\ &= U_{\pi,\mathrm{Y}} U_{-y} U_y, && \text{(D.26)} \end{aligned}$$

thus we get Eq. (D.5). We also use same idea to get Eq. (D.7) from Eq. (D.6).

References

[1] G. Davies and M. F. Hamer. Optical studies of the 1.945 ev vibronic band in diamond. *Proc. R. Soc. London Ser. A*, 384:285, 1976.

[2] J. H. N. Loubser and J. A. van Wyk. Electron spin resonance in the study of diamond. *Rep. Prog. Phys.*, 41:1201, 1978.

[3] N. R. S. Reddy, N. B. Manson, and E. R. Krausz. Two-laser spectral hole burning in a colour centre in diamond. *J. Lumin.*, 38:46, 1987.

[4] P. D. Bloch, W. S. Brochlesby, R. T. Harley, and M. J. Henderson. EFFECTS OF MICROWAVE EXCITATION ON SPECTRAL HOLE-BURNING IN COLOUR CENTRE SYSTEMS. *J. Phys. (Paris), Colloq.*, 46:C7–527, 1985.

[5] E. van Oort, N. B. Manson, and M. Glasbeek. Optically detected spin coherence of the diamond N-V centre in its triplet ground state. *J. Phys. C: Solid State Phys.*, 21:4385, 1988.

[6] A. Gruber, A. Däbenstedt, C. Tietz, L. Fleury, J. Wrachtrup, and C. von Borczyskowski. Scanning Confocal Optical Microscopy and Magnetic Resonance on Single Defect Centers. *Science*, 276:2012, 1997.

[7] F. Jelezko, T. Gaebel, I. Popa, A. Gruber, and J. Wrachtrup. Observation of Coherent Oscillations in a Single Electron Spin. *Phys. Rev. Lett.*, 92:076401, 2004.

[8] F. Jelezko, T. Gaebel, I. Popa, M. Domhan, A. Gruber, and J. Wrachtrup. Observation of Coherent Oscillation of a Single Nuclear Spin and Realization of a Two-Qubit Conditional Quantum Gate. *Phys. Rev. Lett.*, 93:130501, 2004.

[9] J. Meijer, B. Burchard, M. Domhan, C. Wittman, T. Gaebel, I. Popa, F. Jelezko, and J. Wrachtrup. Generation of single color centers by focused nitrogen implantation. *Appl. Phys. Lett.*, 87:261909, 2005.

[10] J. R. Rabeau, P. Reichart, G. Tamanyan, D. N. Jamieson, S. Prawer, F. Jelezko, T. Gaebel, I. Popa, M. Domhan, and J. Wrachtrup. Implantation of labelled single nitrogen vacancy centers in diamond using ^{15}N. *Appl. Phys. Lett.*, 88:023113, 2006.

[11] T. Gaebel, M. Domhan, I. Popa, C. Wittmann, P. Neumann, F. Jelezko, J. R. Rabeau, N. Stavrias, A. D. Greentree, S. Prawer, J. Meijer, J. Twamley, P. R. Hemmer, and J. Wrachtrup. Room-temperature coherent coupling of single spin in diamond. *Nat. Phys.*, 2:408, 2006.

[12] L. Childress, J. M. Taylor, A. S. Sørensen, and M. D. Lukin. Fault-tolerant quantum repeaters with minimal physical resources and implementation based on single-photon emitters. *Phys. Rev. A*, 72:052330, 2005.

[13] L. Childress, M. V. Gurudev Dutt, J. M. Taylor, A. S. Zibrov, F. Jelezko, J. Wrachtrup, P. R. Hemmer, and M. D. Lukin. Coherent Dynamics of Coupled Electron and Nuclear Spin Qubits in Diamond. *Science*, 314:281, 2006.

[14] M. V. Gurudev Dutt, L. Childress, L. Jiang, E. Togan, J. Maze, F. Jelezko, A. S. Zibrov, P. R. Hemmer, and M. D. Lukin. Quantum Register Based on Individual Electronic and Nuclear Spin Qubits in Diamond. *Science*, 316:1312, 2007.

[15] R. J. Epstein, F. M. Mendoza, Y. K. Kato, and D. D. Awschalom. Anisotropic interactions of a single spin and dark-spin spectroscopy in diamond. *Nat. Phys.*, 1:94, 2005.

[16] R. Hanson, O. Gywat, and D. D. Awschalom. Room-temperature manipulation and decoherence of a single spin in diamond. *Phys. Rev. B*, 74:161203, 2006.

[17] R. Hanson, F. M. Mendoza, R. J. Epstein, and D. D. Awschalom. Polarization and Readout of Coupled Single Spins in Diamond. *Phys. Rev. Lett.*, 97:087601, 2006.

[18] R. Hanson, V. V. Dobrovitski, A. E. Feiguin, O. Gywat, and D. D. Awschalom. Coherent Dynamics of a Single Spin Interacting with an Adjustable Spin Bath. *Science*, 320:352, 2008.

[19] S. Takahashi, R. Hanson, J. van Tol, M. S. Sherwin, and D. D. Awschalom. Quenching Spin Decoherence in Diamond through Spin Bath Polarization. *Phys. Rev. Lett.*, 101:047601, 2008.

[20] J. M. Taylor, P. Cappellaro, L. Childress, L. Jiang, D. Budker, P. R. Hemmer, A. Yacoby, R. Walsworth, and M. D. Lukin. High-sensitivity diamond magnetometer with nanoscale resolution. *Nat. Phys.*, 4:810, 2008.

[21] B. M. Chernobrod and G. P. Berman. Spin microscope based on optically detected magnetic resonance. *J. Appl. Phys.*, 97:014903, 2005.

[22] G. P. Berman, A. R. Bishop, B. M. Chernobrod, M. E. Hawley, G. W. Brown, and V. I. Tsifrinovich. Measurement of single electron and nuclear spin states based on optically detected magnetic resonance. *J. Phys.: Conf. Ser*, 38:3207, 2006.

[23] P. Glover and S. P. Mansfield. Limits to magnetic resonance microscopy. *Rep. Prog. Phys.*, 65:1489, 2002.

[24] J. R. Maze, P. L. Stanwix, J. S. Hodges, S. Hong, J. M. Taylor, P. Cappellaro, L. Jiang, M. V. Gurudev Dutt, E. Togan, A. S. Zibrov, A. Yacoby, R. L. Walsworth, and M. D. Lukin. Nanoscale magnetic sensing with an individual electronic spin in diamond. *Nature*, 455:644, 2008.

[25] G. Balasubramanian, I. Y. Chan, R. Kolesov, M. Al-Hmoud, J. Tisler, C. Shin, C. Kim, A. Wojcik, P. R. Hemmer, A. Krueger, T. Hanke, A. Leitenstorfer, R. Bratschitsch, F. Jelezko, and J. Wrachtrup. Nanoscale imaging magnetometry with diamond spins under ambient conditions. *Nature*, 455:648, 2008.

[26] C. L. Degen. Scanning magnetic field microscope with a diamond single-spin sensor. *Appl. Phys. Lett.*, 92:243111, 2008.

[27] J. Isberg, J. Hammersberg, E. Johansson, T. Wikström, D. J. Twitchen, A. J. Whitehead, S. E. Coe, and G. A. Scarsbrook. High carrier mobility in single-crystal plasma-deposited diamond. *Science*, 297:1670, 2002.

[28] C. Santori, P. E. Barclay, K.-M. C. Fu, and R. G. Beausoleil. Vertical distribution of nitrogen-vacancy centers in diamond formed by ion implantation and annealing. *Phys. Rev. B*, 79:125313, 2009.

[29] P. E. Barclay, K.-M. C. Fu, C. Santori, and R. G. Beausoleil. Chip-based microcavities coupled to nitrogen-vacancy centers in single crystal diamond. *Appl. Phys. Lett.*, 95:191115, 2009.

[30] K.-M. C. Fu, C. Santori, P. E. Barclay, L. J. Rogers, N. B. Manson, and R. G. Beausoleil. Observation of the Dynamic Jahn-Teller Effect in the Excited States of Nitrogen-Vacancy Centers in Diamond. *Phys. Rev. Lett.*, 103:256404, 2009.

[31] C. Santori, P. E. Barclay, K.-M. C. Fu, R. G. Beausoleil, S. Spillane, and M. Fisch. Nanophotonics for quantum optics using nitrogen-vacancy centers in diamond. *Nanotechnology*, 21:274008, 2010.

[32] L. Robledo, H. Bernien, Ilse van Weperen, and R. Hanson. Control and Coherence of the Optical Transition of Single Nitrogen Vacancy Centers in Diamond. *Phys. Rev. Lett.*, 105:177403, 2010.

[33] V. M. Acosta, E. Bauch, M. P. Ledbetter, C. Santori, K.-M. C. Fu, P. E. Barclay, R. G. Beausoleil, H. Linget, J. F. Roch, F. Treussart, S. Chemerisov, W. Gawlik, and D. Budker. Diamonds with a high density of nitrogen-vacancy centers for magnetometry applications. *Phys. Rev. B*, 80:115202, 2009.

[34] V. M. Acosta, E. Bauch, M. P. Ledbetter, A. Waxman, L.-S. Bouchard, and D. Budker. Temperature Dependence of the Nitrogen-Vacancy Magnetic Resonance in Diamond. *Phys. Rev. Lett.*, 104:070801, 2010.

[35] G. Balasubramanian, P. Neumann, D. Twitchen, M. Markham, R. Kolesov, N. Mizouchi, J. Isoya, J. Achard, J. Beck, J. Tissler, V. Jacques, P. R. Hemmer, F. Jelezko, and J. Wrachtrup. Ultralong spin coherence time in isotopically engineered diamond. *Nat. Mater.*, 8:383, 2009.

[36] B. J. Maertz, A. P. Wijnheijmer, G. D. Fuchs, M. E. Nowakowski, and D. D. Awschalom. Vector magnetic field microscopy using nitrogen vacancy centers in diamond. *Appl. Phys. Lett.*, 96:092504, 2010.

[37] S. Steinert, F. Dolde, P. Neumann, A. Arid, B. Naydenov, G. Balasubramanian, F. Jelezko, and J. Wrachtrup. High sensitivity magnetic imaging using an array of spins in diamond. *Rev. Sci. Instrum.*, 81:043705, 2010.

[38] L. M. Pham, D. Le Sage, P. L. Stanwix, T. K. Yeung, D. Glenn, A. Trifonov, P. Cappellaro, P. R. Hemmer, M. D. Lukin, H. Park, A. Yacoby, and R. L. Walsworth. Magnetic field imaging with nitrogen-vacancy ensembles. *New J. Phys.*, 13:045021, 2011.

[39] E. Togan, Y. Chu, A. S. Trifonov, L. Jiang, J. Maze, L. Childress, M. V. G. Dutt, A. S. Sørensen, P. R. Hemmer, A. S. Zibrov, and M. D. Lukin. Quantum entanglement between an optical photon and a solid-state spin qubit. *Nature*, 466:730, 2010.

[40] F. Dolde, H. Fedder, M. W. Doherty, T. Nöbauer, F. Rempp, G. Balasubramanian, T. Wolf, F. Reinhard, L. C. L. Hollenberg, F. Jelezko, and J. Wrachtrup. Electric-field sensing using single diamond spins. *Nat. Phys.*, 7:459, 2011.

[41] B. Grotz, J. Beck, P. Neumann, B. Naydenov, R. Reuter, F. Reinhard, F. Jelezko, J. Wrachtrup, D. Schweinfurth, B. Sarkar, and P. Hemmer. Sensing external spins with nitrogen-vacancy diamond. *New J. Phys.*, 13:055004, 2011.

[42] H. J. Mamin, M. H. Sherwood, and D. Rugar. Detecting external electron spins using nitrogen-vacancy centers. *Phys. Rev. B*, 86:195422, 2012.

[43] S. Kolkowitz, Q. P. Unterreithmeier, S. D. Bennett, and M. D. Lukin. Sensing Distant Nuclear Spins with a Single Electron Spin. *Phys. Rev. Lett.*, 109:137601, 2012.

[44] T. H. Taminiau, J. J. T. Wagenaar, T. van der Sar, F. Jelezko, V. V. Dobrovitski, and R. Hanson. Detection and Control of Individual Nuclear Spin Using a Weakly Coupled Electron Spin. *Phys. Rev. Lett.*, 109:137602, 2012.

[45] N. Zhao, J. Honert, B. Schmid, M. Klas, J. Isoya, M. Markham, D. Twitchen, F. Jelezko, R.-B. Liu, H. Fedder, and J. Wrachtrup. Sensing single remote nuclear spins. *Nat. Nanotechnol.*, 7:657, 2012.

[46] H. J. Mamin, M. Kim, M. H. Sherwood, C. T. Rettner, K. Ohno, D. D. Awschalom, and D. Rugar. Nanoscale nuclear magnetic resonance with a nitrogen-vacancy spin sensor. *Science*, 339:557, 2013.

[47] T. Staudacher, F. Shi, S. Pezzagna, J. Meijer, J. Du, C. A. Meriles, F. Reinhard, and J. Wrachtrup. Nuclear Magnetic Resonance Spectroscopy on a (5-Nanometer)^3 Sample Volume. *Science*, 339:561, 2013.

[48] K. Ohashi, T. Rosskopf, H. Watanabe, M. Loretz, Y. Tao, R. Hauert, S. Tomizawa, T. Ishikawa, J. Ishi-Hayase, S. Shikata, C. L. Degen, and K. M. Itoh. Negatively Charged Nitrogen-Vacancy Centers in a 5 nm Thin ^{12}C Diamond Film. *Nano Lett.*, 13:4733, 2013.

[49] M. Loretz, S. Pezzagna, J. Meijer, and C. L. Degen. Nanoscale nuclear magnetic resonance with a 1.9-nm-deep nitrogen-vacancy sensor. *Appl. Phys. Lett.*, 104:033102, 2014.

[50] L. M. Pham, S. J. DeVience, F. Casola, I. Lovchinsky, A. O. Sushkov, E. Bersin, J. Lee, E. Urbach, P. Cappellaro, H. Park, A. Yacoby, M. Lukin, and R. L. Walsworth. NMR technique for determining the depth of shallow nitrogen-vacancy centers in diamond. *Phys. Rev. B*, 93:045425, 2016.

[51] C. Müller, X. Kong, J.-M. Cai, K. Melentijević, A. Stacey, M. Markham, D. Twitchen, J. Isoya, S. Pezzagna, J. Meijer, J. F. Du, M. B. Plenio, B. Naydenov, L. P. McGuinness, and F. Jelezko. Nuclear magnetic resonance spectroscopy with single spin sensitivity. *Nat. Commun.*, 5:4703, 2014.

[52] A. O. Sushkov, I. Lovchinsky, N. Chisholm, R. L. Walsworth, H. Park, and M. D. Lukin. Magnetic Resonance Detection of Individual Proton Spins using Quantum Reporters. *Phys. Rev. Lett.*, 113:197601, 2014.

[53] A. Laraoui, F. Dolde, C. Burk, F. Reinhard, J. Wrachtrup, and C. A. Meriles. High-resolution correlation spectroscopy of ^{13}C spins near a nitrogen vacancy centre in diamond. *Nat. Commun.*, 4:1651, 2013.

[54] A. Laraoui, J. S. Hodges, C. A. Ryan, and C. A. Meriles. Diamond nitrogen-vacancy center as a probe of random fluctuations in a nuclear spin ensemble. *Phys. Rev. B*, 84:104301, 2011.

[55] H. J. Mamin, M. H. Sherwood, M. Kim, C. T. Rettner, K. Ohno, D. D. Awschalom, and D. Rugar. Multipulse Double-Quantum Magnetometry with Near-Surface Nitrogen-Vacancy Centers. *Phys. Rev. Lett.*, 113:030803, 2014.

[56] M. S. Grinold, M. Warner, K. De Greve, Y. Dovzhenko, L. Thiel, R. L. Walsworth, S. Hong, P. Maletinsky, and A. Yacoby. Subnanometre resolution in three-dimensional magnetic resonance imaging of individual dark spins. *Nat. Nanotechnol.*, 9:279, 2014.

[57] J. Herrmann, M. A. Appleton, K. Sasaki, Y. Monnai, T. Teraji, K. M. Itoh, and E. Abe. Polarization- and frequency-tunable microwave circuit for selective excitation of nitrogen-vacancy spins in diamond. *Appl. Phys. Lett.*, 109:183111, 2016.

[58] K.-M. C. Fu, C. Santori, P. E. Barclay, and R. G. Beausoleil. Conversion of neutral nitrogen-vacancy centers to negatively charged nitrogen-vacancy centers through selective oxidation. *Appl. Phys. Lett.*, 96:121907, 2010.

[59] E. E. Kleinsasser, M. M. Stanfield, J. K. Q. Banks, Z. Zhu, W.-D. Li, V. M. Acosta, H. Watanabe, K. M. Itoh, and K.-M. C. Fu. High density nitrogen-vacancy sensing surface created via He^+ ion implantation of ^{12}C diamond. *Appl. Phys. Lett.*, 108:202401, 2016.

[60] L. Hall, P. Kehayias, D. A. Simpson, A. Jarmola, A. Stacey, D. Budker, and L. C. L. Hollenberg. Detection of nanoscale electron spin resonance spectra demonstrated using nitrogen-vacancy centre probes in diamond. *Nat. Commun.*, 7:10211, 2016.

[61] C. Abeywardana, V. Stepanov, F. H. Cho, and S. Takahashi. Electron spin resonance spectroscopy of small ensemble paramagnetic spins using a single nitrogen-vacancy center in diamond. *J. Appl. Phys.*, 120:123907, 2016.

[62] V. Stepanov and S. Takahashi. Determination of nitrogen spin concentration in diamond using double electron-electron resonance. *Phys. Rev. B*, 94:024421, 2016.

[63] K. Ito, H. Saito, K. Sasaki, H. Watanabe, T. Teraji, K. M. Itoh, and E. Abe. Nitrogen-vacancy centers created by N^+ ion implantation through screening Sio_2 layers on diamond. *Appl. Phys. Lett.*, 110:213105, 2017.

[64] G. de Lange, Z. H. Wang, D. Ristè, V. V. Dobrovitski, and R. Hanson. Universal Dynamical Decoupling of a Single Solid-state Spin from a Spin Bath. *Science*, 330:60, 2010.

[65] C. A. Ryan, J. S. Hodges, and D. G. Cory. Robust Decoupling Techniques to Extend Quantum Coherence in Diamond. *Phys. Rev. Lett.*, 105:200402, 2010.

[66] C. A. Meriles, L. Jiang, G. Goldstein, J. S. Hodges, J. Maze, M. D. Lukin, and P. Cappellaro. Imaging mesoscopic nuclear spin noise with a diamond magnetometer. *J. Chem. Phys.*, 133:124105, 2010.

[67] L. T. Hall, C. D. Hill, J. H. Cole, and L. C. L. Hollenberg. Ultrasensitive diamond magnetometry using optimal dynamic decoupling. *Phys. Rev. B*, 82:045208, 2010.

[68] G. de Lange, D. Ristè, V. V. Dobrovitski, and R. Hanson. Single-Spin Magnetometry with Multipulse Sensing Sequences. *Phys. Rev. Lett.*, 106:080802, 2011.

[69] B. Naydenov, F. Dolde, L. T. Hall, C. Shin, H. Fedder, L. C. L. Hollenberg, F. Jelezko, and J. Wrachtrup. Dynamical decoupling of a single-electron spin at room temperature. *Phys. Rev. B*, 83:081201, 2011.

[70] J. Casanova, Z.-Y. Wang, J. F. Haase, and M. B. Plenio. Robust dynamical decoupling sequences for individual-nuclear-spin addressing. *Phys. Rev. A*, 92:042304, 2015.

[71] J. M. Boss, K. Chang, J. Armijo, K. Cujia, T. Rosskopf, J. R. Maze, and C. L. Degen. One- and Two-Dimensional Nuclear Magnetic Resonance Spectroscopy with a Diamond Quantum Sensor. *Phys. Rev. Lett.*, 116:197601, 2016.

[72] Z. Shu, Z. Zhang, Q. Cao, P. Yang, M. B. Plenio, C Müller, J. Lang, N. Tomek, B. Naydenov, L. P. McGuinness, F. Jelezko, and J. Cai. Unambiguous nuclear spin

detection using an engineered quantum sensing sequence. *Phys. Rev. A*, 96:051402, 2017.

[73] L. Jiang, J. S. Hodges, J. R. Maze, P. Maurer, J. M. Taylor, D. G. Cory, P. R. Hemmer, R. L. Walsworth, A. Yacoby, A. S. Zibrov, and M. D. Lukin. Repetitive Readout of a Single Electronic Spin via Quantum Logic with Nuclear Spin Ancillae. *Science*, 326:267, 2009.

[74] P. Neumann, J. Beck, M. Steiner, F. Rempp, H. Fedder, P. R. Hemmer, J. Wrachtrup, and F. Jelezko. Single-Shot Readout of a Single Nuclear Spin. *Science*, 329:542, 2010.

[75] T. Häberle, T. Oeckinghaus, D. Schmid-Lorch, M. Pfender, F. F. de Oliveira, S. A. Momenzadeh, A. Finkler, and J. Wrachtrup. Nuclear quantum-assisted magnetometer. *Rev. Sci. Instrum.*, 88:013702, 2017.

[76] Y. Matsuzaki, T. Shimo-Oka, H. Tanaka, Y. Tokura, K. Semba, and N. Mizouchi. Hybrid quantum magnetic-field sensor with an electron spin and a nuclear spin in diamond. *Phys. Rev. A*, 94:052330, 2016.

[77] S. Zaiser, T. Rendler, I. Jakobi, T. Wolf, S.-Y. Lee, S. Wagner, V. Bergholm, T. Schulte-Herbrüggen, P. Neumann, and J. Wrachtrup. Enhancing quantum sensing sensitivity by a quantum memory. *Nat. Commun.*, 7:12279, 2016.

[78] T. Rosskopf, J. Zopes, J. M. Boss, and C. L. Degen. A quantum spectrum analyzer enhanced by a nuclear spin memory. *NPJ Quantum Information*, 3:33, 2017.

[79] I. Lovchinsky, A. O. Sushkov, E. Urbach, N. P. de Leon, S. Choi, K. De Greve, R. Evans, R. Gertner, E. Bersin, C. Müller, L. McGuinness, F. Jelezko, R. L. Walsworth, H. Park, and M. D. Lukin. Nuclear magnetic resonance detection and spectroscopy of single proteins using quantum logic. *Science*, 351:836, 2016.

[80] N. Aslam, M. Pfender, P. Neumann, R. Reuter, A. Zappe, F. F. de Oliveira, A. Denisenko, H.Sumiya, S. Onoda, J. Isoya, and J. Wrachtrup. Nanoscale nuclear magnetic resonance with chemical resolution. *Science*, 357:67, 2017.

[81] J. Zopes, K. Sasaki, K. S. Cujia, J. M. Boss, K. Chang, T. F. Segawa, K. M. Itoh, and C. L. Degen. High-Resolution Quantum Sensing with Shaped Control Pulses. *Phys. Rev. Lett.*, 119:260501, 2017.

[82] J. Zopes, K. S. Cujia, K. Sasaki, J. M. Boss, K. M. Itoh, and C. L. Degen. Three-dimensional localization spectroscopy of individual nuclear spins with sub-Angstrom resolution. *Nat. Commun.*, 9:4678, 2018.

[83] J. M. Boss, K. S. Cujia, J. Zopes, and C. L. Degen. Quantum sensing with arbitrary frequency resolution. *Science*, 356:837, 2017.

[84] S. Schmitt, T. Gefen, F. M. Stürner, T. Unden, G. Wolff, C. Müller, J. Scheuer, B. Naydenov, M. Markham, S. Pezzagna, J. Meijer, I. Schwarz, M. Plenio, A. Retzker, L. P. McGuinness, and F. Jelezko. Submillihertz magnetic spectroscopy performed with a nanoscale quantum sensor. *Science*, 356:832, 2017.

[85] D. R. Glenn, D. B. Bucher, J. Lee, M. D. Lukin, H. Park, and R. L. Walsworth. High-resolution magnetic resonance spectroscopy using a solid-state spin sensor. *Nature*, 555:351, 2018.

[86] I. Schwartz, J. Scheuer, B. Tratzmiller, S. Müller, Q. Chen, I. Dhand, Z.-Y. Wang, C. Müler, B. Naydenov, F. Jelezko, and M. B. Plenio. Robust optical polarization of nuclear spin baths using Hamiltonian engineering of nitrogen-vacancy center quantum dynamics. *Sci. Adv.*, 4:eaat8978, 2018.

[87] M. Pfender, P. Wang, H. Sumiya, S. Onoda, W. Yang, D. B. R. Dasari, P. Neumann, X.-Y. Pan, J. Isoya, R.-B. Liu, and J. Wrachtrup. High-resolution spectroscopy of single nuclear spins via sequential weak measurements. *Nat. Commun.*, 10:594, 2019.

[88] K. S. Cujia, J. M. Boss, K. Herb, J. Zopes, and C. L. Degen. Tracking the precession of single nuclear spins by weak measurements. *Nature*, 571:230, 2019.

[89] J. Zopes, K. Herb, K. S. Cujia, and C. L. Degen. Three-Dimensional Nuclear Spin Positioning Using Coherent Radio-Frequency Control. *Phys. Rev. Lett.*, 121:170801, 2018.

[90] M. H. Abobeih, J. Randall, C. E. Bradley, H. P. Bartling, M. A. Bakker, M. J. Degen, M. Markham, D. J. Twitchen, and T. H. Taminiau. Atomic-scale imaging of a 27-nuclear-spin cluster using a quantum sensor. *Nature*, 576:411, 2019.

[91] K. Sasaki, Y. Monnai, S. Saijo, R. Fujita, H. Watanabe, J. Ishi-Hayase, K. M. Itoh, and E. Abe. Broadband, large-area microwave antenna for optically detected magnetic resonance of nitrogen-vacancy centers in diamond. *Rev. Sci. Instrum.*, 87:053904, 2016.

[92] K. Sasaki, E. E. Kleinsasser, Z. Zhu, W.-D. Li, H. Watanabe, K.-M. C. Fu, K. M. Itoh, and E. Abe. Dynamic nuclear polarization enhanced magnetic field sensitivity and decoherence spectroscopy of an ensemble of near-surface nitrogen-vacancy centers in diamond. *Appl. Phys. Lett.*, 110:192407, 2017.

[93] K. Sasaki, K. M. Itoh, and E. Abe. Determination of the position of a single nuclear spin from free nuclear precessions detected by a solid-state quantum sensor. *Phys. Rev. B*, 98:121405, 2018.

[94] M. W. Doherty, N. B. Manson, P. Delaney, F. Jelezko, J. Wrachtrup, and L. C. L. Hollenberg. The nitrogen-vacancy colour centre in diamond. *Phys. Rep.*, 528:1, 2013.

[95] R. Schirhagl, K. Chang, M. Loretz, and C. L. Degen. Nitrogen-Vacancy Centers in Diamond: Nanoscale Sensors for Physics and Biology. *Annu. Rev. Phys. Chem.*, 65:83, 2014.

[96] L. Rondin, J.-P. Tetienne, T. Hingant, J.-F. Roch, P. Maletinsky, and V. Jacques. Magnetometry with nitrogen-vacancy defects in diamond. *Rep. Prog. Phys.*, 77:056503, 2014.

[97] A. Schweiger and G. Jeschke. *Principles of Pulse Electron Paramagnetic Resonance*. Oxford University Press, Oxford, 2001.

[98] N. Aslam, G. Waldherr, P. Neumann, F. Jelezko, and J. Wrachtrup. Photo-induced ionization dynamics of the nitrogen vacancy defect in diamond investigated by single-shot charge state detection. *New J. Phys.*, 15:013064, 2013.

[99] J. R. Maze, A. Gali, E. Togan, Y. Chu, A. Trifonov, E. Kaxiras, and M.D. Lukin. Properties of nitrogen-vacancy centers in diamond: the group theoretic approach. *New J. Phys.*, 13:025025, 2011.

[100] S. Felton, A. M. Edmonds, M. E. Newton, P. M. Martineau, D. Fisher, D. T. Twitchen, and J. M. Baker. Hyperfine interaction in the ground state of the negatively charged nitrogen vacancy center in diamond. *Phys. Rev. B*, 79:075203, 2009.

[101] A. Gali, M. Fyta, and E. Kaxiras. *Ab initio* supercell calculations on nitrogen-vacancy center in diamond: Electronic structure and hyperfine tensors. *Phys. Rev. Lett.*, 101:117601, 2008.

[102] M. Steiner, P. Neumann, J. Beck, F. Jelezko, and J. Wrachtrup. Universal enhancement of the optical readout fidelity of single electron spins at nitrogen-vacancy centers in diamond. *Phys. Rev. B*, 81:035205, 2010.

[103] L. Childress and R. Hanson. Diamond NV centers for quantum computing and quantum networks. *MRS Bull.*, 38:134, 2013.

[104] K. M. Itoh and H. Watanabe. Isotope engineering of silicon and diamond for quantum computing and sensing applications. *MRS Commun.*, 4:143, 2014.

[105] F. Jelezko and J. Wrachtrup. Single defect centres in diamond: A review. *Phys. Status Solidi A*, 203:3207, 2006.

[106] P. L. Stanwix, L. M. Pham, J. R. Maze, D. Le Sage, T. K. Yeung, P. Cappellaro, P. R. Hemmer, A. Yacoby, M. D. Lukin, and R. L. Walsworth. Coherence of nitrogen-vacancy electronic spin ensembles in diamond. *Phys. Rev. B*, 82:201201, 2010.

[107] N. Bar-Gill, L. M. Pham, A. Jarmola, D. Budker, and R. L. Walsworth. Solid-state electronic spin coherence time approaching one second. *Nat. Commun.*, 4:1743, 2013.

[108] D. M. Toyli, C. F. de las Casas, D. J. Christle, V. V. Dobrovitski, and D. D. Awschalom. Fluorescence thermometry enhanced by the quantum coherence of single spins in diamond. *Proc. Natl. Acad. Sci. U.S.A.*, 110:8417, 2013.

[109] P. Neumann, I. Jakobi, F. Dolde, C. Burk, R. Reuter, G. Waldherr, J. Honert, T. Wolf, A. Brunner, J. H. Shim, D. Suter, H. Sumiya, J. Isoya, and J. Wrachtrup. High-Precision Nanoscale Temperature Sensing Using Single Defects in Diamond. *Nano Lett.*, 13:2738, 2013.

[110] G. Kucsko, P. C. Maurer, N. Y. Yao, M. Kubo, H. J. Noh, P. K. Lo, H. Park, and M. D. Lukin. Nanometre-scale thermometry in a living cell. *Nature*, 500:54, 2013.

[111] D. R. Glenn, K. Lee, H. Park, R. Weissleder, A. Yacoby, M. D. Lukin, H. Lee, R. L. Walsworth, and C. B. Connolly. Single-cell magnetic imaging using a quantum diamond microscope. *Nat. Methods*, 12:736, 2015.

[112] R. R. Fu, B. P. Weiss, E. A. Lima, R. J. Harrison, X.-N. Bai, S. J. Desch, D. S. Ebel, C. Suavet, H. Wang, D. Glenn, D. Le Sage, T. Kasama, R. L. Walsworth, and A. T. Kuan. Solar nebula magnetic fields recorded in the Semarkona meteorite. *Science*, 346:1089, 2014.

[113] M. Chipaux, A. Tallaire, J. Achard, S. Pezzagna, J. Meijer, V. Jacques, J.-F. Roch, and T. Debuisschert. Magnetic imaging with an ensemble of nitrogen-vacancy centers in diamond. *Eur. Phys. J. D*, 69:166, 2015.

[114] K. Bayat, J. Choy, M. Farrokh Baroughi, S. Meesala, and M. Loncar. Efficient, Uniform, and Large Area Microwave Magnetic Coupling to NV Centers in Diamond Using Double Split-Ring Resonators. *Nano Lett.*, 14:1208, 2014.

[115] M. Mrózek, J. Mlynarczyk, D. S. Rudnicki, and W. Gawlik. Circularly polarized microwaves for magnetic resonance study in the GHz range: Application to nitrogen-vacancy in diamonds. *Appl. Phys. Lett.*, 107:013505, 2015.

[116] W. N. Hardy and L. A. Whitehead. Splitring resonator for use in magnetic resonance from 200-2000 MHz. *Rev. Sci. Instrum.*, 52:213, 1981.

[117] K. Aydin, I. Bulu, K. Guven, M. Kafesaki, C. M. Soukoulis, and E. Ozbay. Investigation of magnetic resonances for different split-ring resonator parameters and designs. *New J. Phys.*, 7:168, 2005.

[118] H. Watanabe, T. Kitamura, S. Nakashima, and S. Shikata. Cathodoluminescence characterization of a nitrogen-doped homoepitaxial diamond thin film. *J. Appl. Phys.*, 105:093529, 2009.

[119] T. Ishikawa, K.-M. C. Fu, C. Santori, V. M. Acosta, R. G. Beausoleil, H. Watanabe, S. Shikata, and K. M. Itoh. Optical and Spin Coherence Properties of Nitrogen-Vacancy Centers Placed in a 100 nm Thick Isotopically Purified Diamond layer. *Nano Lett.*, 12:2083, 2012.

[120] H.Hopster and H. P. Oepen. *Magnetic Microscopy of Nanostructures.* Springer, Berlin, 2005.

[121] D. Le Sage, K. Arai, D. R. Glenn, S. J. DeVince, L. M. Pham, L. Rahn-Lee, M. D. Lukin, A. Yacoby, A. Komeili, and R. L. Walsworth. Optical magnetic imaging of living cells. *Nature*, 496:486, 2013.

[122] D. A. Simpson, J.-P. Tetienne, J. M. McCoey, K. Ganesan, L. T. Hall, S. Petrou, R. E. Scholten, and L. C. L. Hollenberg. Magneto-optical imaging of thin magnetic films using spins in diamond. *Sci. Rep.*, 6:22797, 2016.

[123] J. Wrachtrup, F. Jelezko, B. Grotz, and L. McGuinness. Nitrogen-vacancy centers close to surfaces. *MRS Bull.*, 38:149, 2013.

[124] G. de Lange, T. van der Sar, M. Blok, Z.-H. Wang, V. Dobrovitski, and R. Hanson. Controlling the quantum dynamics of a mesoscopic spin bath in diamond. *Sci. Rep.*, 2:382, 2012.

[125] L. P. McGuinness, L. T. Hall, A. Stacey, D. A. Simpson, C. D. Hill, J. H. Cole, K. Ganesan, B. C. Gibson, S. Prawer, P. Mulvaney, F. Jelezko, J. Wrachtrup, R. E. Scholten, and L. C. L. Hollenberg. Ambient nanoscale sensing with single spins using quantum decoherence. *New J. Phys.*, 15:073042, 2013.

[126] L. Luan, M. S. Grinolds, S. Hong, P. Maletinsky, R. L. Walsworth, and A. Yacoby. Decoherence imaging of spin ensembles using a scanning single-electron spin in diamond. *Sci. Rep.*, 5:8119, 2015.

[127] D. Schmid-Lorch, T. Häberle, F. Reinhard, A. Zappe, M. Slota, L. Bogani, A. Finkler, and J. Wrachtrup. Relaxometry and Dephasing Imaging of Superparamagnetic Magnetite Nanoparticles Using a Single Qubit. *Nano Lett.*, 15:4942, 2015.

[128] A. Dréau, M. Lesik, L. Rondin, P. Spinicelli, O. Arcizet, J.-F. Roch, and V. Jacques. Avoiding power broadening in optically detected magnetic resonance of single nv defects for enhanced dc magnetic field sensitivity. *Phys. Rev. B*, 84:195204, 2011.

[129] V. Jacques, P. Neumann, J. Beck, M. Markham, D. Twitchen, J. Meijer, F. Kaiser, G. Balasubramanian, F. Jelezko, and J. Wrachtrup. Dynamic Polarization of Single Nuclear Spins by Optical Pumping of Nitrogen-Vacancy Color Centers in Diamond at Room Temperature. *Phys. Rev. Lett.*, 102:057403, 2009.

[130] R. Fischer, A. Jarmola, P. Kehayias, and D. Budker. Optical polarization of nuclear ensembles in diamond. *Phys. Rev. B*, 87:125207, 2013.

[131] T. Wolf, P. Neumann, K. Nakamura, H. Sumiya, T. Ohshima, J. Isoya, and J. Wrachtrup. Subpicotesla Diamond Magnetometry. *Phys. Rev. X*, 5:041001, 2015.

[132] W. V. Smith, P. P. Sorokin, I. L. Gelles, and G. J. Lasher. Electron-Spin Resonance of Nitrogen Donors in Diamond. *Phys. Rev.*, 115:1546, 1959.

[133] J. R. Klauder and P. W. Anderson. Spectral Diffusion Decay in Spin Resonance Experiments. *Phys. Rev.*, 125:912, 1962.

[134] L. M. Pham, N. Bar-Gill, C. Belthangady, D. Le Sage, P. Cappellaro, M. D. Lukin, A. Yacoby, and R. L. Walsworth. Enhanced solid-state multispin metrology using dynamical decoupling. *Phys. Rev. B*, 86:045214, 2012.

[135] A. Abragam. *Principles of Nuclear Magnetism*. Oxford University Press, Oxford, 1961.

[136] J. A. van Wyk, E. C. Reynhardt, G. L. High, and I. Kiflawi. The dependences of esr line widths and spin - spin relaxation times of single nitrogen defects on the concentration of nitrogen defects in diamond. *J. Phys. D: Appl. Phys.*, 30:1790, 1997.

[137] A. Jarmola, V. M. Acosta, K. Jensen, S. Chemerisov, and D. Budker. Temperature- and Magnetic-Field-Dependent Longitudinal Spin Relaxation in Nitrogen-Vacancy Ensembles in Diamond. *Phys. Rev. Lett.*, 108:197601, 2012.

[138] M. Mrózek, D. Rudnicki, P. Kehayias, A. Jarmola, D. Budker, and W. Gawlik. Longitudinal spin relaxation in nitrogen-vacancy ensembles in diamond. *EPJ Quantum Technol.*, 2:22, 2015.

[139] J. D. A. Wood, D. A. Broadway, L. T. Hall, A. Stacey, D. A. Simpson, J.-P. Tetienne, and L. C. L. Hollenberg. Wide-band nanoscale magnetic resonance spectroscopy using quantum relaxation of a single spin in diamond. *Phys. Rev. B*, 94:155402, 2016.

[140] J. A. Sidles, J. L. Garbini, K. J. Bruland, D. Ruger, O. Züger, S. Hoen, and C. S. Yannoni. Magnetic resonance force microscopy. *Rev. Mod. Phys.*, 67:249, 1995.

[141] D. Rugar, R. Budakian, H. J. Mamin, and B. W. Chui. Single spin detection by magnetic resonance force microscopy. *Nature*, 430:329, 2004.

[142] C. L. Degen, M. Poggino, H. J. Mamin, C. T. Rettner, and D. Ruger. Nanoscale magnetic resonance imaging. *Proc. Natl. Acad. Sci. U.S.A.*, 106:1313, 2009.

[143] H. Y. Carr and E. M. Purcell. Effect of Diffusion on Free Precession in Nuclear Magnetic Resonance Experiments. *Phys. Rev.*, 94:630, 1954.

[144] S. Meiboom and D. Gill. Modified Spin-Echo Method for Measuring Nuclear Relaxation Times. *Rev. Sci. Instrum.*, 29:688, 1958.

[145] T. Gullion, D. B. Baker, and M. S. Conradi. New, Compensated Carr-Purcell Sequences. *J. Magn. Reson.*, 89:479, 1990.

[146] A. Ajoy, Y.-X. Liu, K. Saha, L. Marseglia, J.-C. Jaskula, U. Bissbort, and P. Cappellaro. Quantum interpolation for high-resolution sensing. *Proc. Natl. Acad. Sci. U.S.A.*, 114:2149, 2017.

[147] Z.-Y. Wang, J. E. Lang, S. Schmitt, J. Lang, J. Casanova, L. Mc Guinness, T. S. Monteiro, F. Jelezko, and M. B. Plenio. Randomization of Pulse Phases for Unambiguous and Robust Quantum Sensing. *Phys. Rev. Lett.*, 122:200403, 2019.

[148] E. Kupče and R. Freeman. Adiabatic Pulses for Wideband Inversion and Broadband Decoupling. *J. Magn. Reson.*, 115:273, 1995.

[149] P. E. Spindler, P. Schöps, A. M. Bowen, B. Endeward, and T. F. Prisner. Shaped Pulses in EPR. *eMagRes*, 5:1477, 2016.

[150] E. Abe and K. Sasaki. Tutorial: Magnetic resonance with nitrogen-vacancy centers in diamond—microwave engineering, materials science, and magnetometry. *J. Appl. Phys.*, 123:161101, 2018.

[151] T. Häberle, D. Schmid-Lorch, F. Reinhard, and J. Wrachtrup. Nanoscale nuclear magnetic imaging with chemical contrast. *Nat. Nanotechnol.*, 10:125, 2015.

[152] S. J. DeVience, L. M. Pham, I. Lovchinsky, A. O. Sushkov, N. Bar-Gill, C. Belthangady, F. Casola, M. Corbett, H. Zhang, M. Lukin, H. Park, A. Yacoby, and R. L. Walsworth. Nanoscale NMR spectroscopy and imaging of multiple nuclear species. *Nat. Nanotechnol.*, 10:129, 2015.

[153] T. Staudacher, N. Raatz, S. Pezzagna, J. Meijer, F. Reinhard, C. A. Meriles, and J. Wrachtrup. Probing molecular dynamics at the nanoscale via an individual paramagnetic centre. *Nat. Commun.*, 6:8527, 2015.

[154] X. Kong, A. Stark, J. Du, L. P. McGuinness, and F. Jelezko. Towards Chemical Structure Resolution with Nanoscale Nuclear Magnetic Resonance Spectroscopy. *Phys. Rev. Appl.*, 4:024004, 2015.

[155] V. S. Perunicic, C. D. Hill, L. T. Hall, and L. C. L. Hollenberg. A quantum spin-probe molecular microscope. *Nat. Commun.*, 7:12667, 2016.

[156] P. Kehayias, A. Jarmola, N. Mosavian, I. Fescenko, F. M. Benito, A. Laraoui, J. Smits, L. Bougas, D. Budker, A. Neumann, S. R. J. Brueck, and V. M. Acosta. Solution nuclear magnetic resonance spectroscopy on a nanostructured diamond chip. *Nat. Commun.*, 8:188, 2017.

[157] N. Zhao, J.-L. Hu, S.-W. Ho, J. T. K. Wan, and R.-B. Liu. Atomic-scale magnetometry of distant nuclear spin clusters via nitrogen-vacancy spin in diamond. *Nat. Nanotechnol.*, 6:242, 2011.

[158] A. Laraoui, D. Pagliero, and C. A. Meriles. Imaging nuclear spins weakly coupled to a probe paramagnetic center. *Phys. Rev. B*, 91:205410, 2015.

[159] Z.-Y. Wang, J. F. Haase, J. Casanova, and M. B. Plenio. Positioning nuclear spins in interacting clusters for quantum technologies and bioimaging. *Phys. Rev. B*, 93:174104, 2016.

[160] Z.-Y. Wang, J. Casanova, and M. B. Plenio. Delayed entanglement echo for individual control of a large number of nuclear spins. *Nat. Commun.*, 8:14660, 2017.

[161] T. H. Taminiau, J. Cramer, T. van der Sar, V. V. Dobrovitski, and R. Hanson. Universal control and error correction in multi-qubit spin registers in diamond. *Nat. Nanotechnol.*, 9:171, 2014.

[162] A. P. Nizovtsev, S. Y. Kilin, A. L. Pushkarchuk, V. A. Pushkarchuk, S. A. Kuten, O. A. Zhikol, S. Schmitt, T. Unden, and F. Jelezko. Non-flipping ^{13}C spins near an NV center in diamond: Hyperfine and spatial characteristics by density functional theory simulation of the $C_{510}[NV]H_{252}$ cluster. *New J. Phys.*, 20:023022, 2018.

[163] J. Scheuer, I. Schwartz, S. Müller, Q. Chen, I. Dhand, M. B. Plenio, B. Naydenov, and F. Jelezko. Robust techniques for polarization and detection of nuclear spin ensembles. *Phys. Rev. B*, 96:174436, 2017.

[164] U. Haeberlen. *High Resolution NMR in Solids Selective Averaging*. Academic, New York, 1976.

[165] J. Wang, F. Feng, J. Zhang, J. Chen, Z. Zheng, L. Guo, W. Zhang, X. Song, G. Guo, L. Fan, C. Zou, L. Lou, W. Zhu, and G. Wang. High-sensitivity temperature sensing using an implanted single nitrogen-vacancy center array in diamond. *Phys. Rev. B*, 91:155404, 2015.

[166] D. A. Simpson, E. Morrisroe, J. M. McCoey, A. H. Lombard, D. C. Mendis, F. Treussart, L. T. Hall, S. Petrou, and L. C. L. Hollenberg. Non-Neurotoxic Nanodiamond Probes for Intraneuronal Temperature Mapping. *ACS Nano*, 11:12077, 2017.

[167] H. C. Davis, P. Ramesh, A. Bhatnagar, A. Lee-Gosselin, J. F. Barry, D. R. Glenn, R. L. Walsworth, and M. G. Shapiro. Mapping the microscale origins of magnetic resonance image contrast with subcellular diamond magnetometry. *Nat. Commun.*, 9:131, 2018.

[168] J. F. Barry, M. J. Turner, J. M. Schloss, D. R. Glenn, Y. Song, M. D. Lukin, H. Park, and R. L. Walsworth. Optical magnetic detection of single-neuron action potentials using quantum defects in diamond. *Proc. Natl. Acad. Sci. U.S.A.*, 113:14133, 2016.

[169] L.-S. Bouchard, V. M. Acosta, E. Bauch, and D. Budker. Detection of the Meissner effect with a diamond magnetometer. *New J. Phys.*, 13:025017, 2011.

[170] A. Waxman, Y. Schlussel, D. Groswasser, V. M. Acosta, L.-S. Bouchard, D. Budker, and R. Folman. Diamond magnetometry of superconducting thin films. *Phys. Rev. B*, 89:054509, 2014.

[171] N. Alfasi, S. Masis, O. Shtempluck, V. Kochetok, and E. Buks. Diamond magnetometry of Meissner currents in a superconducting film. *AIP Adv.*, 6:075311, 2016.

[172] M. Pelliccione, A. Jenkins, P. Ovartchaiyapong, C. Reetz, E. Emmanouilidou, N. Ni, and A. C. B. Jayich. Scanned probe imaging of nanoscale magnetism at cryogenic temperatures with a single-spin quantum sensor. *Nat. Nanotechnol.*, 11:700, 2016.

[173] L. Thiel, D. Rohner, M. Ganzhorn, P. Appel, E. Neu, B. Müller, R. Kleiner, D. Koelle, and P. Maletinsky. Quantitative nanoscale vortex imaging using a cryogenic quantum magnetometer. *Nat. Nanotechnol.*, 11:677, 2016.

[174] D. Rohner, L. Thiel, B. Müller, M. Kasperczyk, R. Kleiner, D. Koelle, and P. Maletinsky. Real-Space Probing of the Local Magnetic Response of Thin-Film Superconductors Using Single Spin Magnetometry. *Sensors*, 18:3790, 2018.

[175] Y. Schlussel, T. Lenz, D. Rohner, Y. Bar-Haim, L. Bougas, D. Groswasser, M. Kieschnick, E. Rozenberg, L. Thiel, A. Waxman, J. Meijer, P. Meletinsky, D. Budker, and R. Folman. Wide-Field Imaging of Superconductor Vortices with Electron Spins in Diamond. *Phys. Rev. Appl.*, 10:034032, 2018.

[176] N. M. Nusran, K. R. Joshi, K. Cho, M. A. Tanatar, W. R. Meier, S. L. Bud'ko, P. C. Canfield, Y. Liu, T. A. Lograsso, and R. Prozorov. Spatially-resolved study of the Meissner effect in superconductors using NV-centers-in-diamond optical magnetometry. *New J. Phys.*, 20:043010, 2018.

[177] K. R. Joshi, N. M. Nusran, M. A. Tanatar, K. Cho, W. R. Meier, S. L. Bud'ko, P. C. Canfield, and R. Prozorof. Measuring the Lower Critical Field of Superconductors Using Nitrogen-Vacancy Centers in Diamond Optical Magnetometry. *Phys. Rev. Appl.*, 11:014035, 2019.

[178] Y. Xu, Y. Yu, Y. Y. Hui, Y. Su, J. Cheng, H.-C. Chang, Y. Zhang, Y. R. Shen, and C. Tian. Mapping Dynamical Magnetic Responses of Ultra-thin Micron-size Superconducting Films using Nitrogen-vacancy Centers in Diamond. *Nano Lett.*, 19:5697, 2019.

[179] A. Nowodzinski, M. Chipaux, L. Toraille, V. Jacques, J.-F. Roch, and T. Debuisschert. Nitrogen-Vacancy centers in diamond for current imaging at the redistributive layer level of Integrated circuits. *Microelectron. Reliab.*, 55:1549, 2015.

[180] J.-P. Tetienne, N. Dontschuk, D. A. Broadway, A. Stacey, D. A. Simpson, and L. C. L. Hollenberg. Quantum imaging of current flow in graphene. *Sci. Adv.*, 3:e1602429, 2017.

[181] K. Chang, A. Eichler, J. Rhensius, L. Lorenzelli, and C. L. Degen. Nanoscale Imaging of Current Density with a Single-Spin Magnetometer. *Nano Lett.*, 17:2367, 2017.

[182] A. Ariyaratne, D. Bluvstein, B. A. Myers, and A. C. B. Jayich. Nanoscale electrical conductivity imaging using a nitrogen-vacancy center in diamond. *Nat. Commun.*, 9:2406, 2018.

[183] M. J. H. Ku, T. X. Zhou, Q. Li, Y. J. Shin, J. K. Shi, C. Burch, H. Zhang, F. Casola, T. Taniguchi, K. Watanabe, P. Kim, A. Yacoby, and R. L. Walsworth. Imaging Viscous Flow of the Dirac Fluid in Graphene Using a Quantum Spin Magnetometer. *arXiv:1905.10791*, 2019.

[184] G. Chatzidrosos, A. Wichenbrock, L. Bougas, H. Zheng, O. Tretiak, Y. Yang, and D. Budker. Eddy-Current Imaging with Nitrogen-Vacancy Centers in Diamond. *Phys. Rev. Appl.*, 11:014060, 2019.

[185] L. Rondin, J.-P. Tetienne, S. Rohart, A. Thiaville, T. Hingant, P. Spinicelli, J.-F. Roch, and V. Jacques. Stray-field imaging of magnetic vortices with a single diamond spin. *Nat. Commun.*, 4:2279, 2013.

[186] J.-P. Tetienne, T. Hingant, J.-V. Kim, L. Herrera Diez, J.-P. Adam, K. Garcia, J.-F. Roch, S. Rohart, A. Thiaville, D. Ravelosona, and V. Jacques. Nanoscale imaging and control of domain-wall hopping with a nitrogen-vacancy center microscope. *Science*, 344:1366, 2014.

[187] I. Gross, L. I. Martínez, J. P. Tetienne, T. Hingant, J.-F. Roch, K. Garcia, R. Soucaille, J. P. Adam, J.-V. Kim, S. Rohart, A. Thiaville, J. Torrejon, M. Hayashi, and

V. Jacques. Direct measurement of interfacial Dzyaloshinskii-Moriya interaction in X|CoFeB|MgO heterostructures with a scanning NV magnetometer (X=Ta, TaN, and W). *Phys. Rev. B*, 94:064413, 2016.

[188] I. Gross, W. Akhtar, V. Garcia, L. J. Martinez, S. Chouaieb, K. Garcia, C. Carrétéro, A. Barthélémy, P. Appel, P. Maletinsky, J.-V. Kim, J. Y. Chauleau, N. Jaouen, M. Viret, M. Bibes, S. Fusil, and V. Jacques. Real-space imaging of non-collinear antiferromagnetic order with a single-spin magnetometer. *Nature*, 252:549, 2017.

[189] Y. Dovzhenko, F. Casola, S. Schlotter, T. X. Zhou, F. Büttner, R. L. Walsworth, G. S. D. Beach, and A. Yacoby. Magnetostatic twists in room-temperature skyrmions explored by nitrogen-vacancy center spin texture reconstruction. *Nat. Commun.*, 10:1038, 2018.

[190] I. Gross, W. Akhtar, A. Hrabec, J. Sampaio, L. J. Martinez, S. Chouaieb, B. J. Shields, P. Maletinsky, A. Thiaville, S. Rohart, and V. Jacques. Skyrmion morphology in ultrathin magnetic films. *Phys. Rev. Mater.*, 2:024406, 2018.

[191] G. Yu, A. Jenkins, X. Ma, S. A. Razavi, C. He, G. Yin, Q. Shao, Q. lin He, H. Wu, W. Li, W. Jiang, X. Han, X. Li, A. C. B. Jayich, P. K. Amiri, and K. L. Wang. Room-Temperature Skyrmions in an Antiferromagnet-Based Heterostructure. *Nano Lett.*, 18:980, 2018.

[192] A. Jenkins, M. Pelliccione, G. Yu, X. Ma, X. Li, K. L. Wang, and A. C. B. Jayich. Single-spin sensing of domain-wall structure and dynamics in a thin-film skyrmion host. *Phys. Rev. Mater.*, 3:083801, 2019.

[193] S. Kolkowitz, A. Safira, A. A. High, R. C. Devlin, S. Choi, Q. P. Unterreithmeier, D. Patterson, A. S. Zibrov, V. E. Manucharyan, H. Park, and M. D. Lukin. Probing Johnson noise and ballistic transport in normal metals with a single-spin qubit. *Science*, 347:1129, 2015.

[194] S. E. Lillie, D. A. Broadway, N. Dontschuk, A. Zavabeti, D. A. Simpson, T. Teraji, T. Daeneke, L. C. L. Hollenberg, and J.-P. Tetienne. Magnetic noise from ultrathin abrasively deposited materials on diamond. *Phys. Rev. Mater.*, 2:116002, 2018.

[195] T. van der Sar, F. Casola, R. Walsworth, and A. Yacoby. Nanometre-scale probing of spin waves using single electron spins. *Nat. Commun.*, 6:7886, 2015.

[196] C. Du, T. van der Sar, T. X. Zhou, P. Upadhyaya, F. Casola, H. Zhang, M. C. Onbasli, C. A. Ross, R. L. Walsworth, Y. Tserkovnyak, and A. Yacoby. Control and local measurement of the spin chemical potential in a magnetic insulator. *Science*, 357:195, 2017.

[197] A. Solyom, Z. Flansberry, M. A. Tschudin, N. Leitao, M. Pioro-Ladrière, J. C. Sankey, and L. I. Childress. Probing a Spin Transfer Controlled Magnetic Nanowire with a Single Nitrogen-Vacancy Spin in Bulk Diamond. *Nano Lett.*, 18:6494, 2018.

[198] H. Zhang, M. J. H. Ku, F. Casola, C. H. Du, T. van der Sar, M. C. Onbasli, C. A. Ross, Y. Terkovnyak, A. Yacoby, and R. L. Walsworth. Spin-torque oscillation in a magnetic insulator probed by a single-spin sensor. *arXiv:1810.07306*, 2018.

[199] C. S. Wolfe, S. A. Manuilov, C. M. Purser, R. Teeling-Smith, C. Dubs, P. C. Hammel, and V. P. Bhallamudi. Spatially resolved detection of complex ferromagnetic dynamics using optically detected nitrogen-vacancy spins. *Appl. Phys. Lett.*, 108:232409, 2016.

[200] P. Andrich, C. F. de las Casas, X. Liu, H. L. Bretscher, J. R. Berman, F. J. Heremans, P. F. Nealey, and D. D. Awschalom. Long-range spin wave mediated control of defect qubits in nanodiamonds. *npj Quantum Inf.*, 3:28, 2017.

[201] D. Kikuchi, D. Prananto, K. Hayashi, A. Laraoui, N. Mizuochi, M. Hatano, E. Saitoh, Y. Kim, C. A. Meriles, and T. An. Long-distance excitation of nitrogen-vacancy centers in diamond via surface spin waves. *Appl. Phys. Express*, 10:103004, 2017.

[202] I. Lovchinsky, J. D. Sanchez-Yamagishi, E. K. Urbach, S. Choi, S. Fang, T. I. Anderson, K. Watanabe, T. Taniguchi, A. Bylinskii, E. Kaxiras, P. Kim, H. Park, and M. D. Lukin. Magnetic resonance spectroscopy of an atomically thin material using a single-spin qubit. *Science*, 355:503, 2017.

[203] A. Ermakova, G. Pramanik, J.-M. Cai, G. Algara-Siller, U. Kaiser, T. Weil, Y.-K. Tzeng, H. C. Chang, L. P. McGuinness, M. B. Plenio, B. Naydenov, and F. Jelezko. Detection of a Few Metallo-Protein Molecules Using Color Centers in Nanodiamonds. *Nano Lett.*, 13:3305, 2013.

[204] E. Schäfer-Nolte, L. Schlipf, M. Ternes, F. Reinhard, K. Kern, and J. Wrachtrup. Tracking Temperature-Dependent Relaxation Times of Ferritin Nanomagnets with a Wideband Quantum Spectrometer. *Phys. Rev. Lett.*, 113:217204, 2014.

[205] F. Shi, Q. Zhang, P. Wang, H. Sun, J. Wang, X. Rong, M. Chen, C. Ju, F. Reinhard, H. Chen, J. Wrachtrup, J. Wang, and J. Du. Single-protein spin resonance spectroscopy under ambient conditions. *Science*, 347:1135, 2015.

[206] S. Hong, M. S. Grinolds, L. M. Pham, D. Le Sage, L. Luan, R. L. Walsworth, and A. Yacoby. Nanoscale magnetometry with nv centers in diamond. *MRS Bull.*, 38:155, 2013.

[207] J. Wrachtrup and A. Finkler. Single spin magnetic resonance. *J. Magn. Reson.*, 269:225, 2016.

[208] X. Chen and W. Zhang. Diamond nanostructures for drug delivery, bioimaging, and biosensing. *Chem. Soc. Rev.*, 46:734, 2017.

[209] D. Suter and F. Jelezko. Single-spin magnetic resonance in the nitrogen-vacancy center of diamond. *Prog. Nucl. Mag. Resonance Spectroscopy*, 98:50, 2017.

[210] C. L. Degen, F. Reinhard, and P. Cappellaro. Quantum sensing. *Rev. Mod. Phys.*, 89:035002, 2017.

[211] F. Casola, T. van der Sar, and A. Yacoby. Probing condensed matter physics with magnetometry based on nitrogen-vacancy centres in diamond. *Nat. Rev. Mater.*, 3:17088, 2018.

[212] V. M. Acosta, L. S. Bouchard, D. Budker, R. Folman, T. Lenz, P. Maletinsky, D. Rohner, Y. Schlussel, and L. Thiel. Color centers in diamond as novel probes of superconductivity. *J. Supercond. Novel Magn.*, 32:85, 2019.

[213] S. Rajendran, N. Zobrist, A. O. Sushkov, R. Walsworth, and M. Lukin. A method for directional detection of dark matter using spectroscopy of crystal defects. *Phys. Rev. D*, 96:035009, 2017.

[214] V. Meyer, S. S, Eaton, and G. R. Eaton. Temperature Dependence of Electron Spin Relaxation of 2,2-diphenyl-1-picrylhydrazyl in Polystyrene. *Appl. Magn. Reson.*, 44:509, 2013.

[215] A. Henstra, P. Dirksen, J. Schmidt, and W. T. Wenckebach. Nuclear Spin Orientation via Electron Spin Locking (NOVEL). *J. Magn. Reson.*, 77:389, 1988.

[216] J. Scheuer, I. Schwartz, Q. Chen, D. S.-Sünninghausen, P. Carl, Höfer, A. Retzker, H. Sumiya, J. Isoya, B. Luy, M. B. Plenio, B. Naydenov, and F. Jelezko. Optically induced dynamic nuclear spin polarization in diamond. *New J. Phys.*, 18:013040, 2016.